

Utah State University

DigitalCommons@USU

All Graduate Theses and Dissertations, Fall
2023 to Present

Graduate Studies

8-2024

Advancing Thermal Property Measurements and Water Management for Controlled Environment Agriculture on Earth and Beyond

Chihiro Dixon
Utah State University

Follow this and additional works at: <https://digitalcommons.usu.edu/etd2023>



Part of the [Plant Sciences Commons](#), and the [Soil Science Commons](#)

Recommended Citation

Dixon, Chihiro, "Advancing Thermal Property Measurements and Water Management for Controlled Environment Agriculture on Earth and Beyond" (2024). *All Graduate Theses and Dissertations, Fall 2023 to Present*. 315.

<https://digitalcommons.usu.edu/etd2023/315>

This Dissertation is brought to you for free and open access by the Graduate Studies at DigitalCommons@USU. It has been accepted for inclusion in All Graduate Theses and Dissertations, Fall 2023 to Present by an authorized administrator of DigitalCommons@USU. For more information, please contact digitalcommons@usu.edu.



ADVANCING THERMAL PROPERTY MEASUREMENTS AND WATER
MANAGEMENT FOR CONTROLLED ENVIRONMENT
AGRICULTURE ON EARTH AND BEYOND

by

Chihiro Dixon

A dissertation submitted in partial fulfillment
of the requirements for the degree

of

DOCTOR OF PHILOSOPHY

in

Soil Science

Approved:

Scott B. Jones, Ph.D.
Major Professor

Bruce Bugbee, Ph.D.
Committee Member

Lawrence Hipps, Ph.D.
Committee Member

Wenyi Sheng, Ph.D.
Committee Member

Pin Shuai, Ph.D.
Committee Member

D. Richard Cutler, Ph.D.
Vice Provost of Graduate Studies

UTAH STATE UNIVERSITY
Logan, Utah

2024

Copyright © Chihiro Dixon 2024

All Rights Reserved

ABSTRACT

Advancing Thermal Property Measurements and Water Management for
Controlled Environment Agriculture on Earth and Beyond

by

Chihiro Dixon, Doctor of Philosophy

Utah State University, 2024

Major Professor: Dr. Scott B. Jones
Department: Plants, Soils and Climate

Plant growth systems operating under reduced gravity conditions (i.e., μg) face challenges related to altered water distribution in the root zone. This inconsistency can lead to hypoxia (excessive water) and drought stress (insufficient water), affecting plant yield, which is a crucial component of sustaining astronauts' diet and mental well-being during space missions. This research aimed to enhance the accuracy of thermal property sensors, specifically Heat Pulse Probes (HPP), utilized in previous space missions to monitor water content in the root zone. Additionally, the study aimed to deepen our understanding of managing optimal water status in containerized plant growth media, particularly synthetic and natural fibers, based on understanding the hysteretic water retention characteristic. Calibrating HPPs with air-free ice yielded sharper peak temperature rise curves compared to traditional media (i.e., agar-stabilized water), facilitating the optimization of temperature

analysis models. Various granular media, prepared using the air-pluviation method, yielded reproducible bulk density, providing additional thermal property calibration standards across a range of water content from oven-dry- to saturated-conditions. An automated water retention measurement system was designed and fabricated based on a traditional method (i.e., hanging water column). This system coupled with model fitting using existing water retention models, enabled efficient characterization of hysteretic water retention of coarse-textured media within a typical controlled range of matric potential for plant growth ($-50 < h < 0$ cm). Lightweight fibrous media exhibited water retention characteristics compatible with traditional horticultural media (i.e., peat moss), suggesting their suitability as plant growth media and facilitating fluid distribution when constructing layered root zones using fabric and peat moss. An optimized plant-optimal passive irrigation system utilizing a Mariotte bottle connected to a check valve and porous membrane was introduced and validated for controlling target matric potential based on the media's water retention characteristics. This system offers potential improvements in passive irrigation under μ g conditions, compensating for the lack of gravity and maintaining target matric potential without powered pumps or valves. Overall, this research advances the design and implementation of plant growth systems for use in microgravity conditions and on Earth.

(236 pages)

PUBLIC ABSTRACT

Advancing Thermal Property Measurements and Water Management for
Controlled Environment Agriculture on Earth and Beyond

Chihiro Dixon

Space exploration stands as one of humanity's most profound endeavors, and plant growth in space is essential for sustaining astronauts during long-duration missions. However, operating plant growth systems under reduced gravity conditions presents challenges, particularly in ensuring uniform water distribution in the root zone. Non-uniform water distribution such as excess water and/or insufficient water in the root zone can significantly impact plant yield, necessitating the need to accurately estimate water status in the root zone and understand the dynamics of water flow in plant growth media under reduced gravity conditions. The objectives of this research were to enhance the accuracy of thermal property sensors using innovative techniques such as Heat Pulse Probes (HPPs), which were used in previous space missions to monitor water content in the root zone. We also wanted to advance our understanding of managing optimal water status in containerized plant growth media, particularly how water is retained and released from synthetic and natural fibers. Calibrating HPPs using air-free ice provided sharper temperature rise curves compared to traditional calibration media, leading to improved thermal property estimation. Various granular media with reproducible bulk density were utilized to establish thermal property calibration standards across different water content

levels. The development of an automated water retention measurement system enabled efficient characterization of water retention in coarse-textured media. This research clarified the suitability of lightweight fabrics as candidate plant growth media by comparing them with the water retention characteristics of traditional plant growth media (i.e., peat moss). Furthermore, an optimized irrigation system requiring no automated controls was presented. That system included a Mariotte bottle connected to a check valve and porous membrane used to maintain the target water status during plant growth, offering potential simplification of plant growth systems used in past space missions. Overall, this research contributes to advancing plant growth systems for microgravity conditions, with implications for both space exploration and agriculture on Earth. By ensuring efficient water distribution in plant growth media, we pave the way for sustainable food production in space and on Earth.

DEDICATION

I would like to dedicate this work to my grandpa, Hirotada.

ACKNOWLEDGMENT

I am deeply indebted to my academic advisor, Scott B. Jones, for his unwavering dedication to teaching, trust, and encouragement. While the pursuit of graduate studies spanning seven years is uncommon, Scott's faith in me and his words of encouragement nurtured my appreciation for the challenges and hardships I experienced during graduate school. I extend my heartfelt gratitude to Scott not only as an academic advisor but also as a mentor and a friend. As an international student who embarked on this journey without knowing anyone, I am profoundly grateful that Scott took on the role of my major advisor.

I would also like to express my gratitude to my committee members, Drs. Bruce Bugbee, Lawrence Higgs, Pin Shuai, and Wenyi Sheng, for their unwavering support and assistance throughout the entire process. Additionally, I owe a debt of gratitude to faculty members and assistants, especially Bill Mace, whose assistance transcended the lab and beyond.

Furthermore, I extend my thanks to my previous major advisor, Masaru Sakai, and professors Kunio Watanabe and Nobuo Toride at Mie University, for their support and encouragement in providing me with the opportunity to apply to Utah State University.

I am grateful to the individuals with whom I shared office and lab space, who not only helped my academic life but also made this office feel like home: Hiroaki Shimada, Rong Zhou, Idowu Ateloye, Kshitij Parajuli, Morteza Sadeghi, Masoumeh Hashemi, Phearen Miller, Justin Allred, Krishna Borhara, Vishal Singh, Li-Ting (Mila) Yen, Shannon Rauter, Brendan Fatzinger, Asmita Paudel, Samikshya Pyakurel, Tina Sullivan, Megan Baker, Chieh-Yun (Carolin) Chang, Ji-Jhong (JJ) Chen, Juan Domingo Gonzalez,

and Sarah Schreck. Special thanks also go to my friends, Hsin and Yurika, and their children, Yuuta and Airi, as well as Charlie Hellberg and Jona Odulio, whose encouragement, moral support, and patience were invaluable as I progressed from the initial proposal writing to the final document.

I am grateful for the financial support provided by the National Aeronautics and Space Administration (NASA), the Department of Plants, Soils, and Climate and the Graduate School of Utah State University.

A special thanks is due to my family for encouraging me to pursue graduate studies and for believing in my abilities. My deepest appreciation goes to my best friend and husband, Sam, for his unwavering patience, honesty, love, and support until the completion of this dissertation.

To each and every one of you mentioned, and to those whose contributions may not be explicitly acknowledged, I extend my sincerest gratitude. This accomplishment would not have been possible without your unwavering support.

Chihiro Dixon

CONTENTS

	Page
Abstract	ii
Public Abstract.....	v
Dedication.....	vii
Acknowledgment	viii
List Of Tables	xii
List Of Figures	xv
Chapter I. Introduction.....	1
Chapter II. Standardizing Heat Pulse Probe Measurements for Thermal Property Determination Using Ice and Water	13
Abstract	13
Introduction	14
Theory	18
Materials and Methods	20
Results and Discussion	26
Conclusions	33
References	35
Chapter III. Thermal Property Standards Using Granular Media with Air-Pluviation and Heat Pulse Probe Measurements	47
Abstract	47
Introduction	48
Theory	52
Materials and Methods	58
Results and Discussion	64
Conclusions	72
References	74
Chapter IV. Automated Hanging Water Column for Characterizing Water Retention and Hysteresis of Coarse-Textured Porous Media.....	90
Abstract	90

Introduction	91
Theoretical	93
Materials and Methods	94
Results and Discussion	101
Conclusions	106
References	108
Chapter V. Characterizing Hysteretic Water Retention of Synthetic- and Natural-Fiber as Candidate Plant Growth Media	120
Abstract	120
Introduction	121
Theoretical	124
Materials and Methods	126
Results	132
Discussion	137
Conclusions	142
References	145
Chapter VI. A Plant-Optimal Irrigation System for Reduced Gravity Conditions	159
Abstract	159
Introduction	160
Theoretical	163
Materials and Methods	165
Results	172
Discussion	175
Conclusions	177
References	180
Chapter VII. Conclusion	192
Appendices.....	196
Appendix A CR-BASIC Program for the Automated Hanging Water Column Measurements	197
Appendix B Coauthor Approval Letters	210
Curriculum Vitae	213

LIST OF TABLES

Table	Page
Chapter II	
1 Comparison of rod dimensions and volumetric heat capacities of the HPP components	40
2 Thermal properties of ice and water as functions of temperature using polynomial equations (all $r^2 = 0.99$) generated by curve fitting software (TableCurve 2D, Systat Software Inc.) and coefficients fitted to 10°C increment data presented by Haynes (2016).....	41
3 Physical rod spacing (r_{phy}) and the average calibrated spacing (r_c) and standard deviation (Std.) are presented for air-free ice and agar-stabilized water.	42
4 Computed average, standard deviation, RMSE, TE, and RE to the reference thermal properties of ice and water with different r_c using the ILS and ICPC model.	43
Chapter III	
1 Particle- and bulk densities (ρ_s and ρ_b), porosity and quartz (SiO ₂) fraction of granular media.	80
2 Calibrated apparent rod spacing in agar-stabilized water (r_c) and thermistor rod dimensions and volumetric heat capacities of the THPP components (after Naruke et al. (2021)).	81
3 Diameters through which, respectively, 90%, 50% and 10% of the selected granular media passed.....	81
4 Average and standard deviation (Stdev) of estimated C_v and λ , calculated $\kappa (= C_v/\lambda)$ in granular media at oven-dry, saturated- and drained- water content (θ_w) conditions using the THPP measurements.	82
5 Estimated thermal parameters for thermal property functions.....	83
6 RMSE and bias of thermal property functions in various testing media.	84
Chapter IV	
1 Particle size range, particle density (ρ_s), bulk density (ρ_b) and computed	

porosity ($\varphi = 1 - \rho_b/\rho_s$) of quartz sand.	112
2 Hysteretic water retention parameters (van Genuchten, 1980) for the initial drying (d0)-, main drying (d)- and main wetting (w)-curves of quartz sand.	113
3 Water retention parameters (van Genuchten, 1980) for quartz sand (Accusand) (after Schroth et al. (1996)).	114

Chapter V

1 Fibrous media's compositions, structure, <i>GSM</i> , thickness and number of layers used for the automated water retention measurements.	152
2 Mean and standard error values of effective particle size distribution of peat moss.	153
3 Physical properties including material density (ρ_s), bulk density (ρ_b) and computed porosity ($\varphi = 1 - \rho_s / \rho_b$).	153
4 Water retention parameters of the van Genuchten (1980) model for the initial drying (d0)-, main drying (d)- and main wetting (w)-processes.	154
5 The average and standard deviation values of triplicated <i>h</i> measurements and the plant dry shoot mass per unit area (g cm^{-2}) in synthetic woven fibers.	155

Chapter VI

1 Physical properties including particle size distribution, particle density (ρ_s), bulk density (ρ_b) and the computed porosity ($\varphi = 1 - \rho_b/\rho_s$) and hysteretic water retention parameters for the van Genuchten (1980) model and the computed target volumetric water content (θ_t) and matric potential (h_t) in Profile, Turface and Mix.	184
2 Potential components of the plant-optimal irrigation system comprised of the porous cup in the media, the check valve ($H_{cv} = 9.1$ cm) and the water reservoir under Earth's gravity condition.	185
3 Target matric potential (h_t) computed from the drying water retention character, the threshold hydraulic potential to open the check valve (H_{cv}) with the standard error value and the air-inlet tube position (z_m) in the Mariotte's bottle computed with Equation 3 in Profile, Turface and Mix. ...	185
4 The average- and standard error-values of dry leaf mass per unit area (g cm^{-2}) in Profile, Turface and Mix.	186

- 5 Comparison of potential components of (a) the conventional Mariotte bottle irrigation system without the check valve under Earth's gravity condition and (b) the plant-optimal irrigation system with the check valve under reduced gravity (0g) condition as illustrated in Figure 4.187

LIST OF FIGURES

Figure	Page
Chapter II	
1 The cross-section of a Tri-needle Heat Pulse Probe (THPP) with two thermistor-rods (T_a and T_b) and one heater-rod.	44
2 Ice block showing air-free and air-entrained sections with THPP rods (the heater-rod and two thermistor-rods, T_a and T_b) in the air-free portion.	44
3 Comparison of the measured temperature rise at one thermistor-rod, T_a , and the fitted temperature rise as a function of time in air-free ice (-21°C) and agar-stabilized water (21°C).	45
4 Thermal-conductivity (λ) and volumetric heat capacity (C_v) from THPP estimates with the calibrated r_c in air-free ice (-21°C) using the ICPC model and resulting computed thermal diffusivity ($\kappa = \lambda/C_v$) (symbols).	46
Chapter III	
1 (a) A pictorial drawing of THPP, (b) a cross-section of THPP and (c) a pictorial drawing of a layered screen column.....	85
2 Particle size distribution of coarse granular media based on the parameters shown in Table 3.....	86
3 The volumetric heat capacity (C_v) function of water content determined by THPP (symbols) and the mixing model (lines) using the fitted parameter shown in Table 5.....	87
4 The average λ functions determined by THPP (symbols) with the black bar representing the standard deviation.	88
5 Volumetric heat capacity (C_v) and thermal- conductivity (λ) from THPP estimations as well as resulting computed thermal diffusivity ($\kappa = \lambda/C_v$) in coarse angular sand (symbols).....	89
Chapter IV	
1 (a) Automated water retention measurement system consisting of a compound pressure transducer, a diffuse laser mounted on a 10 cm linear actuator, a 50 ml burette attached to a 70 cm linear actuator, a fritted Buchner funnel, a T-slot-based outer aluminum frame and the control	

	panel and (b) a magnified picture of the coarse-textured porous medium water retention measurement system.....	115
2	Automated water retention measurement system flowchart	116
3	Cumulative particle distribution of graded sand.	117
4	Triplicated measurements of the automated hysteretic water retention in graded sand.	118
5	Hysteretic water retention measurements and fitted van Genuchten (1980) (VG) water retention models describing (a) C778 graded- and (b)–(h) sieved-quartz sand (ASTM-C778).....	119

Chapter V

1	Soilless media (left to right) including (a) synthetic fibers: Spa and Yoga (SY), The Gauntlet (GA), Creature Edgeless (CR), Platinum Pluffle (PL), Dry Me A River (DR), CapMat II (CA) and (b) natural fibers: jute (JU), linen (LI), cellulosic sponge (CE) and peat moss (PE).	156
2	(a) Initial setup and (b) post-harvesting plant growth media, Spa and Yoga.	157
3	Hysteretic water retention measurements (symbols) including the first drying process (d0) and repeated drying (d-repeat)- and repeated wetting (w-repeat)-processes as well as fitted van Genuchten (1980) water retention models (lines) describing (a)–(f) Synthetic fibers and (g)–(i) natural fibers.	158

Chapter VI

1	Calcined clay with three different particle size ranges: Profile (0.25–1 mm), Turface (1–2 mm) and Mix (0.25–2 mm).	188
2	(a) A top-down picture and (c) an illustration demonstrating the plant-optimal irrigation system with (b) Romaine lettuce cultivation.	189
3	Water retention curve for the drying (solid lines) and wetting (dash-dotted lines) processes in (a) Profile, (b) Turface and (c) Mix using the VG model parameters listed in Table 1, and the total 60 days of diurnal changes in the averaged value of triplicated matric potential (h) measurements at $z = 5$ cm (black solid lines), and the target matric potential (h_i) values (blue dash lines) and daily average value of h measurements (light blue circles) with the gray bars showing the standard deviation in (d) Profile, (e) Turface and (f) Mix.	190
4	The illustration of the comparison between (a) the capillary-driven	

irrigation using the Mariotte bottle under Earth gravity and (b) the plant-optimal irrigation using the check valve and collapsible water reservoir. ...191

CHAPTER I

INTRODUCTION

Space exploration stands as one of humanity's most profound endeavors, seeking to further our understanding of planetary geology, climate dynamics, and the potential for extraterrestrial life on celestial bodies like the Moon and Mars (Léveillé, 2010; Martínez et al., 2017; Smrekar et al., 2019). Alongside these missions, plant growth experiments have emerged as crucial endeavors, primarily focusing on sustainable plant production to support astronauts' dietary and mental well-being during long-term space missions (Haeuplik-Meusburger et al., 2014; Zabel et al., 2016). Despite advancements, long-term plant production challenges persist, particularly in achieving uniform distribution of fluids (water, dissolved nutrients, and gas) throughout the growth media (e.g., Johnson et al., 2021; Monje et al., 2003; Porterfield et al., 2003), leading to inconsistent root zone water status even in the latest plant growth system aboard the International Space Station (ISS), the Vegetable Production System (VEGGIE) (Massa et al., 2017) and Advanced Plant Habitat (APH) (Monje et al., 2020). For instance, the VEGGIE system, employing a non-powered, passive capillary-driven irrigation method faced issues with excess water and poor root zone aeration under reduced gravity conditions (Massa et al., 2017; Monje et al., 2020), highlighting the need for improved water management strategies.

Sensing Root Zone Water Status Under Reduced Gravity Conditions

Monitoring root zone water status is pivotal for effective water management. The Svet space greenhouse on the Russian Mir space station during the bio-regenerative life support system (BLSS) research pioneered the use of both thermal properties and matrix

potential for inferring volumetric water content of the root zone using Heat Pulse Probe (HPP) and tensiometer measurements during plant growth under reduced gravity conditions (Yendler et al., 1995; Bingham et al., 1996). The HPP offers valuable insights into thermal properties in extraterrestrial environments and has been utilized in other space missions like NASA's Mars InSight mission and the Phoenix Lander mission on Mars (Zent et al., 2009, 2010), and the European Space Agency's Rosetta spacecraft bound to Comet 67P (Marczewski et al., 2004; Nagihara et al., 2014).

Heat Pulse Probe (HPP) for Determining Thermal Properties

The HPP method has also been widely used for determining thermal properties and surrogate properties (i.e., water content) of materials (i.e., soils) on Earth. Scientific studies addressing HPP applications (He et al., 2018) have significantly increased since the introduction of the Dual-needle (also dual-rod) HPP (DHPP) analysis by Campbell et al. (1991). The DHPP comprises a line source heater rod and temperature-sensing rod(s), utilizing temporal temperature rise measurements in response to the heat pulse generated from the heater rod to derive thermal property values such as volumetric heat capacity (C_v), thermal diffusivity (κ), and thermal conductivity (λ) (Campbell et al., 1991). The surrogate property like volumetric water content is estimated based on the estimated thermal properties (Bristow, 1998). Therefore, the accuracy in estimating water content in the root zone relies on the accuracy of thermal property estimations.

Calibration Method for Heat Pulse Probe Using Air-Free Ice

The latest advancements (Kamai et al., 2015) propose a new model for more accurate thermal property determination while reducing calibration medium dependence (Knight et al., 2012, 2016). However, validating DHPP models remains challenging due to

the lack of readily available calibration media. While agar-stabilized water has been conventionally used (Campbell et al., 1991), the thermal properties of solids present a promising alternative calibration medium with a different range of thermal property values.

Standardizing Thermal Property Calibration Method Using Granular Media

Additionally, studies have explored on-site DHPP calibration in the field (Liu et al., 2013; Zhang et al., 2020). However, there is a gap between in-situ calibration in non-porous media (e.g., water and ice) and on-site calibration in heterogeneous field soils. Targeting commercially available granular media as standard calibration options could advance thermal property sensor development, albeit with challenges in achieving reproducible bulk density. Air-pluviation, demonstrated by Miura and Toki (1982), offers a promising method for establishing repeatable packed media conditions, crucial for accurate thermal property measurements.

Impact of Reduced Gravity on Hydraulic Properties and Water Retention Characteristics

In reduced gravity conditions, water transport through media primarily relies on capillarity, emphasizing the importance of hydraulic properties, particularly hysteretic water retention characteristics. The porous medium's water retention relates to a material's (i.e., soil) volumetric water content (θ) with a hydraulic energy state called matric potential (h) under saturated and unsaturated conditions. The hysteretic water retention character, which varies during drying and wetting processes (Pham et al., 2005), is particularly essential in plant production, where evapotranspiration and irrigation subject the media to these alternating conditions. Studies indicated that the hysteretic water retention characteristics observed on Earth are similarly applicable under reduced gravity conditions

(Heinse et al., 2005, 2007, 2015).

Exploring Fibrous Media for Plant Growth in Reduced Gravity Conditions

Recent plant growth experiments under reduced gravity conditions, including the Svet Space Greenhouse (Bingham et al., 2000) and VEGGIE (Massa et al., 2017), utilized fibrous media as an encasing or a wicking medium to ensure uniform water distribution. Studies also explored fibrous media as candidate plant growth media under both Earth gravity (Storck et al., 2019; Dirkes et al., 2021) and reduced gravity (Paradiso et al., 2020) conditions, characterized by their lightweight, affordability, availability, and porous structure, which offer several advantages as plant growth media. However, limited research exists on the water retention characteristics of fibrous media with a focus on plant growth media (Paradiso et al., 2020), necessitating further investigation for optimal growth media selection.

Automated Hysteretic Water Retention Measurement System

Conventional water retention measurements developed by Haines (1930) yield informative water retention characteristics within the practical control range of matric potential for plant growth in the controlled environment (i.e., $-100 < h < 0$ cm) (Pecanha et al., 2021; Heiskanen, 1995). However, the measurements rely on manual protocols and require a wait time to reach hydraulic equilibrium, making it laborious (Assouline, 2021). To address these limitations, the development of automated water retention curve measurements offers a precise alternative, utilizing a diffusive laser distance sensor, linear actuators, and a pressure transducer for efficient data collection.

Design and Evaluation of a Passive Irrigation System for Soilless Media

The irrigation control should be adjusted based on hysteretic water retention

characteristics of the growth medium and potentially, plant water requirements. The capillary-driven irrigation system (e.g., capillary mats/wicks, ebb and flow system, sub-irrigated planters) represents a traditional approach to maintaining root zone water status under Earth's gravity conditions (Semananda et al., 2018). Previously, check valve installations to the capillary-driven irrigation system under Earth's gravity, as demonstrated by Jones and Or (1998), maintained negative matric potential within containerized sand while cultivating wheat. A check valve enables one-way fluid transport based on the pressure gradient between the inlet and outlet. This system could compensate for the lack of gravitational potential under reduced gravity conditions, potentially addressing challenges associated with overwatering the root zone under reduced gravity conditions.

Research Hypotheses

This research proposed the following five hypotheses.

- 1) Solid ice exhibiting a significantly different thermal property compared to the conventional calibration media, agar-stabilized water, can be used to validate thermal property sensor calibration.
- 2) Granular media with highly reproducible bulk density can provide a wide range of water content-dependent thermal properties, which can serve as granular material calibration standards for thermal property sensors.
- 3) An automated hanging water column measurement system with linear actuators combined with a laser diffusive distance sensor and a tensiometer can verify and monitor the matric potential of the media and provide repeatable measurements of the hysteretic water retention curves of porous media.

- 4) Lightweight fibrous media exhibit water retention characteristics suitable for plant growth, warranting consideration as growth media.
- 5) A capillary-driven irrigation system can passively support plant growth using a target matric potential based on the porous media's water retention curve, which only requires a check valve as the control mechanism.

Research Objectives

My Ph.D. dissertation included the following five objectives.

- 1) Demonstrate and validate a novel calibration method for Heat Pulse Probes using air-free ice.
- 2) Develop and demonstrate a standardized heat pulse probe thermal property calibration method covering a range of water contents using granular media with reproducible packing density.
- 3) Design, fabricate, and validate an automated hysteretic water retention curve measurement system using standard quartz sand with different particle size ranges.
- 4) Characterize hysteretic water retention curves of fibrous media as candidate plant growth media.
- 5) Design and evaluate a passive irrigation system for soilless media based on maintaining a target matric potential set point.

REFERENCES

Assouline, S. 2021. What Can We Learn from the Water Retention Characteristic of a Soil Regarding Its Hydrological and Agricultural Functions? Review and Analysis of Actual Knowledge. *Water Resour Res* 57(12): e2021WR031026. doi: 10.1029/2021WR031026.

Bingham, G.E., S.B. Jones, D. Or, I.G. Podolski, M.A. Levinskikh, et al. 2000. Microgravity effects on water supply and substrate properties in porous matrix root support systems. *Acta Astronaut* 47(11): 839–848. doi: 10.1016/S0094-5765(00)00116-8.

Bingham, G.E., F.B. Salisbury, W.F. Campbell, J.G. Carman, D.L. Bubenheim, et al. 1996. The Spacelab-Mir-1 “Greenhouse-2” experiment. *Advances in Space Research* 18(4–5): 225–232. doi: 10.1016/0273-1177(95)00881-E.

Bristow, K.L. 1998. Measurement of thermal properties and water content of unsaturated sandy soil using dual-probe heat-pulse probes. *Agric For Meteorol* 89(2): 75–84. doi: 10.1016/S0168-1923(97)00065-8.

Campbell, G.S., C. Calissendorff, J.H. Williams, R.M. Newman, G.J. Kluitenberg, et al. 1991. Probe for Measuring Soil Specific Heat Using A Heat-Pulse Method. *Soil Science Society of America Journal* 55(1): 291–293. doi: 10.2136/sssaj1991.03615995005500010052x.

Dirkes, L., J.D. Massanés, R. Böttjer, J.L. Storck, and A. Ehrmann. 2021. Outdoor vertical farming on textile substrates. *IOP Conf Ser Mater Sci Eng* 1031(1): 012020. doi: 10.1088/1757-899X/1031/1/012020.

Haeuplik-Meusburger, S., C. Paterson, D. Schubert, and P. Zabel. 2014. Greenhouses and their humanizing synergies. *Acta Astronaut* 96(1): 138–150. doi:

10.1016/j.actaastro.2013.11.031.

Haines, W.B. 1930. Studies in the physical properties of soil. V. The hysteresis effect in capillary properties, and the modes of moisture distribution associated therewith. *J Agric Sci* 20(1): 97–116. doi: 10.1017/S002185960008864X.

He, H., M.F. Dyck, R. Horton, T. Ren, K.L. Bristow, et al. 2018. Development and Application of the Heat Pulse Method for Soil Physical Measurements. *Reviews of Geophysics* 56(4): 567–620. doi: 10.1029/2017RG000584.

Heinse, R., S.D. Humphries, R.W. MacE, S.B. Jones, S.L. Steinberg, et al. 2005. Measurement of porous media hydraulic properties during parabolic flight induced microgravity. SAE International.

Heinse, R., S.B. Jones, D. Or, I. Podolskiy, T.S. Topham, et al. 2015. Microgravity Oxygen Diffusion and Water Retention Measurements in Unsaturated Porous Media aboard the International Space Station. *Vadose Zone Journal* 14(6): vzj2014.10.0135. doi: 10.2136/vzj2014.10.0135.

Heinse, R., S.B. Jones, S.L. Steinberg, M. Tuller, and D. Or. 2007. Measurements and Modeling of Variable Gravity Effects on Water Distribution and Flow in Unsaturated Porous Media. *Vadose Zone Journal* 6(4): 713–724. doi: 10.2136/vzj2006.0105.

Heiskanen, J. 1995. Physical properties of two-component growth media based on Sphagnum peat and their implications for plant-available water and aeration. *Plant Soil* 172(1): 45–54.

Johnson, C.M., H.O. Boles, L.E. Spencer, L. Poulet, M. Romeyn, et al. 2021. Supplemental Food Production With Plants: A Review of NASA Research. *Frontiers in Astronomy and Space Sciences* 8. doi: 10.3389/fspas.2021.734343.

Jones, S.B., and D. Or. 1998. A capillary-driven root module for plant growth in microgravity. *Advances in Space Research* 22(10): 1407–1412. doi: 10.1016/S0273-1177(98)00215-4.

Kamai, T., G.J. Kluitenberg, and J.W. Hopmans. 2015. A Dual-Probe Heat-Pulse Sensor with Rigid Probes for Improved Soil Water Content Measurement. *Soil Science Society of America Journal* 79(4): 1059–1072. doi: 10.2136/sssaj2015.01.0025.

Knight, J.H., G.J. Kluitenberg, and T. Kamai. 2016. The dual probe heat pulse method: interaction between probes of finite radius and finite heat capacity. *J Eng Math* 99(1): 79–102. doi: 10.1007/S10665-015-9822-X.

Knight, J.H., G.J. Kluitenberg, T. Kamai, and J.W. Hopmans. 2012. Semianalytical Solution for Dual-Probe Heat-Pulse Applications that Accounts for Probe Radius and Heat Capacity. *Vadose Zone Journal* 11(2). doi: 10.2136/vzj2011.0112.

Léveillé, R. 2010. A half-century of terrestrial analog studies: From craters on the Moon to searching for life on Mars. *Planet Space Sci* 58(4): 631–638. doi: 10.1016/j.pss.2009.04.001.

Liu, G., M. Wen, X. Chang, T. Ren, and R. Horton. 2013. A Self-Calibrated Dual Probe Heat Pulse Sensor for In Situ Calibrating the Probe Spacing. *Soil Science Society of America Journal* 77(2): 417–421. doi: 10.2136/SSSAJ2012.0434N.

Marczewski, W., K. Schröer, K. Seiferlin, B. Usowicz, M. Banaszkiewicz, et al. 2004. Prelaunch performance evaluation of the cometary experiment MUPUS-TP. *J Geophys Res Planets* 109(E7). doi: 10.1029/2003JE002192.

Martínez, G.M., C.N. Newman, A. De Vicente-Retortillo, E. Fischer, N.O. Renno, et al. 2017. The Modern Near-Surface Martian Climate: A Review of In-situ Meteorological

Data from Viking to Curiosity. *Space Sci Rev* 212(1–2): 295–338. doi: 10.1007/s11214-017-0360-x.

Massa, G.D., N.F. Dufour, J.A. Carver, M.E. Hummerick, R.M. Wheeler, et al. 2017. VEG-01: Veggie hardware validation testing on the international space station. *Open Agric* 2(1): 33–41. <https://www.degruyter.com/document/doi/10.1515/opag-2017-0003/html> (accessed 16 May 2021).

Miura, S., and S. Toki. 1982. A Sample Preparation Method and its Effect on Static and Cyclic Deformation-Strength Properties of Sand. *Soils and Foundations* 22(1): 61–77. doi: 10.3208/SANDF1972.22.61.

Monje, O., J.T. Richards, J.A. Carver, D.I. Dimapilis, H.G. Levine, et al. 2020. Hardware Validation of the Advanced Plant Habitat on ISS: Canopy Photosynthesis in Reduced Gravity. *Front Plant Sci* 11: 673. doi: 10.3389/FPLS.2020.00673/BIBTEX.

Monje, O., G.W. Stutte, G.D. Goins, D.M. Porterfield, and G.E. Bingham. 2003. Farming in space: Environmental and biophysical concerns. *Advances in Space Research* 31(1): 151–167. doi: 10.1016/S0273-1177(02)00751-2.

Nagihara, S., M. Hedlund, K. Zacny, and P.T. Taylor. 2014. Improved data reduction algorithm for the needle probe method applied to in-situ thermal conductivity measurements of lunar and planetary regoliths. *Planet Space Sci* 92: 49–56. doi: 10.1016/J.PSS.2013.12.012.

Paradiso, R., A. Ceriello, A. Pannico, S. Sorrentino, M. Palladino, et al. 2020. Design of a Module for Cultivation of Tuberous Plants in Microgravity: The ESA Project “Precursor of Food Production Unit” (PFPU). *Front Plant Sci* 11: 417. doi: 10.3389/fpls.2020.00417.

Peçanha, D.A., T.P.L. da Cunha-Chiamolera, Y. Chourak, E.Y. Martínez-Rivera, and M. Urrestarazu. 2021. Effect of the Matric Potential on Growth and Water, Nitrate and Potassium Absorption of Vegetables under Soilless Culture. *J. Soil Sci. Plant Nutr.* 21(4): 3493–3501. doi: 10.1007/S42729-021-00622-W/FIGURES/4.

Pham, H.Q., D.G. Fredlund, and S.L. Barbour. 2005. A study of hysteresis models for soil-water characteristic curves. <https://doi.org/10.1139/t05-071> 42(6): 1548–1568. doi: 10.1139/T05-071.

Porterfield, D.M., G.S. Neichitailo, A.L. Mashinski, and M.E. Musgrave. 2003. Spaceflight hardware for conducting plant growth experiments in space: The early years 1960-2000. *Advances in Space Research* 31(1): 183–193. doi: 10.1016/S0273-1177(02)00752-4.

Semananda, N., J. Ward, and B. Myers. 2018. A Semi-Systematic Review of Capillary Irrigation: The Benefits, Limitations, and Opportunities. *Horticulturae* 4(3): 23. doi: 10.3390/horticulturae4030023.

Smrekar, S.E., P. Lognonné, T. Spohn, W.B. Banerdt, D. Breuer, et al. 2019. Pre-mission InSights on the Interior of Mars. *Space Sci Rev* 215(1): 3. doi: 10.1007/s11214-018-0563-9.

Storck, Böttjer, Vahle, Brockhagen, Grothe, et al. 2019. Seed Germination and Seedling Growth on Knitted Fabrics as New Substrates for Hydroponic Systems. *Horticulturae* 5(4): 73. doi: 10.3390/horticulturae5040073.

Yendler, B.S., G. Bingham, S. Jones, and I. Podolsky. 1995. Moisture sensor for use in microgravity. *SAE Technical Papers*. doi: 10.4271/951471.

Zabel, P., M. Bamsey, D. Schubert, and M. Tajmar. 2016. Review and analysis of

over 40 years of space plant growth systems. Elsevier Ltd.

Zent, A.P., M.H. Hecht, D.R. Cobos, G.S. Campbell, C.S. Campbell, et al. 2009. Thermal and Electrical Conductivity Probe (TECP) for Phoenix. *J Geophys Res Planets* 114(E3). doi: 10.1029/2007JE003052.

Zent, A.P., M.H. Hecht, D.R. Cobos, S.E. Wood, T.L. Hudson, et al. 2010. Initial results from the thermal and electrical conductivity probe (TECP) on Phoenix. *J Geophys Res Planets* 115(E3): 0–14. doi: 10.1029/2009JE003420.

Zhang, M., Y. Lu, T. Ren, and R. Horton. 2020. In-situ probe spacing calibration improves the heat pulse method for measuring soil heat capacity and water content. *Soil Science Society of America Journal* 84(5): 1620–1629. doi: 10.1002/SAJ2.20124.

CHAPTER II

STANDARDIZING HEAT PULSE PROBE MEASUREMENTS FOR THERMAL
PROPERTY DETERMINATION USING ICE AND WATER

ABSTRACT

The growing demand for Heat Pulse Probes (HPP) to estimate thermal properties and surrogate soil processes comes with a need for improved standards for calibration and validation in reference materials. This study proposed air-free ice as a calibration material to determine the apparent rod spacing (r_c) for HPP. The advantage of using air-free ice as a calibration standard over agar-stabilized water stems from the fact that at 0°C ice provides a reference volumetric heat capacity ($C_v = 1.93 \text{ MJ m}^{-3} \text{ }^\circ\text{C}^{-1}$), less than half that of water ($C_v = 4.22 \text{ MJ m}^{-3} \text{ }^\circ\text{C}^{-1}$), while ice provides a four times larger reference thermal conductivity value ($\lambda = 2.16 \text{ W m}^{-1} \text{ }^\circ\text{C}^{-1}$) relative to that of water ($\lambda = 0.56 \text{ W m}^{-1} \text{ }^\circ\text{C}^{-1}$), which leads to a sharper peak temperature rise curve that may improve thermal property estimates in ice compared to the elongated peak obtained in water. We performed r_c calibrations with air-free ice in a freezer at -21°C and agar-stabilized water at 21°C using both *Infinite-Line Source* (ILS) and *Identical-Cylinders Perfect-Conductors* (ICPC) models to fit λ and C_v to temperature rise data and compute thermal diffusivity (κ) from the fitted λ and C_v (i.e., $\kappa = \lambda/C_v$). Results showed that the ICPC model yielded similar r_c values in both air-free ice and agar-stabilized water with reduced Total Error (TE) in estimating λ , C_v , and κ compared to results with the conventional ILS model. We suggest air-free ice as another standard for HPP rod spacing calibration and sensor-based thermal property

validation.

1. INTRODUCTION

Heat pulse probes (HPPs) have been widely used for in situ measurement of thermal properties as well as for the determination of a variety of indirect properties and processes of porous materials (e.g., soils). Scientific studies addressing HPP applications (He et al., 2018) have significantly increased since the introduction of the dual-needle (also dual-rod) HPP (DHPP) analysis by Campbell et al. (1991). Historically, the thermal conductivity (λ), volumetric heat capacity (C_v), and thermal diffusivity (κ) have been determined by fitting a heat transfer model to the temporal temperature response data given a known energy input.

The basic HPP consists of one line-source heater rod and one parallel temperature sensing rod. Research-related HPPs are custom-made consisting of between 2 and 11 parallel rods, while some commercial HPPs are also available with two or more rods (e.g., SH-3, Meter Group, Inc., Pullman, WA, USA). Applications of HPPs with a varied number of temperature-sensing-rods have been employed to simultaneously estimate properties or processes in porous media, such as soil moisture (Campbell et al. 1991), heat flux (Cobos and Baker, 2003), heat storage (Ochsner et al., 2007), water flux (Ren et al., 2000; Hopmans et al., 2002; Ochsner et al., 2003; Kamai et al., 2008; Knight et al., 2012; Yang et al., 2013), and subsurface evaporation rate (Heitman et al., 2008) in addition to the thermal properties (Bilskie et al., 1998; Bristow et al., 1994a). Beyond traditional HPP measurements, additional needles for bulk soil electrical conductivity (EC) measurements, using a Wenner array, were coupled with HPP measurements (Mori et al., 2003, 2005; Mortensen et al., 2006). Thermo-time domain reflectometry (T-TDR), first introduced by

Noborio et al. (1996), couples HPP measurements with TDR measurements to determine permittivity, soil water content, thermal properties, electrical conductivity, bulk density, and porosity (Ren et al., 1999, 2003; Sheng et al., 2017; Peng et al., 2019). Here we will refer to a Dual-needle HPP (DHPP), a Tri-needle HPP (THPP), as well as a Penta-needle HPP (PHPP) with the latter two HPP types having one heater rod with additional temperature-sensing rods.

A commonly used HPP model employed for fitting thermal properties considers the heater-rod as an infinite line source of instantaneous heat over a finite time interval (Campbell et al., 1991; Bristow et al., 1994). Campbell et al. (1991) first demonstrated the *Infinite Line Source* (ILS) theory with a pulse of heat from the heater- to a temperature-sensing rod for determining C_v . Kluitenberg et al. (1993) and Bristow et al. (1994b) improved the approach to simultaneously estimate λ , C_v , and κ based on the same theory. However, recent HPP designs (Kamai et al., 2015; Peng et al., 2019) involved thicker stainless-steel rods to minimize probe deflections. These thicker rods are a further deviation from the conventional ILS theory that assumes an infinitely small rod diameter with zero heat capacity. A new model has been developed and tested that includes the influence of rod properties accounting for rod and epoxy geometries along with their respective heat capacities (Knight et al., 2012). This new semi-analytical HPP model is called the *Identical-Cylinders Perfect-Conductors* (ICPC) model and will be discussed in more detail later.

Among common materials found on Earth, ice and water are the most widely studied, and their thermal properties have been determined by various methods leading to what are now well-defined specific heat (c), C_v , λ , and κ values (e.g., see Haynes, 2016).

Ice has the potential to become a viable calibration material with lower C_v ($1.93 \text{ MJ m}^{-3} \text{ }^\circ\text{C}^{-1}$ at 0°C) and higher λ ($2.16 \text{ W m}^{-1} \text{ }^\circ\text{C}^{-1}$ at 0°C), which exhibits a sharper temperature rise observation relative to the traditionally employed agar-stabilized water calibration. However, the challenge is to create ice without air bubbles since ice containing air bubbles may lead to a calibration medium with vastly different thermal properties. Past studies have not explored HPP calibration in air-free ice nor provided a protocol for making air-free ice. Furthermore, temperature rise analysis using the ICPC and ILS models provides validation of the HPP's thermal property estimation in both ice and water, where those properties are substantially different between liquid and solid phases of water.

For HPPs, the apparent distance, r_c , between the heat source and the temperature-sensing-rod (center-to-center) must be calibrated to accurately determine thermal properties from the measured temperature rise data. In both the ILS and ICPC models with known heat input and r_c values, two of the three thermal properties, i.e., λ , C_v , and κ , are determined by fitting the solution to the captured temperature rise data, and the third property can be calculated from the relationship of $C_v = \lambda/\kappa$. The r_c calibration using the ILS model with known C_v of a given material was originally developed by Campbell et al. (1991), and is now widely recognized as the standard calibration method. The calibrated r_c is not necessarily equal to the physically measured rod spacing, r_{phy} . The standard calibration method uses agar-stabilized water ($2\text{--}6 \text{ g L}^{-1}$ agar) at a constant temperature of 20°C , where the thermal properties of water are assumed, being $\lambda = 0.598 \text{ W m}^{-1} \text{ }^\circ\text{C}^{-1}$, $C_v = 4.18 \text{ MJ m}^{-3} \text{ }^\circ\text{C}^{-1}$, and $\kappa = 0.143 \text{ mm}^2 \text{ s}^{-1}$.

Later, Ham and Benson (2004) demonstrated the dependence of r_c on the C_v of the calibration material based on the ILS model, where r_c increased as C_v decreased. For

example, they observed that $r_c > r_{phy}$ in dry glass beads while $r_c < r_{phy}$ in both saturated glass beads and agar-stabilized water. Knight et al. (2012) clarified that the C_v of the rod (C_0) to the C_v of the material under test, defined here as $\beta_0 (= C_0/C_v)$ has a substantial effect on the temperature response in the ICPC model, which accounts for the rod's diameter and C_0 , therefore the conventional ILS model exhibits the dependence of r_c on the C_v of the test media. For example, r_c was found to increase with β_0 when $\beta_0 > 1$, which is the case when the C_v of the material (e.g., dry glass beads) is smaller than the C_v of the rod. However, r_c decreases with β_0 when $\beta_0 < 1$ (e.g., saturated glass beads and agar-stabilized water). Knight et al. (2012) mentioned that the ICPC model can minimize the dependence of r_c on the C_v of the calibration media, and the ICPC model might even eliminate the need to calibrate r_c . Peng et al. (2019) demonstrated that the T-TDR sensor using the ICPC model analysis performed well without calibrating r_c and instead, using the physically measured rod spacing ($r_c = r_{phy}$) in various soil types, both disturbed and intact samples, exhibited within the $\pm 10\%$ error range in determining C_v of samples compared to the modeled C_v (De Vries, 1963). There is a need to verify the r_c dependence and thermal property estimation using the ICPC model with a comparison of the conventional ILS model to reference thermal properties. The effect of agar concentration on the thermal properties of water has been largely ignored, but Zhang et al., (2011) showed that λ of agar-stabilized water increased by 3% at an agar concentration of 1 g L^{-1} , while it decreased by 2 % and 6 % at agar concentrations of 5 and 10 g L^{-1} , respectively, compared to their reference measurements of λ in ultrapure-water under room temperature. The lack of thermally stable and standardized calibration media having well-defined thermal properties as well as having a repeatable protocol makes calibrating r_c and validating thermal property determinations

challenging.

The objectives of this study were to 1) identify a method for creating a repeatable reference standard of air-free ice; 2) calibrate r_c in air-free ice and compare it to that calibrated in agar-stabilized water as well as to r_{phy} using the ICPC and ILS models; 3) validate the HPP estimation of thermal properties for ice and water.

2. THEORY

2.1 Heat transfer model

The ILS model is the most commonly applied theory for HPP simulation of temperature change ΔT ($^{\circ}\text{C}$) measured at the apparent distance r_c (m) from the line-source heater in a porous medium. It is based on the heat conduction equation with a short-duration heat input, t_0 (s), and infinite line source of heat, q' (W m^{-1}), propagating through a homogeneous and isotropic medium (Bristow et al., 1994b), written as

$$\Delta T(t) = \begin{cases} -\frac{q'}{4\pi\lambda} Ei\left(-\frac{r_c^2}{4\kappa t}\right) & 0 < t \leq t_0 \\ \frac{q'}{4\pi\lambda} \left\{ Ei\left[-\frac{r_c^2}{4\kappa(t-t_0)}\right] - Ei\left(-\frac{r_c^2}{4\kappa t}\right) \right\} & t > t_0 \end{cases} \quad (1)$$

where t is the elapsed time (s) from the heat pulse application and $Ei(z)$ is the exponential function of argument z . The short-duration heat application used here for the ILS approach (also referred to as Pulsed Infinite Line Source or PILS) is distinguished from the continuous heat application method. A source of error for the ILS model is the assumption that a heat pulse is instantaneously applied from a line-source heater with zero radius and non-existent C_v . In reality, however, the finite physical and thermal properties of the rods may alter the resulting temperature rise to some degree.

Knight et al. (2012) proposed a semi-analytical solution to the temperature rise

function of time at the temperature-sensing-rod based on the Laplace transform referred to as the identical-cylinders perfect-conductors (ICPC) model, written as

$$\hat{T}_C(p) = \frac{q' K_0(\mu r_c)}{2\pi\lambda p \left\{ \mu a_0 \left[K_1(\mu a_0) + \left(\frac{\mu a_0 \beta_0}{2} \right) K_0(\mu a_0) \right] \right\}^2} \quad (2)$$

where p is the Laplace transform variable (s^{-1}) and $\hat{T}_C(p)$ is the Laplace transform of the temperature at the temperature-sensing-rod, $T_C(t)$, for the case of continuous heating. Also, $K_n(z)$ is the modified Bessel function of the second kind of order n and argument z , $\mu = \sqrt{p/\kappa}$, a_0 is the radius of the rod (m), $\beta_0 = C_0/C_v$. The weighting average volumetric heat capacity of the rod, C_0 , including stainless-steel and epoxy was calculated as:

$$C_0 = C_E \frac{d_E^2}{d_0^2} + C_{SS} \left(1 - \frac{d_E^2}{d_0^2} \right) \quad (3)$$

where C_E and C_{SS} are volumetric heat capacities of rod-epoxy and -stainless-steel and d_E and d_0 are the inner and outer diameter of the stainless-steel rod, respectively. Based on the principle of superposition, the temperature increase from pulsed heating can be calculated as:

$$\Delta T(t) = \begin{cases} \Delta T_C(t) & 0 < t \leq t_0 \\ \Delta T_C(t) - \Delta T_C(t - t_0) & t > t_0 \end{cases} \quad (4)$$

This solution accounts for the effect of a finite rod radius and the finite heat capacity of both heater- and temperature-sensing-rod including the stainless-steel tubing and the epoxy. The ICPC model becomes identical to the ILS model of Bristow et al. (1994) if the radius of both heater- and temperature-sensing-rod become zero ($a_0 = 0$). The introduction of finite rod radius (a_0) and β_0 accounts for the shift of heat-pulse arrival at the temperature-sensing-rods relative to the ILS model, reducing the bias of thermal property estimation in

materials with a varied range of thermal properties.

2.2 Accuracy and bias of thermal property estimations

The significance of the calibration for r_c among rods T_a and T_b , as well as the accuracy of thermal property estimates in air-free ice (-21°C) and agar-stabilized water (21°C), was evaluated using Root Mean Square Error (RMSE) and Total Error (TE) calculations, written as:

$$\text{RMSE} = \sqrt{\frac{\sum(A_e - A_r)^2}{n}} \quad (5)$$

$$\text{TE} = \sqrt{\text{stdev}^2 + \text{MSE}} \quad (6)$$

where A_e is the estimated r_c or thermal property based on either the ILS (Eq. 1) or the ICPC (Eqs. 2 and 4) model and A_r is the measured r_{phy} or reference thermal property and n is the number of measurements. The TE accounts for the combination of both random and systematic errors, which represents the square root of the sum of standard deviation (stdev) and mean squared error ($\text{MSE} = \text{RMSE}^2$). The significance of the errors was expressed using TE and the ratio of TE to A_e is defined here as the Relative Error, RE ($\text{RE} = \text{TE}/A_r$).

3. MATERIALS AND METHODS

3.1 Heat Pulse Probe Construction and Measurements

Table 1 lists details of past and present HPP designs (Campbell et al., 1991; Ham and Benson, 2004; Yang et al., 2013; Kamai et al., 2015; Peng et al., 2019), including r_{phy} , rod length, external and internal diameter, and C_v of stainless-steel, filling epoxy, and C_o , which was calculated using Eq. 3. The design of the HPP rods tends to be longer and thicker

than the original HPP sensor (DHPP_C) by Campbell et al. (1991). Peng et al. (2019) demonstrated the THPP_P combined with the TDR technique to have 1.75 times longer and 2.9 times thicker rods compared to the original DHPP_C. Yang et al. (2011) applied the PHPP_Y which had a heater-rod orthogonally surrounded by four thermistor-rods. Kamai et al. (2015) used the conventional DHPP (C-DHPP_K), which followed the design by Tarara and Ham (1997), as well as the rigid DHPP (R-DHPP_K) with longer and thicker rods than the C-DHPP_K.

We constructed a THPP following the design used by Kamai et al. (2015) but used thicker rods, which helped to increase C_0 from $3.68 \text{ MJ m}^{-3} \text{ }^\circ\text{C}^{-1}$ for the R-DHPP_K to $3.87 \text{ MJ m}^{-3} \text{ }^\circ\text{C}^{-1}$ for our THPP. Three stainless steel rods (316 stainless steel, McMaster-Carr, Douglasville, GA, USA) with the dimensions of 2.40 mm O.D. and 0.61 mm I.D. (wall thickness = 0.90 mm) were used. Each of the two temperature-sensing-rods contained a single thermistor (10K3MCD1, BetaTherm Corp., Shrewsbury, MA, USA) positioned in the middle of the exposed rod length. The heater-wire was made from a 40 gauge (diameter = 0.0787 mm) enameled Nichrome resistance wire (Nichrome 80, Pelican Wire Co., Naples, FL, USA) with a constant resistance per wire length ($221.9 \text{ } \Omega \text{ m}^{-1}$). The heater wire was folded in half to create a loop at the distal end of the rod. Both the heater- and thermistor-rods were filled with a thermally conductive epoxy (slow cure silver epoxy, Arctic Silver Inc., Visalia, CA, USA). Figure 1 shows a cross-sectional image of our THPP's heater-rod sandwiched between the two thermistor-rods. Letters T_a and T_b represent the two individual thermistor-rods that measure the temperature response from the central heater-rod. A 39 mm diameter polycarbonate disk of 10 mm thickness was drilled out to house the two thermistor-rods on either side of the heater-rod with a 7 mm

center-to-center spacing between each rod pair. The heater- and thermistor- rod wires protruding from the bottom of the disk were potted inside a 40-mm-I.D. ABS pipe using a 2-part potting epoxy (50-3100RBK-resin, CAT.150CL13-hardener, Epoxies, Etc., Cranston, RI, USA), where the polycarbonate disk was previously glued into the upper end of the pipe. The outer wall of the ABS pipe had two grooves machined at the upper end to house O-rings for sealing against a 150 mm long, 57 mm I.D. clear Lexan tube used to contain the agar-stabilized water being measured. After assembling all the components for the THPP, r_{phy} at the top, middle, and base of each heater-thermistor-rod pair (center-to-center) were measured by a digital caliper and the average r_{phy} spacing is presented in Table 1.

The heater wire of the THPP was connected in series with a 1- Ω precision resistor ($\pm 1\%$, 2 W), the voltage across which was measured by a CR6 datalogger (Campbell Scientific, Logan, UT, USA) for heating power calculation. The heating duration was 8 s with an average heating rate of $50.1 \pm 0.32 \text{ W m}^{-1}$. Our heating rate was relatively smaller than other HPP studies (i.e., Kamai et al., 2015) to avoid melting the ice, which would create a testing material consisting both water and ice leading to substantial calibration errors. The thermistors were measured directly through the differential channels on the datalogger using the built-in 5-k Ω resistor ($\pm 0.1\%$, 10 ppm $^{\circ}\text{C}^{-1}$) to complete the bridge. Thermistor temperatures were recorded for over 150 s, including 30 s prior to firing the heater and a continuation for 120 s to capture the heating peak in air-free ice and agar-stabilized water. The average pre-heating temperature collected for 5 seconds before the heat pulse was determined as the initial temperature. The 120 s of heating and post-heating temperature data were used to optimize thermal properties using ILS and ICPC models.

Measurements were initiated every 15 minutes so that the sample's temperature around the THPP could cool back down to near ambient temperature after heating to avoid temperature buildup or artificial thermal gradients. The temperature response and heating rate data were recorded for post-analysis of r_c and thermal properties.

3.2 Considerations for air-free ice creation

The creation of air-free ice is non-trivial and we found bartenders to be among the most skilled creators of clear ice using a variety of empirical approaches. Obtaining air-free ice can be challenging without understanding several principles associated with water and the freezing process: 1) water contains dissolved gas and the solubility of gas increases as temperature decreases; 2) dissolved air moves towards the ice-water interface during the freezing process, which may lead to bubble nucleation, growth of bubbles, and encapsulation (Lipp et al., 1987); 3) boiling or vacuuming the water temporarily reduces gas concentration in water but may not significantly improve the quantity of air-free ice because gas will diffuse back into the cooling water during the hours or days required for freezing; 4) one way to allow the gas to escape as the liquid volume diminishes is by freezing from the bottom of the water body upward (surface must remain unfrozen), which is a method used by commercial ice makers, requiring specialized machinery; 5) the more common and convenient approach for obtaining air-free ice is to freeze water in a conventional freezer from the top down; 6) a limitation of top-down freezing is that only about the top half of the total water depth will be air-free after complete freezing; 7) the top-down approach requires an insulated container that minimizes freezing from the bottom and sides of the container inward (i.e., in a non-insulated container, trapped air shows up in the center of the ice body rather than at the bottom, e.g., ice cubes); 8) rotationally-

molded coolers provide uniform insulation and thicker walls than conventional coolers, thus potentially improving results of the top-down freezing approach; 9) to provide air-free ice that fully encases the HPP rods for calibration and validation, the water depth in the cooler should be approximately 3 to 4 times that of the rod length, assuming HPP rods are suspended vertically downward into the water surface.

3.3 Liquid and Solid Reference Media

Agar-stabilized water provides a stable thermal property reference under room temperature as agar minimizes convective thermal gradients within the gel-like state of the water. We heated water mixed with 4 g L^{-1} agar (Bacto-agar, Difco Laboratories, Detroit, MI, USA) to the boiling point to ensure that the agar was completely dissolved in the water. The mixture was then cooled to around 50°C and then poured into a 10-cm long, 8-cm I.D. cylindrical plastic column to cool further. The THPP was centrally inserted facing downward with the rods completely immersed in the agar-stabilized water column. The THPP and column were then placed inside a styrofoam box to stabilize the temperature of the column during the THPP measurements.

We used a medium-sized chest freezer with a rotationally-molded cooler placed at the bottom of the freezer. The cooler lid was kept open and the cooler was water-filled to a depth of 20 cm. The THPP rods were submerged into the water surface of the cooler, suspended by a clamp and support system. The THPP sensor wires were run out of the cooler to the datalogger for recording temperature rise data for thermal property determination in ice. The freezer door was closed and we waited 3 days to ensure the entire water body was frozen and the ice had reached an equilibrium temperature with the freezer of -21°C . Figure 2 shows the THPP rods encased in the upper air-free portion of the ice

body. We note that the final temperature of ice should be low enough to prevent ice near the heater-rod from melting during the heat pulse as this melted water complicates the temperature rise data if heat propagates through a combination of ice and meltwater. For example, He et al. (2015) showed that ice melt during heating in frozen soil was eliminated when the ambient temperature of the partially frozen soil was below -5°C . Therefore, it is possible to calibrate THPP above -21°C (i.e., -10°C), although thermal properties in ice at -10 or -20°C are not substantially different. We recommend setting the freezer temperature at the minimum temperature setting to create stable temperature conditions in ice and to avoid melting around the heater-rod.

3.4 Data processing of measured temperature rise for parameter estimation

The r_c and thermal properties using the ILS and ICPC models were determined by minimizing the objective function (OF);

$$OF = \sum_{i=1}^n [\Delta T_S(t_i) - T_M(t_i, \mathbf{p})]^2 \quad (7)$$

where $\Delta T_S(t_i)$ is the temperature increase measurement by the thermistor-rod at time t_i , $T_M(t_i, \mathbf{p})$ is the temperature increase using the ILS and ICPC models, and \mathbf{p} is a vector containing optimized parameters. The parameter optimization was conducted using MATLAB code from Kamai et al. (2015), which is a combination of the single point method (Ren et al., 1999) and the entire temperature rise curve fitting method (Hopmans et al., 2002). This hybrid approach allowed the model to fit temperature rise data ± 5 s before and after the peak temperature rise including the peak temperature value, which provided 11 data points for the optimization. Late-time temperatures after the peak, i.e., all 120 s of data, were not included in the analysis based on the assumption that i) heat through

the sensor body and ii) a finite test sample size both distort those late-time temperature values (Kluitenberg et al., 1993; Kamai et al., 2015).

The r_c calibration and thermal property estimation using both ILS and ICPC models require a full dataset including temperature values, $q^?$, t_0 , and additional parameters of a_0 and C_0 for the ICPC model. We used $\mathbf{p} = (r_c, \lambda)$ for calibration in air-free ice at -21°C and in agar-stabilized water at 21°C . Values of C_v for air-free ice and agar-stabilized water were computed from temperature-dependent empirical polynomial functions we derived, which are described in the results section. Thermal property optimization was conducted using $\mathbf{p} = (\lambda, C_v)$ with the calibrated r_c values in air-free ice and agar-stabilized water as well as with r_{phy} . The third thermal property, κ , was calculated using optimized λ and C_v ($\kappa = \lambda/C_v$).

Each thermistor-rod provided triplicate temperature measurements under the target temperature, which resulted in 3 datasets for the r_c calibration from each thermistor-rod in addition to the combined 6 data points ($T_a + T_b$) for the THPP-derived thermal properties determination using both thermistor-rods.

4. RESULTS AND DISCUSSION

4.1 Reference temperature-dependent thermal properties of water and ice

The reference thermal properties (c , C_v , λ , and κ) of ice and water at different temperatures were empirically modeled and listed in Table 2 with $r^2 = 0.99$ for all thermal property functions. All data employed in Table 2 were entered with and fitted to five significant digits for accuracy. We note the discontinuity in modeled data at 0°C where thermal properties (c , C_v , λ , and κ) of ice and water at 0°C were: $c = 1.73$ and $4.18 \text{ J g}^{-1} \text{ }^\circ\text{C}^{-1}$, $C_v = 1.60$ and $4.04 \text{ MJ m}^{-3} \text{ }^\circ\text{C}^{-1}$, $\lambda = 2.16$ and $0.556 \text{ W m}^{-1} \text{ }^\circ\text{C}^{-1}$, and $\kappa = 1.12$ and $0.132 \text{ mm}^2 \text{ s}^{-1}$, respectively. In comparing these thermal property values, the c and C_v of

water are more than double the values of ice, while λ of water was one quarter λ of ice and finally κ of water was an order of magnitude less than κ of ice.

4.2 Temperature Rise Fitting in Water and Ice

Figure 3 presents the measured temperature rise recorded at one thermistor-rod, T_a , compared with the ILS- and ICPC-fitted curves in both air-free ice (-21°C) and agar-stabilized water (21°C). The C_v values of 1.79 and $4.18 \text{ MJ m}^{-3} \text{ }^\circ\text{C}^{-1}$ were input for air-free ice (-21°C) and agar-stabilized water (21°C), respectively, and were computed and applied to determine r_c using the corresponding equations and parameters presented in Table 3. The temperature rise data at the other thermistor-rod, T_b , exhibited an almost identical temperature rise response in agar-stabilized water while showing a slightly lower temperature rise in air-free ice compared to T_a . The maximum measured discrepancy in temperature between the two thermistor-rods was 0.05°C in air-free ice, which occurred 10 seconds after the heater firing, while for agar-stabilizer water the discrepancy was 0.002°C at 21 s after the heater firing. We will discuss these measurement discrepancies in more detail later.

The measured peak ΔT in air-free ice was about twice as much as the peak in agar-stabilized water, and the time duration to reach the peak in air-free ice was only 16 s while the duration in agar-stabilized water was about 79 s due to the combination of a smaller C_v and a larger κ of ice compared to those of water. The ΔT curve in air-free ice showed a distinctive spike, and the temperature rise fitting range for parameter optimization was between 0.39 and 0.47°C , in contrast to a flat curve in agar-stabilized water, with a much smaller temperature rise fitting range between 0.2313 and 0.2319°C , occasionally exhibiting a constant peak ranging over 2 to 3 s during measurements in agar-stabilized

water. Since our heat input ($q' = 50.1 \text{ W m}^{-1}$) was one-third of the heat intensity of Kamai et al. (2015), our peak value of ΔT in agar-stabilized water was also about one-third of their measured values. In theory, q' should not affect parameter optimization (Ham and Benson, 2004). However, the fluctuation in temperature measurements induced by the smaller q' can amplify errors in parameter optimization using agar-stabilized water. On the other hand, even with the small q' , the temperature rise range of values in air-free ice was much larger, i.e., 0.45°C of the peak temperature, which seems to be an advantage of using air-free ice as a calibration media when minimizing q' .

The ICPC model showed slightly improved fitting during the early temperature rise stage compared with the ILS model especially in agar-stabilized water, although the ICPC model in air-free ice showed a slight overestimation at the peak temperature in Figure 3. Kluitenberg et al. (1993) demonstrated that the ILS theory is not as applicable at late times because the physical temperature measurements are affected by the finite length of the rods and the sensor body, as well as by the sample container size. We compared different ΔT data ranges for parameter optimization especially in ice using the ICPC model (data not shown). The hybrid approach by Kamai et al. (2015), which only uses $\pm 5 \text{ s}$ around the peak temperature, provided the smallest errors in estimating both r_c and λ compared with a variety of pre- and post-peak data ranges. Although different fitting ranges provided slightly different ΔT fitted curves near the peak and the hybrid approach showed slight underestimations of the peak ΔT , different fitting ranges did not exhibit substantial changes in the overall temperature rise curves. Therefore, the hybrid approach can also be applicable for the r_c calibration as well as the thermal property optimization.

4.3 Apparent Rod Spacing Calibration in Ice and Water

Table 3 presents measured spacing, r_{phy} , and calibrated spacing, r_c , including the average value and standard deviation (Std.) determined in air-free ice and agar-stabilized water using the ILS and the ICPC models for a variety of rod configurations, which for our THPP probe included spacing results from both thermistor-rods. The differences between r_c values determined in air-free ice and agar-stabilized water ($r_{c_i} - r_{c_w}$) were also presented. Note that the standard deviations for different geometries of HPP listed in Table 1, were calculated from multiple rods with the same probe configurations. The average r_c for THPP was calculated by separating each thermistor-rod T_a and T_b and reporting for each thermistor-rod individually. We also present the measured thermal properties in air-free ice at horizontal and vertical orientations to observe the possibility of altered rod spacing from internal ice expansion.

One of the thermistor-rods, T_a , presented a 0.2 mm larger value of its average r_c than the other thermistor-rod, T_b , in air-free ice under vertical orientation. As expected, a similar trend where T_a exhibited a larger average r_c than T_b 's was also observed when the rods were horizontally oriented in air-free ice. This r_c difference between the two rods for both ILS and ICPC analysis is not consistent with results for agar-stabilized water where r_c for T_a and T_b were identical for both ILS and ICPC models. It is not clear where the T_a and T_b differences in r_c for ice measurements resulted, but perhaps the sharp temperature peak in air-free ice compared to the very broad peak in agar-stabilized water was a contributor. Since the calibrated r_c in each thermistor-rod exhibited different values, we recommend the r_c calibration be applied for each rod. The ILS model in air-free ice produced overestimations of r_c , relative to the estimated r_c from the ICPC model. Previous

studies with various sensor geometries showed that the r_c in agar-stabilized water using the ILS model was somewhat close to the r_{phy} , and Kamai et al. (2015) showed a slight increase of r_c using the ICPC model in agar-stabilized water. Our THPP also showed the average r_c using both ILS and ICPC models being close to the r_{phy} .

The average r_c using the ILS model in air-free ice increased by 0.45 mm compared with the average r_c in agar-stabilized water, in part, because the ILS model neglects the rod's diameter and C_v of the rod, and owing to the increase in C_v from $1.79 \text{ MJ m}^{-3} \text{ }^\circ\text{C}^{-1}$ in ice to $4.18 \text{ MJ m}^{-3} \text{ }^\circ\text{C}^{-1}$ in water. This r_c dependence using the ILS model was discussed in Ham and Benson (2004). However, the ICPC model fitting in air-free ice resulted in both a slight increase in T_a (0.05 mm) and a slight decrease in T_b (0.17 mm) in the average r_c compared to the average r_c in agar-stabilized water. This result is consistent with other studies suggesting that the r_c calibration using the ICPC model is less dependent on the r_c of the material's C_v compared to the ILS model.

4.4 Ice Expansion Impact on r_c

We wondered if a significant change in the physical or calibrated rod spacing in ice would result from the freezing process. The density of ice at -20°C is 0.92 g cm^{-3} (Haynes, 2016), suggesting the volume of ice expands by approximately 8% relative to a liquid state at 20°C . This translates to approximately a 0.5 mm shift in the 7 mm rod spacing. To evaluate freezing effects, we installed the THPP rods vertically and horizontally in the freezing water to see if any difference in r_c would be observed between the vertical- and horizontal-orientation under freezing conditions. For vertical installation, the rods were positioned at the center of the cooler in the top portion of the water body whereas, for the horizontal setup, the rods were oriented horizontally and parallel to the surface of the water

at the center of the cooler, but a few centimeters below the water surface. The rod spacing for the vertically- and horizontally-oriented rods are compared in Table 3 where r_c values derived from both orientations revealed significant differences in the air-free ice relative to agar-stabilized water using both ILS and ICPC models. Interestingly, consistent trends in r_c values were obtained for both vertical and horizontal orientations where both Ta and Tb had larger r_c values than in agar-stabilized water for ILS, even approaching the 0.5 mm expected shift based on the 8% ice expansion. However, for ICPC, the difference between r_{c_i} and r_{c_w} in Ta and Tb exhibited inconsistent results and the r_c values were more similar to values of r_c in water. Overall, the r_c estimates for both thermistors, Ta and Tb did not seem to be substantially affected by the rod orientation in ice. If the ice expands in all directions from the center, the resulting impact on r_c values would seem to be highly variable depending on position relative to the center, rather than on orientation. More detailed research is needed to fully address the ice expansion issue and to identify any optimal positioning scenarios for the rods.

4.5 Thermal Property Estimation in Water and Ice

Table 4 presents the statistical analysis of THPP-derived thermal properties (λ , C_v and κ), including their average (Avg.), standard deviation (Std.), RMSE, TE, and RE using ILS and ICPC models with the r_c calibrated in air-free ice (r_{c_i}), the r_c calibrated agar-stabilized water (r_{c_w}), and the measured physical spacing (r_{phy}). As mentioned, the thermal properties of ice and water were derived using the individually calibrated r_c for each thermistor-rod. In Table 4, we present the combined results using both thermistor-rods to show the approximate error range of thermal property estimations by THPP. By inputting r_{phy} into ILS and ICPC models for thermal property calculation, the results are derived with

no spacing calibration. The minimum TE values of thermal properties determined in both agar-stabilized water and air-free ice are highlighted in bold text, suggesting the most accurate and precise estimation among the 6 approaches. With one exception, i.e., the C_v estimation using the ILS model, the smallest TE values for λ and κ were exhibited by the ICPC model fitting with either r_{c_i} or r_{phy} in Table 4.

The ICPC model reduced the TE for all thermal properties especially for λ in both air-free ice and agar-stabilized water. The r_c calibration in different media did not affect λ estimation using the ILS model, resulting in the same average, standard deviation, RMSE, TE, and RE of λ in air-free ice and agar-stabilized water. The effect of r_c on λ estimation has been thoroughly discussed previously (Noborio et al., 1996; Kluitenberg et al., 2010). We found that the ICPC model in both air-free ice and agar-stabilized water exhibited slight changes in λ among the three different spacing values, showing reduced TE and RE compared to ILS model results. Regardless of the heat transfer model, applying the uncalibrated r_{phy} and the r_c calibrated in media with different thermal properties than the test media resulted in larger errors when estimating C_v . For example, estimating C_v of agar-stabilized water with r_{c_i} using both ILS and ICPC models resulted in RE's of 10% and 5%, respectively, and using r_{phy} with both models gave RE's of 2.3 and 1.4%, respectively. These RE values were substantially greater than the RE values for C_v of agar-stabilized water using r_{c_w} , which were 0.5% and 0.6%, respectively. Both models provided equally small TE and RE for C_v estimations in both air-free ice and agar-stabilized water as long as the calibration was done in the test media. This suggests that the in-situ r_c calibration using the field C_v could improve thermal property estimation compared to using the r_c calibration performed in the laboratory with agar-stabilized water due to the discrepancy

in thermal properties between bulk soil and water. In other words, when the material's C_v is substantially different from the C_v of the calibration material (e.g., wet soil vs. dry soil), then the thermal property estimation can be biased by using a derived r_c value from a reference material that has dis-similar thermal properties. We note that the C_v of air-free ice is closer to that of wet soil than the C_v of water, a potential advantage of using ice as reference material. The κ results were obtained using the computed κ from fitted λ and C_v values and the ICPC model with r_{c_i} and r_{phy} exhibited the minimum RE in air-free ice and agar-stabilized water, respectively.

The temperature-dependent reference thermal property (λ , κ , and C_v) functions of ice and water were plotted in Fig. 4 to compare how well the ICPC model performed using the calibrated r_c values in air-free ice (r_{c_i}) to fit or compute λ , C_v , and κ for both ice and water. The standard deviation around the mean of each thermal property is presented by error bars. These thermal properties derived using the ICPC model with calibrated r_{c_i} in both agar-stabilized water and air-free ice show good agreement with the reference empirical functions from Table 2, in a range between 0.60 and 2.4 W m⁻¹ °C⁻¹ for λ , 1.79 and 4.18 MJ m⁻³ °C⁻¹ for C_v , and 0.14 and 1.4 mm² s⁻¹ for κ .

5. CONCLUSIONS

Using air-free ice as a standard for HPP rod spacing calibration was demonstrated and compared to the traditional calibration medium of agar-stabilized water. Creating air-free ice is non-trivial and requires three main components: 1) a freezer capable of maintaining temperatures below -10°C and enclosing a medium-sized cooler, 2) a well-insulated cooler to ensure top-down freezing (the rotationally-molded type is recommended), and 3) the water depth in the cooler should be 3–4 times deeper than the

THPP rod length to ensure air-free ice surrounds the HPP rods. Depending on the volume of water used, the freezing of air-free ice may require substantially more time than making agar-stabilized water. It was a concern that ice expansion may alter the physical probe spacing and apparent significant differences were determined in r_c between ice and water. The resulting thermal property determination in ice, however, was closer to the expected thermal properties of ice or more accurately determined than those of water. In addition to providing another probe spacing calibration standard with substantially different thermal properties compared to agar-stabilized water, air-free ice is also useful for verifying the thermal property estimation of HPPs in general. The ICPC model significantly reduced RE for thermal property estimations in both air-free ice and agar-stabilized water compared with the ILS model. Since the ICPC model accounts for the finite diameter and C_v of the HPP rods, the calibrated r_c is closer to the r_{phy} with less dependence on the calibration medium C_v compared to the ILS model. However, simply applying the r_{phy} in the ICPC model without spacing calibration will likely yield non-negligible errors for thermal property determination. Based on our calibration and thermal property analysis in ice and water presented here, we find the application of the ICPC model in both liquid and solid reference media to be a potential benefit for HPP applications in the future.

REFERENCES

- Bilskie, J.R., R. Horton, and K.L. Bristow. 1998. Test of a dual-probe heat-pulse method for determining thermal properties of porous materials¹. *Soil science* 163(5): 346–355.
https://journals.lww.com/soilsci/Abstract/1998/05000/TEST__OF_A_DUAL_PROBE_HEAT_PULSE_METHOD_FOR.2.aspx (accessed 28 July 2020).
- Bristow, K.L., G.J. Kluitenberg, and R. Horton. 1994a. Measurement of Soil Thermal Properties with a Dual-Probe Heat-Pulse Technique. *Soil Sci. Soc. Am. J.* 58(5): 1288–1294. doi: 10.2136/sssaj1994.03615995005800050002x.
- Bristow, K., R. White, and G. J. Kluitenberg. 1994b. Comparison of Single and Dual Probes for Measuring Soil Thermal Properties with Transient Heating. *Aust. J. Soil Res. - AUST J SOIL RES* 32. doi: 10.1071/SR9940447.
- Campbell, G.S., C. Calissendorff, J.H. Williams, R.M. Newman, G.J. Kluitenberg, et al. 1991. Probe for Measuring Soil Specific Heat Using A Heat-Pulse Method. *Soil Sci. Soc. Am. J.* 55(1): 291–293. doi: 10.2136/sssaj1991.03615995005500010052x.
- Cobos, D.R., and J.M. Baker. 2003. In Situ Measurement of Soil Heat Flux with the Gradient Method. *Vadose Zo. J.* 2(4): 589–594. doi: 10.2113/2.4.589.
- Ham, J.M., and E.J. Benson. 2004. On the Construction and Calibration of Dual-Probe Heat Capacity Sensors. *Soil Sci. Soc. Am. J.* 68(4): 1185–1190. doi: 10.2136/sssaj2004.1185.
- Haynes, W.M. 2016. *CRC Handbook of Chemistry and Physics*. CRC Press.
- He, H., M.F. Dyck, R. Horton, T. Ren, K.L. Bristow, et al. 2018. Development and Application of the Heat Pulse Method for Soil Physical Measurements. *Rev. Geophys.*

- 56(4): 567–620. doi: 10.1029/2017RG000584.
- He, H., M. Dyck, J. Wang, and J. Lv. 2015. Evaluation of TDR for Quantifying Heat-Pulse-Method-Induced Ice Melting in Frozen Soils. *Soil Sci. Soc. Am. J.* 79(5): 1275–1288. doi: 10.2136/sssaj2014.12.0499.
- Heitman, J.L., R. Horton, T.J. Sauer, and T.M. DeSutter. 2008. Sensible Heat Observations Reveal Soil-Water Evaporation Dynamics. *J. Hydrometeorol.* 9(1): 165–171. doi: 10.1175/2007JHM963.1.
- Hopmans, J.W., J. Šimunek, and K.L. Bristow. 2002. Indirect estimation of soil thermal properties and water flux using heat pulse probe measurements: Geometry and dispersion effects. *Water Resour. Res.* 38(1): 7-1-7–14. doi: 10.1029/2000wr000071.
- Kamai, T., G.J. Kluitenberg, and J.W. Hopmans. 2015. A Dual-Probe Heat-Pulse Sensor with Rigid Probes for Improved Soil Water Content Measurement. *Soil Sci. Soc. Am. J.* 79(4): 1059–1072. doi: 10.2136/sssaj2015.01.0025.
- Kamai, T., A. Tuli, G.J. Kluitenberg, and J.W. Hopmans. 2008. Soil water flux density measurements near 1 cm d⁻¹ using an improved heat pulse probe design . *Water Resour. Res.* 44(4). doi: 10.1029/2008wr007036.
- Kluitenberg, G.J., J.M. Ham, and K.L.L. Bristow. 1993. Error Analysis of the Heat Pulse Method for Measuring Soil Volumetric Heat Capacity. *Soil Sci. Soc. Am. J.* 57(6): 1444–1451. doi: 10.2136/sssaj1993.03615995005700060008x.
- Kluitenberg, G.J., T. Kamai, J.A. Vrugt, and J.W. Hopmans. 2010. Effect of Probe Deflection on Dual-Probe Heat-Pulse Thermal Conductivity Measurements. *Soil Sci. Soc. Am. J.* 74(5): 1537–1540. doi: 10.2136/sssaj2010.0016n.
- Knight, J.H., G.J. Kluitenberg, T. Kamai, and J.W. Hopmans. 2012. Semianalytical

- Solution for Dual-Probe Heat-Pulse Applications that Accounts for Probe Radius and Heat Capacity. *Vadose Zo. J.* 11(2). doi: 10.2136/vzj2011.0112.
- Lipp, G., C. Körber, S. English, U. Hartmann, and G. Rau. 1987. Investigation of the behavior of dissolved gases during freezing. *Cryobiology* 24(6): 489–503. doi: 10.1016/0011-2240(87)90053-8.
- Mori, Y., J.W. Hopmans, A.P. Mortensen, and G.J. Kluitenberg. 2003. Multi-Functional Heat Pulse Probe for the Simultaneous Measurement of Soil Water Content, Solute Concentration, and Heat Transport Parameters. *Vadose Zo. J.* 2(4): 561–571. doi: 10.2136/vzj2003.5610.
- Mori, Y., J.W. Hopmans, A.P. Mortensen, and G.J. Kluitenberg. 2005. Estimation of Vadose Zone Water Flux from Multi-Functional Heat Pulse Probe Measurements. *Soil Sci. Soc. Am. J.* 69(3): 599–606. doi: 10.2136/sssaj2004.0174.
- Mortensen, A.P., J.W. Hopmans, Y. Mori, and J. Šimůnek. 2006. Multi-functional heat pulse probe measurements of coupled vadose zone flow and transport. *Adv. Water Resour.* 29(2): 250–267. doi: 10.1016/j.advwatres.2005.03.017.
- Noborio, K., K.J. McInnes, and J.L. Heilman. 1996. Measurements of soil water content, heat capacity, and thermal conductivity with a single TDR probe. *Soil Sci.* 161(1): 22–28. doi: 10.1097/00010694-199601000-00004.
- Ochsner, T.E., R. Horton, and T. Ren. 2003. Use of the Dual-Probe Heat-Pulse Technique to Monitor Soil Water Content in the Vadose Zone. *Vadose Zo. J.* 2(4): 572–579. doi: 10.2136/vzj2003.5720.
- Ochsner, T.E., T.J. Sauer, and R. Horton. 2007. Soil heat storage measurements in energy balance studies. *Agron. J.* 99(1): 311–319. doi: 10.2134/agronj2005.0103S.

- Peng, W., Y. Lu, X. Xie, T. Ren, and R. Horton. 2019. An Improved Thermo-TDR Technique for Monitoring Soil Thermal Properties, Water Content, Bulk Density, and Porosity. *Vadose Zo. J.* 18(1): 1–9. doi: 10.2136/vzj2019.03.0026.
- Ren, T., G.J. Kluitenberg, and R. Horton. 2000. Determining Soil Water Flux and Pore Water Velocity by a Heat Pulse Technique. *Soil Sci. Soc. Am. J.* 64(2): 552–560. doi: 10.2136/sssaj2000.642552x.
- Ren, T., K. Noborio, and R. Horton. 1999. Measuring Soil Water Content, Electrical Conductivity, and Thermal Properties with a Thermo-Time Domain Reflectometry Probe. *Soil Sci. Soc. Am. J.* 63(3): 450–457. doi: 10.2136/sssaj1999.03615995006300030005x.
- Ren, T., T.E. Ochsner, and R. Horton. 2003. Development of Thermo-Time Domain Reflectometry for Vadose Zone Measurements. *Vadose Zo. J.* 2(4): 544–551. doi: 10.2136/vzj2003.5440.
- Sheng, W., R. Zhou, M. Sadeghi, E. Babaeian, D.A. Robinson, et al. 2017. A TDR Array Probe for Monitoring Near-Surface Soil Moisture Distribution. *Vadose Zo. J.* 16(4): 1–8. doi: 10.2136/vzj2016.11.0112.
- Tarara, J.M., and J.M. Ham. 1997. Measuring soil water content in the laboratory and field with dual-probe heat-capacity sensors. *Agron. J.* 89(4): 535–542. doi: 10.2134/agronj1997.00021962008900040001x.
- De Vries, D.A. 1963. Thermal properties of soils. In: Van Wijk, W.R., editor, *Physics of Plant Environment*. North-Holland Publishing Company, Amsterdam. p. 210–235
- Yang, C., M. Sakai, and S.B. Jones. 2013. Inverse method for simultaneous determination of soil water flux density and thermal properties with a penta-needle heat pulse probe.

Water Resour. Res. 49(9): 5851–5864. doi: 10.1002/wrcr.20459.

Zhang, M., Z. Che, J. Chen, H. Zhao, L. Yang, et al. 2011. Experimental determination of thermal conductivity of water-agar gel at different concentrations and temperatures.

J. Chem. Eng. Data 56(4): 859–864. doi: 10.1021/je100570h.

Table 1. Comparison of rod dimensions and volumetric heat capacities of the HPP components.

HPP	r_{phy}	Stainless steel rod			Volumetric heat capacity			
		Length	d_o	d_e	C_{SS}	C_E	C_o	
		mm			— MJ m ⁻³ °C ⁻¹ —			
THPP	T_a	6.87	50	2.40	0.61	4.0	2.03	3.87
	T_b	“	“	“	“	“	“	“
DHPP _C †	6	28	0.819					
DHPP _H ‡	5.78	28						
PHPP _Y §	6.5	28	1.27††					
			2.10‡‡					
C-DHPP _K ¶	6.06	28	1.27	0.838	4.0	2.03	3.14	
R-DHPP _K ¶	7.14	35	2.38	0.959	4.0	2.03	3.68	
	7.13	40	“	“	“	“	“	
	7.14	45	“	“	“	“	“	
THPP _P #	10	70	2.38††	0.96††	4.0	2.03	3.68	
			2‡‡	1.5‡‡				

†Campbell et al. (1991); ‡Ham and Benson (2004); §Yang et al. (2013); ¶Each r_{phy} is the average of three needles constructed by Kamai et al. (2015); #Peng et al. (2019); ††Temperature-sensing-rod; ‡‡Heater-rod.

Table 2. Thermal properties of ice and water as functions of temperature using polynomial equations (all $r^2 = 0.99$) generated by curve fitting software (TableCurve 2D, Systat Software Inc.) and coefficients fitted to 10°C increment data presented by Haynes (2016).

Water (0 to 100°C)		Ice (-50 to 0°C)	
Specific heat, c ($\text{J g}^{-1} \text{ } ^\circ\text{C}^{-1}$)			
$\ln y = a + bT + cT^2 + dT^3 + eT^4 + fT^5$		$y = a + bT + cT^2$	
a	1.4397	a	2.0982
b	-7.6917×10^{-4}	b	7.4607×10^{-3}
c	2.3230×10^{-5}	c	1.7857×10^{-6}
d	-3.4110×10^{-7}		
e	2.6325×10^{-9}		
f	-7.8426×10^{-12}		
Volumetric heat capacity, C_v ($\text{MJ m}^{-3} \text{ } ^\circ\text{C}^{-1}$)			
$y = a + bT^{1.5} + cT^{0.5}$		$y = a + bT + cT^2$	
a	4.2194	a	1.9235
b	-1.0600×10^{-4}	b	6.5317×10^{-3}
c	-7.2627×10^{-3}	c	1.5232×10^{-7}
Thermal conductivity, λ ($\text{W m}^{-1} \text{ } ^\circ\text{C}^{-1}$)			
$y = a + bT + cT^{1.5}$		$y^2 = a + bT + cT^2$	
a	0.55546	a	4.6622
b	2.8702×10^{-3}	b	-4.2206×10^{-2}
c	-1.6512×10^{-4}	c	3.5874×10^{-4}
Thermal diffusivity, κ ($\text{mm}^2 \text{ s}^{-1}$)			
$y = a + bT + cT^{1.5}$		$y = a + bT + cT^2$	
a	0.13183	a	1.1231
b	7.2856×10^{-4}	b	-8.7149×10^{-3}
c	-3.7120×10^{-5}	c	6.9886×10^{-5}

Table 3. Physical rod spacing (r_{phy}) and the average calibrated spacing (r_c) and standard deviation (Std.) are presented for air-free ice and agar-stabilized water. The difference between r_c of ice and water ($r_{c_i} - r_{c_w}$) is also presented. Data were analyzed using the infinite line source- (ILS) and identical-cylinders perfect-conductors- (ICPC) models with various heat pulse probe (HPP) configurations. See Table 1 for sensor references.

Air-free ice (-21°C)							
Probe Orientation	Model		r_{phy}	r_c	Std.	$r_{c_i} - r_{c_w}$	
mm							
Vertical	THPP	ILS	T_a	6.87	7.37	0.001	0.45
		“	T_b	6.94	7.15	0	0.23
		ICPC	T_a	6.87	7.01	0.001	0.05
		“	T_b	6.94	6.79	0	-0.17
Horizontal	THPP	ILS	T_a	6.87	7.34	0.003	0.42
		“	T_b	6.94	7.13	0.003	0.21
		ICPC	T_a	6.87	7	0.003	0.04
		“	T_b	6.94	6.79	0.003	-0.17
Agar-stabilized water (21°C)							
Probe Orientation	Model		r_{phy}	r_c	Std.		
mm							
Vertical	THPP	ILS	T_a	6.87	6.92	0.015	
		“	T_b	6.94	6.92	0.018	
		ICPC	T_a	6.87	6.96	0.015	
		“	T_b	6.94	6.96	0.018	
DHPP _C	ILS		6	5.88			
DHPP _H	“		5.78	5.67	<0.02		
PHPP _Y	“		6.5	6.26	0.003		
C-DHPP _K †	ILS		6.06	6.11	0.023		
	ICPC		“	6.14	0.022		
R-DHPP _K †	ILS		7.14	7.03	0.068		
	ICPC		“	7.08	0.068		
	ILS		7.13	7	0.06		
	ICPC		“	7.06	0.059		
	ILS		7.14	7.05	0.095		
	ICPC		“	7.1	0.094		

† Average and standard deviation for r_{phy} and r_c are average values from three needles with the same two-needle configuration as Kamai et al. (2015).

Table 4. Computed average, standard deviation, RMSE, TE, and RE to the reference thermal properties of ice and water with different r_c using the ILS and ICPC model. Bold numbers represent the minimal TE of each thermal property estimates.

		Thermal conductivity, λ									
		Water (21°C) Reference: $\lambda = 0.600$					Ice (-21°C) Reference: $\lambda = 2.39$				
		Avg.	Std.	RMSE	TE	RE	Avg.	Std.	RMSE	TE	RE
		—— $\text{W m}^{-1} \text{ }^\circ\text{C}^{-1}$ ——				%	—— $\text{W m}^{-1} \text{ }^\circ\text{C}^{-1}$ ——				%
ILS	r_{c_i}	0.670	0.005	0.071	0.071	12	2.306	0.029	0.088	0.093	3.9
	r_{c_w}	0.670	0.005	0.071	0.071	12	2.306	0.029	0.088	0.093	3.9
	r_{phy}	0.670	0.005	0.071	0.071	12	2.306	0.029	0.088	0.093	3.9
ICPC	r_{c_i}	0.619	0.005	0.021	0.022	3.6	2.414	0.023	0.039	0.045	1.9
	r_{c_w}	0.622	0.004	0.023	0.023	3.8	2.425	0.039	0.061	0.073	3.0
	r_{phy}	0.620	0.004	0.020	0.021	3.5	2.416	0.044	0.061	0.075	3.2
		Volumetric heat capacity, C_v									
		Water (21°C) Reference: $C_v = 4.18$					Ice (-21°C) Reference: $C_v = 1.79$				
		Avg.	Std.	RMSE	TE	RE	Avg.	Std.	RMSE	TE	RE
		—— $\text{MJ m}^{-3} \text{ }^\circ\text{C}^{-1}$ ——				%	—— $\text{MJ m}^{-3} \text{ }^\circ\text{C}^{-1}$ ——				%
ILS	r_{c_i}	3.797	0.098	0.396	0.408	10	1.788	0.000	0.001	0.001	0.0
	r_{c_w}	4.176	0.015	0.017	0.022	0.5	1.967	0.048	0.189	0.195	11
	r_{phy}	4.248	0.038	0.089	0.097	2.3	1.976	0.065	0.204	0.215	12
ICPC	r_{c_i}	4.261	0.130	0.174	0.217	5.2	1.787	0.000	0.001	0.001	0.0
	r_{c_w}	4.177	0.017	0.019	0.025	0.6	1.753	0.052	0.072	0.089	5.0
	r_{phy}	4.192	0.033	0.049	0.059	1.4	1.785	0.071	0.086	0.111	6.2
		Thermal diffusivity, $\kappa (= \lambda/C_v)$									
		Water (21°C) Reference: $\kappa = 0.144$					Ice (-21°C) Reference: $\kappa = 1.34$				
		Avg.	Std.	RMSE	TE	RE	Avg.	Std.	RMSE	TE	RE
		—— $\text{mm}^2 \text{ s}^{-1}$ ——				%	—— $\text{mm}^2 \text{ s}^{-1}$ ——				%
ILS	r_{c_i}	0.177	0.004	0.034	0.034	24	1.290	0.016	0.049	0.052	3.9
	r_{c_w}	0.161	0.001	0.017	0.017	12	1.174	0.044	0.170	0.175	13
	r_{phy}	0.160	0.001	0.016	0.017	12	1.170	0.053	0.177	0.185	14
ICPC	r_{c_i}	0.146	0.005	0.007	0.009	6.0	1.351	0.013	0.022	0.026	1.9
	r_{c_w}	0.149	0.000	0.005	0.005	3.8	1.386	0.064	0.093	0.113	8.4
	r_{phy}	0.146	0.002	0.003	0.003	2.3	1.359	0.078	0.098	0.125	9.4

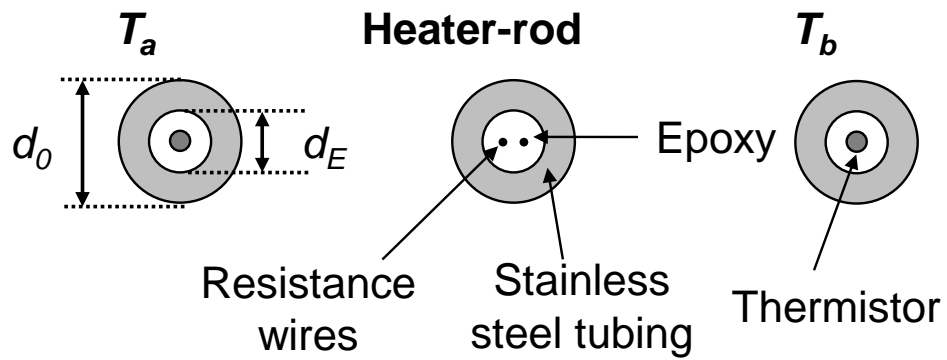


Fig. 1. The cross-section of a Tri-needle Heat Pulse Probe (THPP) with two thermistor-rods (T_a and T_b) and one heater-rod.

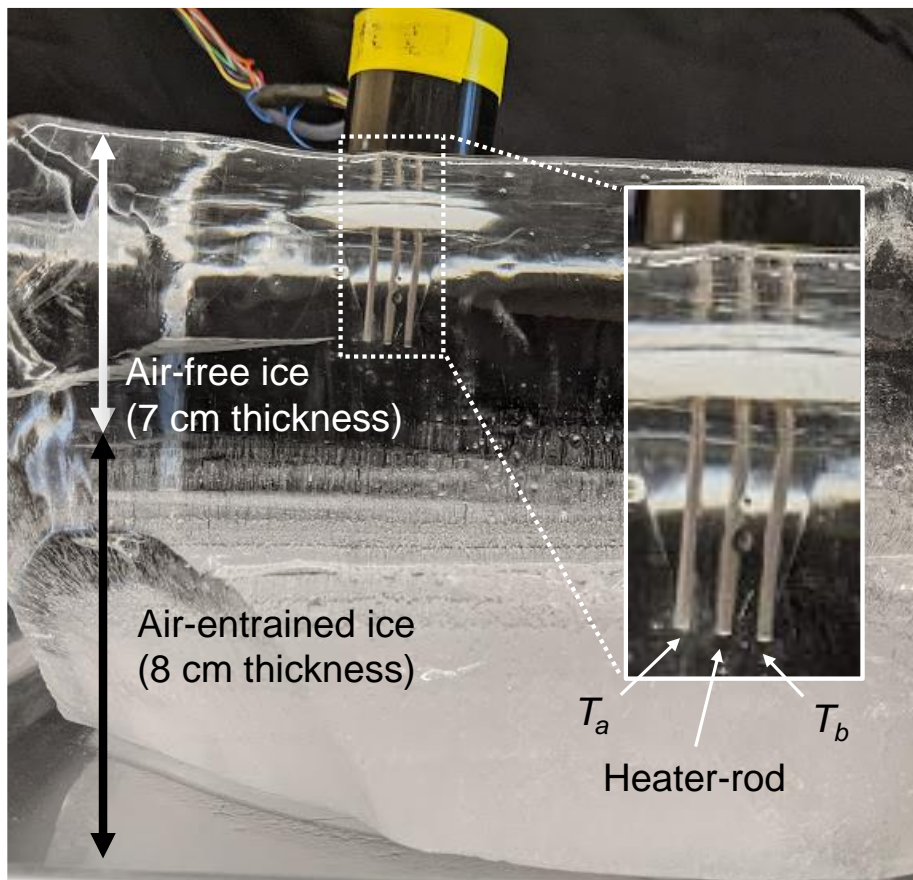


Fig. 2. Ice block showing air-free and air-entrained sections with THPP rods (the heater-rod and two thermistor-rods, T_a and T_b) in the air-free portion.

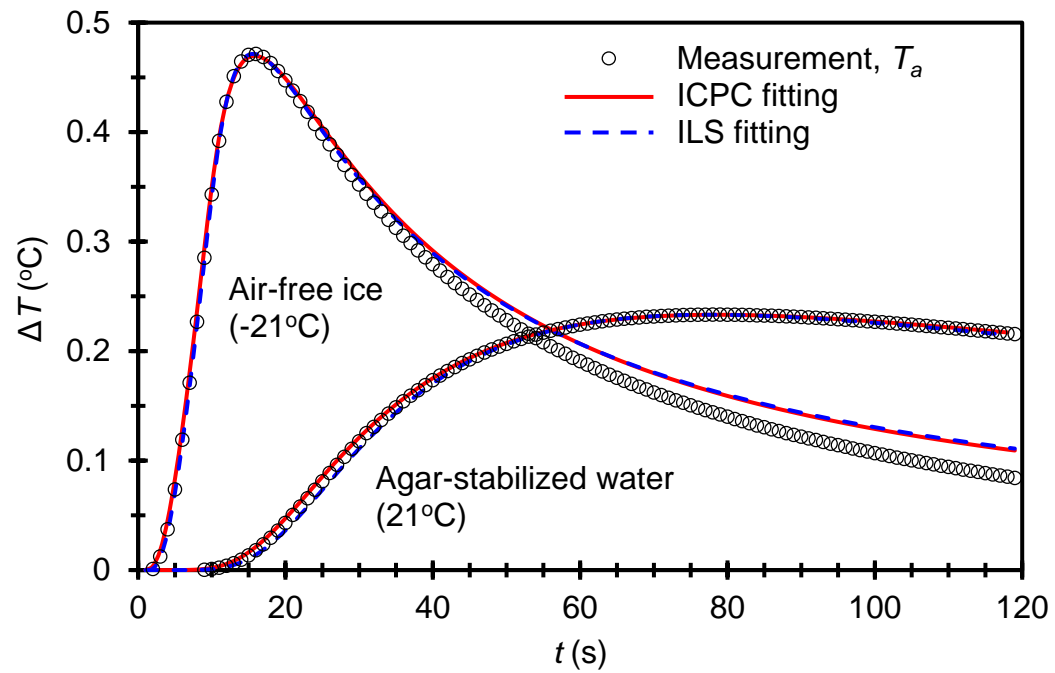


Fig. 3. Comparison of the measured temperature rise at one thermistor-rod, T_a , and the fitted temperature rise as a function of time in air-free ice (-21°C) and agar-stabilized water (21°C).

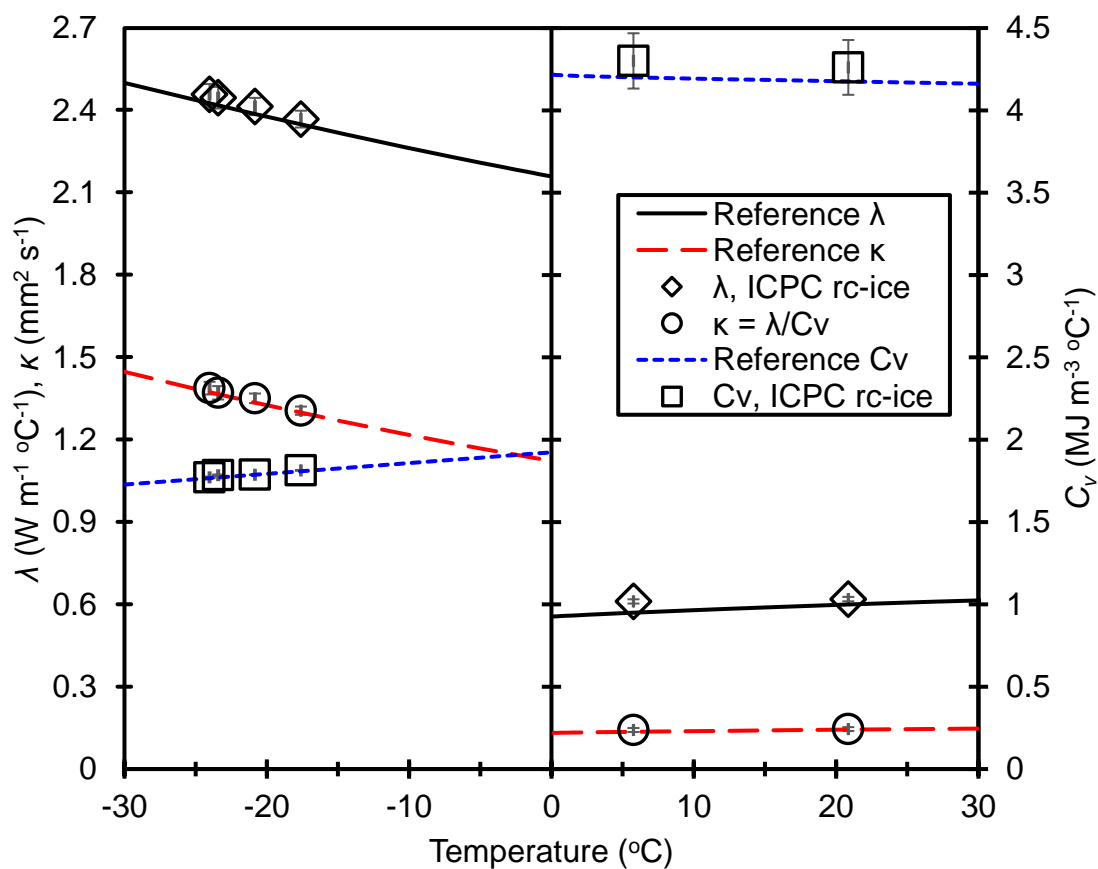


Fig. 4. Thermal-conductivity (λ) and volumetric heat capacity (C_v) from THPP estimates with the calibrated r_c in air-free ice (-21°C) using the ICPC model, and resulting computed thermal diffusivity ($\kappa=\lambda/C_v$) (symbols). Lines illustrate the modeled reference values presented as functions of temperature.

CHAPTER III

THERMAL PROPERTY STANDARDS USING GRANULAR MEDIA WITH AIR-
PLUVIATION AND HEAT PULSE PROBE MEASUREMENTS

ABSTRACT

The fundamental thermal properties of soils and granular media include volumetric heat capacity (C_v), thermal conductivity (λ) and thermal diffusivity (κ), which play key roles in the transfer and maintenance of heat in the environment. Thermal properties are highly dependent upon the granular medium volumetric water content (θ_w), and thus thermal property functions are critical for modeling soil and land surface thermal processes. However, few available standard granular materials provide a source of ‘known’ thermal property values, perhaps foremost because of the difficulty in achieving a repeatable bulk density (ρ_b) value in addition to other packing and wetting complications. Our objectives were to identify and evaluate a range of readily available granular media that could be used to calibrate and validate thermal property measurements (i.e., Heat Pulse Probes, HPP) and to establish packing and wetting/drainage methods that result in repeatable granular media conditions for thermal property determinations. We identified and tested a variety of granular media including spherical- (quartz sand, glass beads), angular- (crushed media) and aggregated- materials. Thermal property values were determined under uniform θ_w of oven-dried, saturated conditions and the drained-water content at -5.9 m suction using combined methods of HPP measurements for thermal property estimations and the multiple sieving pluviation (MSP) method, yielding highly repeatable ρ_b in coarse granular media.

Overall, thermal property values ranged from 0.51 to 3.68 MJ m⁻³ K⁻¹ for C_v , 0.13 to 3.73 W m⁻¹ K⁻¹ for λ and 0.17 to 1.5 mm² s⁻¹ for κ . Optimized parameters were presented for selected $C_v(\theta_w)$ and $\lambda(\theta_w)$ thermal property models. We demonstrated that with the MSP method, it was possible to achieve highly repeatable ρ_b values and thermal property values for several commercially available granular materials. We recommend this approach as a standard calibration method based on 1) repeatable granular media packing and 2) standardized thermal property values for coarse granular media at targeted uniform θ_w distributions.

1. INTRODUCTION

Thermal properties, including volumetric heat capacity (C_v), thermal conductivity (λ), and thermal diffusivity (κ), are fundamental physical parameters. These properties are critical for understanding the Earth's energy balance, which affects vadose zone temperature-dependent processes such as microbial activity, redox potential, plant root uptake of water and nutrients, freezing and thawing processes as well as the transport of gases, nutrients and water. Thermal properties in granular media vary with temperature, water content, pressure and mineral type (Farouki, 1981) as well as particle structural characteristics including aggregation, bulk density (ρ_b), particle size distribution and particle shape (Dai et al., 2019). Therefore several thermal property models have been developed to characterize thermal properties by accounting for variable conditions. The mixing models developed by de Vries (1963) consider granular media as a constituent of solid, water, gas and organic matter, and the models are extensively used to characterize both C_v and λ at variable volumetric water contents (θ_w). Although the mixing model describing C_v is relatively straightforward and widely used, models describing λ continue

to be developed to adequately describe the complexity of thermal conductance in three phases (i.e., solid, water and air). Several λ models including the mixing model (Campbell et al., 1994; de Vries, 1963), empirical models (Campbell, 1985; Chung and Horton, 1987), the conceptual model (Lu and Dong, 2015) and the theoretical model (Ghanbarian and Daigle, 2016) are available with limitations for certain soil types and conditions. These models are often compared to thermal property measurements in field soils, while the application of thermal property models to readily available media is limited to quartz sand. The availability of standardized granular materials with well-characterized thermal property values (C_v , λ and κ) and the fitted parameters for available models can improve thermal property sensor calibration and performance and advance the development and validation of heat transfer models and their simulation capabilities.

The Dual-rod Heat Pulse (DHP) technique employed using Heat Pulse Probes (HPPs) is widely employed in science and engineering fields for determining thermal property values (Bilskie et al., 1998; Bristow et al., 1994) and a variety of surrogate properties and processes such as water flux (Hopmans et al., 2002; Knight et al., 2012; Yang et al., 2013), subsurface evaporation rate (Heitman et al., 2008), heat flux (Cobos and Baker, 2003) and heat storage (Ochsner et al., 2007). The HPP consists of a line source heater rod and at least one parallel temperature sensing rod. The measured and subsequently modeled temporal temperature rise generally yields all three available thermal property values via model fitting (i.e., C_v , κ and λ). However, accuracy relies heavily on the determination of the center-to-center spacing, r_c , between the temperature sensing rod(s) and the adjacent heater rod.

A widely used conventional model employed in HPPs considers the heater rod as

an infinite line source (ILS) that outputs instantaneous heat (Campbell et al., 1991) or creates heat during a finite time interval (Bristow et al., 1994). This ILS model has been used as a standard method to measure thermal conductivity (ASTM International. Subcommittee D18. 12 on Rock Mechanic, 2008). However, the ILS model yields biased thermal property determination associated with the finite size and contrasting thermal properties of the heater- and temperature-sensing- rods (Guaraglia and Pousa, 1999; Hopmans et al., 2002). Additionally, recent designs of the HPP include thickened stainless-steel rods to minimize rod deflections, resulting in reduced thermal property value errors associated with rod spacing errors. Therefore, Knight et al. (2012) developed a model that includes the physical dimensions and the heat capacity of rod materials including stainless steel and filling epoxy. This semi-analytical model is called the “Identical Cylindrical Perfect Conductors (ICPC)” model and provides better estimations of thermal property values compared to those estimated by the ILS model for agar-stabilized water and air-free ice (Naruke et al., 2021) as well as for selected soil materials (i.e., sand and loam) (Peng et al., 2021) with known thermal properties.

Despite the wide application and development of HPPs, thermal property standards and measurement protocols using globally-available granular media have not been established. In-situ HPP calibration is traditionally conducted in agar-stabilized water, while Naruke et al. (2021) established the calibration protocol using air-free ice to provide additional standard properties. Various studies (Liu et al., 2013; Zhang et al., 2020) also explored on-site HPP calibration in the field. However, there is a gap between in-situ calibration in non-porous media and on-site calibration in heterogeneous field soils, and targeting commercially available granular media as standard calibration options can

advance the development of thermal property sensors. Most manufacturers of granular media provide a single value of λ or sometimes include a range of λ values across a θ_w range from dry to wet, however, a reliably measured suite including all three fundamental thermal properties (C_v , λ and κ) is to our knowledge unavailable. A major challenge of developing a standardized in-situ method using granular media has included establishing and maintaining a repeatably- and accurately-packed material at different θ_w conditions. Because ρ_b variation directly impacts solid- and pore space- configuration, it consequently impacts thermal properties. Suggesting a variety of readily-available granular media exhibiting different mineral types (e.g., quartz and aluminum oxide), particle shapes (e.g., spherical and angular) and particle structures (e.g., aggregated and non-aggregated), may enable the advancement of our understanding of heat transport mechanism through different constituent phases (i.e., solid, water and air).

Traditionally, pluviation, tamping and vibration methods under dry- or wet-conditions have been widely used to prepare granular media in laboratory testing and field engineering studies and applications (Shi et al., 2021; Tabaroei et al., 2017). Air-pluviation uses a funnel to channel granular media at maintained velocity from a certain height (ASTM Committee D-18 on Soil and Rock., 2006) and is widely used to provide repeatable ρ_b (Kodicherla et al., 2018; Shi et al., 2021; Tabaroei et al., 2017). The early work by Miura and Toki (1982) first demonstrated air-pluviation using a screen column, called the “Multiple Sieving Pluviation (MSP)” method, allowing particles to scatter randomly while pouring media into a column, preventing particle segregation. Shi et al. (2021) evaluated the homogeneity and microstructure of granular media prepared by air- and water- MSP methods and moist- and dry- tamping methods of coarse calcareous sand and showed that

the air-MSP method provided the highest homogeneity. Both tamping and vibration are often combined with the MSP method, and Yu et al., (2006) demonstrated that properly controlled vibration results in disordered to ordered packing and the highest ρ_b . However, the denser packing using the vibration method for ellipsoidal-shaped particles can alter particle orientation (e.g., horizontal or vertical) and exhibit a wall effect (Gan and Yu, 2020), meaning that the vibration method alters particle contact and the contact between HPP rods and ellipsoidal-shaped particles. Given the theoretical assumptions for heat transport in homogeneously packed granular media, we find the air-MSP method to be a critical standard preparation method for HPP calibration measurements for repeatable thermal property measurements in coarse granular packed media.

Our objectives were to 1) determine the repeatability of coarse granular media packing density using the MSP method, 2) to determine the HPP-based thermal properties of these media using the ICPC model at oven-dried-, saturated- and drained- θ_w conditions, and 3) to determine model parameter values describing θ_w -dependent C_v and λ values of these media based on fitted data.

2. THEORY

2.1 ICPC model

Knight et al. (2012) presented the ICPC model, which is a semi-analytical solution of the temperature rise with time, $\Delta T(t)$ at a known distance from the line-source heater, r_c (m), as the heat propagates through a homogeneous and isotropic medium. The Laplace transform solution of this process is written as:

$$\hat{T}_C(p) = \frac{q' K_0(\mu r_c)}{2\pi\lambda p \left\{ \mu a_0 \left[K_1(\mu a_0) + \left(\frac{\mu a_0 \beta_0}{2} \right) K_0(\mu a_0) \right] \right\}^2} \quad (1)$$

where q' represents the heat input (W m^{-1}), p is the Laplace transform variable (s^{-1}) and $\hat{T}_C(p)$ is the Laplace transform of the temperature arriving at the sensing rod, $T_C(t)$, for the case of continuous heating. Also, $K_n(z)$ is the modified Bessel function of the second kind of order n and argument z , $\mu = \sqrt{p/\kappa}$, a_0 is the radius of the rod (m), $\beta_0 = C_0/C_v$. The weighted average volumetric heat capacity of the rod, C_0 , including stainless steel and epoxy was calculated as:

$$C_0 = C_E \frac{d_E^2}{d_0^2} + C_{SS} \left(1 - \frac{d_E^2}{d_0^2}\right) \quad (2)$$

where C_E and C_{SS} are volumetric heat capacities of rod-epoxy and -stainless-steel and d_E and d_0 are the inner and outer diameters of the stainless-steel rod, respectively. Based on the principle of superposition, the temperature increase from a heating pulse can be calculated as:

$$\Delta T(t) = \begin{cases} \Delta T_C(t) & 0 < t \leq t_0 \\ \Delta T_C(t) - \Delta T_C(t - t_0) & t > t_0 \end{cases} \quad (3)$$

where t is the elapsed time (s) and t_0 is a short duration of heat input (s), which conventionally is 8 s. This solution accounts for a finite rod radius and the finite heat capacity of both heater- and temperature-sensing-rods, including the stainless-steel tubing and the epoxy. The ICPC model becomes identical to the traditional line-heat source (ILS) model (also referred to as Pulsed Infinite Line Source or PILS) developed by Bristow et al. (1994) if the radius of both heater- and temperature-sensing-rod become zero ($a_0 = 0$). The introduction of finite rod radius (a_0) and β_0 accounts for the shift of heat-pulse arrival at the temperature-sensing-rods relative to the ILS model, reducing the bias of thermal property estimation in materials with a varied range of thermal properties.

2.2 Thermal Property Models

2.2.1. Volumetric heat capacity

The volumetric heat capacity of granular materials characterizes the amount of heat stored in a unit volume of media, which is an important characteristic determining the magnitude of annual and diurnal variations in heat storage impacting various processes. Since granular media primarily consists of minerals, water, air, and organic matter, C_v can be estimated from constituent-mass fractions and -specific heat capacities as follows (Campbell, 1985; de Vries, 1963):

$$C_v = \sum \rho_x c_x \theta_x \quad (4)$$

where ρ_x is constituent density (kg m^{-3}), c_x is constituent specific heat capacity ($\text{MJ kg}^{-1} \text{ } ^\circ\text{C}^{-1}$) and θ_x is constituent volume fraction ($\text{m}^3 \text{ m}^{-3}$). The subscript x specifies the mixture constituency where s , w , a , and om refer to solid, water, air, and organic matter, respectively. The solid-phase term may include multiple minerals such as quartz (q) and other minerals (m), and θ_s is the sum of the volume fraction weighted heat capacities of all identified minerals (i.e., $\theta_s = \theta_q + \theta_m$). Equation 4 can be simplified if the air and organic matter terms are ignored due to their small heat capacity and small volume fraction, respectively (Bristow, 1998; Campbell, 1985).

2.2.2 Thermal conductivity

Thermal conductivity is the amount of heat transmitted through a unit area in a unit of time under a unit temperature gradient, which varies with pore structure, temperature, water content, and mineral type in granular materials. Various λ functions of θ_w have been proposed to characterize heat transfer through granular media, as Dong et al. (2015) discussed.

2.2.3. Mixing model

The ‘mixing model’ computes λ of a granular medium as a weighted sum of the thermal conductivities of material constituents (Campbell et al., 1994; de Vries, 1963):

$$\lambda(\theta_w) = \frac{\sum k_x \theta_x \lambda_x}{\sum k_x \theta_x} \quad (5)$$

where again x specifies the mixture constituency and k_x is a constituent weighting factor. The organic matter component in Eq. 5 is normally combined with the solid phase for simplicity (de Vries, 1963), and if that is the case, the solid phase term in the equation is a comprehensive term that includes minerals and organic matter (i.e., $s = q + m + om$). The solid phase thermal conductivity term (λ_s) may include multiple minerals, e.g., quartz, mica, and others, which may require additional λ and k inputs for mixing models of C_v (Eq. 4) and λ (Eq. 5). The weighting factor, k_x , can be calculated as:

$$k_x = \frac{1}{3} \left[\frac{2}{1+g_a(\lambda_x/\lambda_f-1)} + \frac{1}{1+g_c(\lambda_x/\lambda_f-1)} \right] \quad (6)$$

where g_a and g_c are shape factors, and λ_f is fluid thermal conductivity. Shape factors, g_a and g_c can be expressed as $g_a = 0.088$ for mineral sand (Bittelli et al., 2015) and $g_c = 1 - 2 g_a$, respectively. The thermal conductivity of air (λ_a) is the sum of the conductivity of dry air ($\lambda_{da} = 0.025 \text{ W m}^{-1} \text{ }^\circ\text{C}^{-1}$, de Vries (1963)) and a vapor component associated with latent heat transfer. Campbell et al. (1994) introduced λ_f and an empirical function of water content, f_w , to simplify the k_x calculation in each constituent:

$$\lambda_f = \lambda_a + f_w(\lambda_w - \lambda_a) \quad (7)$$

$$f_w = \frac{1}{1+(\theta_w/\theta_0)^{-q}} \quad (8)$$

where θ_0 and q are material properties that affect the slope of the λ function, especially during the transition from the air- to the water-dominated stage. Bittelli et al. (2015)

established linear regression models, $\theta_0 = 0.33\theta_c + 0.078$ and $q = 7.25\theta_c + 2.52$, both of which are highly related to the clay content (θ_c). In this study, we assumed $\theta_c = 0$ because our testing media were coarse-textured, therefore both parameters were constants with $\theta_0 = 0.078$ and $q = 2.52$, respectively.

2.2.4. Campbell (1985) model

The following empirical $\lambda(\theta_w)$ model was developed by Campbell (1985):

$$\lambda(\theta_w) = A + B\theta_w - (A - D) \exp[-(C\theta_w)^E] \quad (9)$$

where A , B , C , D and E are coefficients that can be determined by fitting Eq. 9 to the measured λ as a function of θ_w or computed using the volume fraction constituents such as solid (s), quartz (q), other mineral (m) and clay (c) as follows.

$$A = \frac{0.57 + 1.73\theta_q + 0.93\theta_m}{1 - 0.74\theta_q - 0.49\theta_m} - 2.8\theta_s(1 - \theta_s), \quad B = 2.8\theta_s, \\ C = 1 + 2.6\theta_c^{-0.5}, \quad D = 0.03 + 0.7\theta_s^2, \quad E = 4 \quad (10)$$

The λ value at saturation (θ_{sat}) can be calculated as $\lambda(\theta_{\text{sat}}) = A + B\theta_{\text{sat}}$, and we determined the A and B values by fitting Eq. 10 to λ measurements. The coefficient C determines how the curve rapidly increases in the lower range of θ_w . Although our coarse granular media did not include clay, $C = 1$ led to a linear λ function of θ_w with no transition point. Therefore, we set $C = 83$, representing a very small clay content, $\theta_c = 0.001$. The D value represents the λ value when $\theta_w = 0$, therefore and D was computed as an average of oven-dry λ measurements.

2.2.5. Chung and Horton (1987) model

An empirical model developed by Chung and Horton (1987) is described as

$$\lambda(\theta_w) = b_1 + b_2\theta_w + b_3\theta_w^{0.5} \quad (11)$$

where b_1 , b_2 and b_3 are empirical parameters determined for specific soils. The parameter,

b_1 refers to the oven-dry λ (λ_{dry}) when $\theta_w = 0$. Chung and Horton (1987) reported parameters b_1 , b_2 and b_3 for three soil types (i.e., sand, silt and clay).

2.2.6. Lu and Dong (2015) model

Lu and Dong (2015) developed a $\lambda(\theta_w)$ model similar to the sigmoidal function of the water retention curve developed by van Genuchten (1980), the retention curve being the relationship between θ_w and the matric potential of the media. The Lu and Dong (2015) model included an onset of the thermal conductivity function θ_{wf} and a fluid network connectivity parameter, m .

$$\frac{\lambda(\theta_w) - \lambda_{dry}}{\lambda_{sat} - \lambda_{dry}} = 1 - \left[1 + \left(\frac{\theta_w}{\theta_{wf}} \right)^m \right]^{1/m-1} \quad (12)$$

2.2.7. Ghanbarian and Daigle (2016) model

Ghanbarian and Daigle (2016) developed a theoretical λ model using the percolation-based effective-medium approximation:

$$(\theta_{sat} - \theta_w) \frac{\lambda_{dry}^{1/t_s} - \lambda^{1/t_s}}{\lambda_{dry}^{1/t_s} + [(\theta_{sat} - \theta_{wc})/\theta_{wc}] \lambda^{1/t_s}} + \theta_w \frac{\lambda_{sat}^{1/t_s} - \lambda^{1/t_s}}{\lambda_{sat}^{1/t_s} + [(\theta_{sat} - \theta_{wc})/\theta_{wc}] \lambda^{1/t_s}} = 0 \quad (13)$$

where t_s is the scaling factor. The critical water content, θ_{wc} , is the volumetric water content at which the liquid phase first forms a continuous path through the porous medium. Ghanbarian and Daigle, (2016) described the θ_{wc} value as analogous to the parameter θ_{wf} in the Lu and Dong (2015) model. The Ghanbarian and Daigle (2016) model is especially flexible to fit a variety of porous media, especially fine-textured soils, and Sadeghi et al. (2018) suggested various existing models are special cases of Ghanbarian and Daigle (2016). While Eq. 12 is an implicit λ function, Sadeghi et al. (2018) derived an explicit λ form as follows:

$$\lambda(\theta_w) = \left[a_1 + a_2 \theta_w + \text{sgn}(t_s) a_2 \sqrt{b_3 + 2b_1 b_2^{-1} \theta_w + \theta_w^2} \right]^{t_s} \quad (14)$$

$$a_1 = \frac{-\theta_w \lambda_{sat}^{1/t_s} + (\theta_{sat} - \theta_w) \lambda_{dry}^{1/t_s}}{2(\theta_{sat} - \theta_w)}, \quad a_2 = \frac{\lambda_{sat}^{1/t_s} - \lambda_{dry}^{1/t_s}}{2(\theta_{sat} - \theta_w)}$$

$$a_3 = \frac{\left[\theta_w \lambda_{sat}^{1/t_s} - (\theta_{sat} - \theta_w) \lambda_{dry}^{1/t_s} \right]^2 + 4\theta_w (\theta_{sat} - \theta_w) \lambda_{sat}^{1/t_s} \lambda_{dry}^{1/t_s}}{\left(\lambda_{sat}^{1/t_s} - \lambda_{dry}^{1/t_s} \right)^2} \quad (15)$$

where sgn is the sign function (i.e., $\text{sgn}(x > 0) = 1$, $\text{sgn}(x < 0) = -1$).

2.3 Accuracy of Thermal Property Estimations

The accuracy of thermal property estimates in granular media was evaluated using Root Mean Square Error (RMSE), which is often used in thermal properties analysis (He et al., 2017; Lu et al., 2019, 2014; Peng et al., 2019; Tian et al., 2016) written as:

$$\text{RMSE} = \sqrt{\frac{\sum (A_{cal} - A_{ref})^2}{n}} \quad (16)$$

where A is the thermal property with lowercase “*cal*” and “*ref*” representing the calculated values using the listed models (Eqs. 4–15) and the estimated values by fitting the ICPC model (Eqs. 1–3) to HPP temperature rise with time measurements. The parameter n is the number of measurements. The RMSE provides knowledge of how far/close calculated thermal property values (A_{cal}) are from the estimated thermal property values (A_{ref}) based on measurements.

3. MATERIALS AND METHODS

3.1 Heat Pulse Probe Construction

A three-rod Heat Pulse Probe (THPP) was constructed following the description of Naruke et al. (2021). The THPP consisted of three stainless steel rods (316 stainless steel,

McMaster-Carr, Douglasville, GA, USA). Each of the two temperature-sensing-rods, T_a and T_b , contained a single thermistor (10K3MCD1, BetaTherm Corp., Shrewsbury, MA, USA) positioned at the rod's mid-length. The heater rod, positioned between the temperature rods, contained heater wire made from 40-gauge enameled Nichrome resistance wire (Nichrome 80, Pelican Wire Co., Naples, FL, USA) with a constant resistance per wire length ($221.9 \Omega \text{ m}^{-1}$). The heater wire was folded in half to create a loop at the distal end of the rod. The heater- and thermistor- rods were filled with a thermally conductive epoxy (slow cure silver epoxy, Arctic Silver Inc., Visalia, CA, USA).

Error! Reference source not found.a shows a THPP with rods extending from the THPP base, and **Error! Reference source not found.**b shows the cross-section of the THPP. Table 2 describes the stainless-steel rod dimensions, including the physical rod spacing (r_{phy}) between each thermistor-rod and the heater-rod, the length of rods (L) and outer- and inner- diameters of the rods, d_o and d_e , respectively. In **Error! Reference source not found.**a, a 39 mm diameter polycarbonate disk of 10 mm thickness was drilled out to house the two thermistor-rods on either side of the heater-rod with a 7 mm center-to-center spacing between each rod pair. The plastic disk with a relatively small λ was used to avoid non-granular media-related heat transfer between rods, which could result in thermal property errors. A hole with a diameter of 1.5 cm was also drilled on the disk to attach a sintered stainless-steel plate connected to plastic tubing to infuse/withdraw water in the testing media. The heater- and thermistor- rod wires protruding from the bottom of the disk, as well as the tubing connected to the sintered stainless-steel disk, were potted inside of a 40 mm-i.d. ABS pipe using a two-part potting epoxy (50-3100RBK-resin, CAT.150CL13-hardener, Epoxies, Etc., Cranston, RI, USA), where the polycarbonate disk

was previously glued into the upper end of the pipe. The outer wall of the ABS pipe had two grooves machined at the upper end to house O-rings for sealing against a 150 mm long, 57 mm i.d. clear Lexan tube used to contain the granular media. The distance between each thermistor-rod and the tube wall should exceed more than the r_{phy} value (i.e., 7 mm) to prevent the effect of different thermal property interfaces (i.e., granular media and air) (Kluitenberg and Philip, 1999). Our measurement system provided a sufficient distance (i.e., 18 mm) between the thermistor-rod and the wall. The heater wire of the THPP was connected in series with a 1- Ω precision resistor ($\pm 1\%$, 2 W), the voltage across which was measured by a CR6 datalogger (Campbell Scientific, Logan, UT, USA) for heating power calculation. The heating duration was 8 s with an average heating rate of $50.1 \pm 0.32 \text{ W m}^{-1}$. The thermistors were measured directly through the differential channels on the datalogger using the built-in 5-k Ω resistor ($\pm 0.1\%$, 10 ppm $^{\circ}\text{C}^{-1}$) to complete the bridge. Thermistor temperatures were recorded for over 150 (or 270) s, including 30 s prior to firing the heater, and a continuation for 120 (or 240) s to capture the heating peak, especially in dry granular media. Due to the large porosity and small λ of oven-dried pumice, a 30 + 240 s temperature rise with time data collection was needed to capture the temperature rise peak. The average pre-heating temperature for 5 seconds before the heat pulse initiation was used as the initial temperature. The 120 (or 240) s of heating and post-heating temperature data were used to optimize thermal properties using the ICPC model. Measurements were initiated every 20 minutes so the sample's temperature around the THPP could cool back down to near ambient temperature after heating to avoid temperature buildup or artificial thermal gradients. The temperature response and heating rate data were recorded for post-analysis of r_c and thermal properties.

3.2 Granular Materials as Reference Media

Granular materials were selected to provide a wide range of thermal and physical properties as reference standards for HPP calibration and validation. The granular media included (a) spherical granular media: fine sand (C778) (C778 ASTM graded silica sand, US Silica, Ottawa, IL, USA), Wedron sand (Wed) (Wedron silica Co., Wedron, IL), soda-lime glass beads (Sod) (GL0191B4/425-600, Mo-sci Specialty Products, L.L.C., Rolla, MO), (b) angular granular media: coarse angular sand (Ang) (2075, Industrial Quarts, Unimin Corp., Emmett, ID), aluminum oxide (Alu) (BLASTITE, Washington Mills, North Grafton, MA), coal slag (Coa) (BLACK BEAUTY Abrasives EXTRA FINE, Harsco Co., Mechanicsburg, PA), garnet (Gar) (#100/120 Grit, Blastline USA) and (c) aggregated media: Profile (Pro) (Profile Products LLC, Buffalo Grove, IL), pumice (Pum) (1/8" – 1/32" pumice, Scenic Hill Farm, Oregon, WA). Table 1 shows the physical properties of the selected granular materials. For additional details about the granular materials, see the product datasheet of each media (Mo-sci Co., 2020; Profile, 2020; U.S. Silica, 2020; Unimin, 2020; Washington Mills, 2020; Black Beauty, 2019).

The particle size distribution of each granular medium was measured by sieving samples for 15 minutes using a sieve shaker (CE Tyler RX-24, Combustion Engineering, New York, NY) and then weighing the material remaining on the series of sieves with opening sizes of 2.00, 1.70, 1.18, 1.00, 0.850, 0.710, 0.600, 0.500, 0.425, 0.355, 0.250, 0.212, 0.150, 0.125 and 0.053 mm based on the ASTM sieve size. The ρ_s of each granular medium were determined using the water displacement method (Dane and Topp, 2002).

3.3 Packing the Granular Media

A difficulty in using granular media is to establish and maintain a repeatable

packing ρ_b . Packaging these media at various controlled θ_w values is further challenging. Packing dry particles eliminates the effects of wet media packing. Packing in water to saturate the media can lead to particle segregation and unintended layering of the media. We employed the MSP method (Miura and Toki, 1982) to achieve a uniform dry granular medium ρ_b around the THPP. All samples were oven-dried at 105°C for at least 24 hours and stored in sealed plastic bags to cool down and to begin measurements. A small diameter (0.25”) funnel was positioned above a screen column as a hopper to maintain a uniform material flow. The stream of particles from the funnel was applied at a constant rate into a 220 mm long Lexan screen column (57 mm o.d., 51 mm i.d.) illustrated in Fig. 1a, containing five layers of steel wire screen (5 mm square openings), each layer 35 mm apart. The screen column was created by cutting 30 mm sections of the column and a 30 × 30 mm square screen and sandwiching the heated screen (using a torch) between two column sections, effectively melting the wire into the column ends that also melted together. The completed screen column was connected to the top of the THPP column with a sleeve so that particles poured into the screen column would randomly scatter as they descended into the THPP column and effectively pummel the deposited material surface as a means of settling that surface to a consistent, repeatable density. We found this method avoids the unintended compaction around rods resulting from insertion into prepacked material. The dry ρ_b values in repeated packing trials of each material were virtually identical using this approach, as demonstrated in Table 1, with the largest standard deviation being just 0.6% of the mean dry ρ_b value for Profile (Pro). The screen column was removed, and the packed column was ready for the first heat pulse measurements.

After obtaining measurements on the dry media, the same packed material was

saturated by injecting DI water into the media through the 1 cm diameter sintered stainless steel plate in the THPP base. The underside of the plate was glued to a barbed fitting and a small diameter tube that exited the lower pipe wall. The tube was useful for both adding and removing water from a sample. The Lexan column was sealed at the top using an O-ring adorned plug with a vacuum line connector exiting the top of the plug. We put the THPP column under a vacuum during water filling to minimize air entrapment in the granular medium. The total porosity ($= 1 - \rho_b / \rho_s$) of each packing was computed from ρ_b and ρ_s and used to determine the amount of water to inject to saturate the packed pore volume. After obtaining water-saturated measurements of the thermal properties, we connected a laboratory vacuum line, which maintained a static suction of -5.9 m and removed free water from the sintered stainless-steel plate (previous water inlet) with air. After 60 minutes of the de-watering process, thermal property values at the quasi-equilibrium θ_w (drained θ_w) were obtained. Water additions and removals from each sample were verified by measuring changes in total column mass with a balance. Following the drained θ_w measurements, the θ_w of the packed samples were determined using the oven-drying method (Dane and Topp, 2002). The granular media packing method described here provides (1) oven-dried-, (2) saturated- and (3) drained- θ_w determinations of thermal property values in each granular material.

3.4 Data Processing of Temperature Rise Data for Thermal Property Determinations

Thermal property (λ and C_v) values were estimated using a MATLAB program to fit the ICPC model (Eqs. 1–3) to the measured temperature rise with time data. The apparent rod spacing value (r_c) was based on measurements in agar-stabilized water reported by Naruke et al. (2021) as shown in Table 2. Naruke et al. (2021) also reported

the r_c values calibrated in air-free ice, and air-free ice could equally serve as calibration material for agar-stabilized water. Table 2 lists THPP rod configurations and input values, including the calibrated r_c and volumetric heat capacity for stainless steel and epoxy used in the ICPC model. Thermal diffusivity, κ , ($= \lambda/C_v$), was obtained using the fitted values of λ and C_v . Estimated C_v and λ at various θ_w conditions were used to determine parameter values for selected models of C_v (Eq. 4) and λ (Eqs. 5–15) for a θ_w range from oven-dry to saturation.

4. RESULTS AND DISCUSSION

4.1 Granular Media as Reference Standards

The particle size distribution of each testing media was characterized in Fig. 2 and Table 3 as the particle diameter (mm) through which x % of a test granular medium passed as well as the fine particle content, which passed through the 53 μm sieve. In most cases, diameters were greater than 53 μm , correlating with a sandy texture. The finest medium was aluminum oxide (Alu) and garnet (Gar), and the coarsest was pumice (Pum). Most of the particles in pumice (Pum) were larger than 1 mm, however, the sieving process broke particles down into smaller fractions in some of the weaker aggregated media, making particle diameter determination challenging. Soda-lime glass beads (Sod) showed a very narrow distribution, while Wedron sand (Wed) exhibited a relatively wide distribution. In addition to Wedron sand (Wed), both aluminum oxide (Alu) and garnet (Gar) exhibited similar effective particle size distributions. Coarse angular sand (Ang), Wedron sand (Wed), and fine silica sand (C778) had high quartz content (>90%), and these three materials presented similar particle size distributions. Each granular medium was carefully packed using the MSP method, which worked well for most granular media. However,

finer particles such as aluminum oxide (Alu) and garnet (Gar) passed through the screens and were less effectively scattered, leading to a cone-shaped surface rather than a flat surface during packing. A smaller mesh opening size may increase particle scattering for finer materials and be used as additional standard granular media.

4.2 Thermal Property Estimation in Granular Media

4.2.1 Thermal property determination using the air-MSP method

As shown in Table 1, the air-MSP method resulted in consistent ρ_b values for the different test media. Pumice (Pum) showed a relatively larger standard deviation of ρ_b value of 1.17 kg m^{-3} with a mean ρ_b value of 488 kg m^{-3} and we triplicated pumice trial to provide the likelihood of errors in estimated thermal property values. Thermal property (λ , C_v and κ) estimations using THPP measurements with two thermistor rod, T_a and T_b , with a triplicated air-MSP trial in oven-dried pumice showed small standard deviations of $1.8 \times 10^{-3} \text{ W m}^{-1} \text{ K}^{-1}$ in λ , $1.6 \times 10^{-2} \text{ MJ m}^{-3} \text{ K}^{-1}$ in C_v and $1.0 \times 10^{-2} \text{ mm}^2 \text{ s}^{-1}$ in κ , and each standard deviation value had less than 1, 3 and 4% in each of mean thermal properties (data not shown). Therefore, THPP measurements combined with the air-MSP method provided reproducible thermal property estimations in granular media.

4.2.2 Thermal property estimation at different water contents

Table 4 lists the averages and standard deviations (Stdev) of thermal property values estimated by fitting the ICPC model to triplicated measurements of temperature rise with time in both thermistor-rods, T_a and T_b , therefore six data sets, at oven-dry, saturated- and drained- θ_w conditions. We combined thermal property results from T_a and T_b to provide a range of errors in estimating each thermal property value. Estimated thermal property values exhibited ranges in C_v of 0.52 to $3.5 \text{ MJ m}^{-3} \text{ K}^{-1}$, in λ of 0.13 to 3.6 W m^{-1}

K^{-1} , and in κ of 0.17 to $1.4 \text{ mm}^2 \text{ s}^{-1}$. Most of the media showed minimal standard deviations at the oven-dry condition and larger standard deviations at drained- and saturation- θ_w conditions. The larger standard deviations at drained- and saturation- θ_w conditions in fine-textured granular media, such as fine sand (C778), Wedron sand (Wed), aluminum oxide (Alu) and garnet (Gar), might be due in part to trapped air between particles creating non-homogeneous conditions. The saturated θ_w value in these media during the infusion process was smaller than the porosity value. Dane and Hopmans (2002) reported that θ_w value at saturation during the wetting process is commonly about 85% of saturation θ_w at the complete saturation condition. While the dry and saturated media are considered to possess uniform properties and resulting repeatable thermal properties, the partially wetted media also showed small deviations in their thermal property determinations as result, indicating that the water distribution in the column at the drained θ_w was also relatively uniform. Thermal properties (C_v , λ and κ) at our three target θ_w conditions represented different combinations of the three solid, water and air phases within the testing media. For the oven-dry condition, thermal properties depended only on the solid and air phases, while all three phases affected thermal properties for saturated- and for drained-conditions. The C_v measurements at the three different θ_w conditions presented increasing C_v as θ_w increased. The two aggregated media (Pro and Pum) had oven-dried C_v values at around half of the rest of the granular media tested, due to the lower ρ_b values (higher air content). Oven-dry λ measurements in Table 4 exhibited a narrow range from 0.13 to $0.40 \text{ W m}^{-1} \text{ K}^{-1}$, while saturated λ had a much larger range from 0.61 to $3.71 \text{ W m}^{-1} \text{ K}^{-1}$. The three different quartz sands (C778, Wed and Ang) exhibited the highest oven-dry λ values ranging between 0.36 and $0.40 \text{ W m}^{-1} \text{ K}^{-1}$, while the two aggregated media (Pro and Pum) exhibited the lowest

oven-dry λ values of 0.17 and 0.13 W m⁻¹ K⁻¹, respectively, due to the lower ρ_b values. Although particle shape (e.g., spherical and ellipsoidal) and packing method (e.g., random packing vs. vibration) affect ρ_b and contact between particle to particle and particle to a different phase(s) (Dai et al., 2019), our thermal property measurements using THPP did not show substantial difference among three different categories (spherical, angular and aggregated) except for aggregated- and non-aggregated- media.

Some of these test media exhibited a rapid increase in λ when θ_w increased from oven-dry to the drained condition, followed by a more moderate increase in λ after θ_w increased between the drained condition and saturation (e.g., Ang, C778, Wed and Gar). Other media exhibited a gradual monotonic increase in λ for the entire θ_w range (e.g., Sod, Coa, Pro, and Pum). The rapid increase of λ in the relatively dry condition was caused by growing pendular rings (also called capillary bridges) (de Bisschop and Rigole, 1982; Rose, 1958) which increased the contact area, and thus, the heat transfer between solid particles. This occurred until the effect of water became insignificant when θ_w was high. Among the three λ functions of quartz sand (Ang, C778 and Wed), the fine sand (C778) with the highest ρ_b (1829 kg m⁻³) had the largest λ function, while Ang with the lowest ρ_b (1607 kg m⁻³) presented the lowest values of thermal conductivity. Soda-line glass beads (Sod) and coal slag (Coa) had similar λ functions, explained by similar quartz content and ρ_b . Aggregated media such as Profile (Pro) and pumice (Pum) had relatively small λ across a wide range of θ_w . Because both Profile and pumice had internal aggregation, intra-aggregate entrapped air had a large effect on λ , while water mainly filled most of the external aggregate pores and internal aggregate pores were filled mostly with air. Thermal diffusivity (κ) measurements showed the largest κ at the drained θ_w in all media except for

pumice (Pum). Since κ was calculated as $\kappa = C_v / \lambda$, moderate increases in λ for θ_w beyond the drained condition to saturation led to decreasing κ toward the saturated condition.

These coarse granular media presented distinct wetting/drying fronts when water was pushed into or drained from the column. The ICPC model assumed a uniform distribution of materials including water and solid phases, therefore, our thermal property measurements were limited at the three target θ_w conditions for our vertical rod orientation. The vertical orientation was also advantageous to provide repeatable bulk packing density in the granular media using the air-MSP method.

4.3 Thermal Property Models

In Fig. 3, the average- and standard deviation values of C_v versus θ_w for the eight granular media listed in Table 4 were plotted as circle symbols and black solid bars. The optimized mixing model of C_v (Eq. 4) using the fitted parameter, c_s listed in **Error! Reference source not found.** for each media is exhibited as the solid line. Since the fitted parameter was only c_s , which determined the offset value of the C_v function, the slope of all lines was determined by θ_w multiplied by the volumetric heat capacity of water ($C_w = \rho_w \times c_w = 4.18 \text{ MJ m}^{-3} \text{ K}^{-1}$). The C_v function of aggregated media, Profile and pumice as shown as black- and gray- circles showed lower trends than for other media due to lower ρ_b values of 693 and 488 kg m^{-3} , respectively

Estimated c_s in testing media (**Error! Reference source not found.**) showed that soda-lime glass beads (Sod) and pumice (Pum) had the highest- and lowest- c_s of 846 and 652 $\text{J kg}^{-1} \text{ K}^{-1}$, respectively. The average estimated c_s values for three different quartz sands (Ang, C778, Wed) was 781 $\text{J kg}^{-1} \text{ K}^{-1}$ with highest- and lowest- c_s values of 820 and 761 $\text{J kg}^{-1} \text{ K}^{-1}$, in Wedron sand (Wed) and C778, respectively. Reported c_s values in soda-lime glass beads (Ham and Benson, 2004; Tarara and Ham, 1997) and quartz sand (Bristow et al., 1994) were 794 and 802 $\text{J kg}^{-1} \text{ K}^{-1}$, respectively. Although our estimated c_s value in soda-lime glass beads (Sod) was greater than the reported values, our c_s in quartz sands (Ang, C778, Wed)

followed literature values. Thermal conductivity functions using the mixing model (Eqs. 5–8), Campbell (1985) model (Eqs. 9 and 10), Chung and Horton (1987) model (Eq. 11), Lu and Dong (2015) model (Eq. 12) and Ghanbarian and Daigle (2016) model (Eqs. 13–15) were compared with THPP determined λ values in

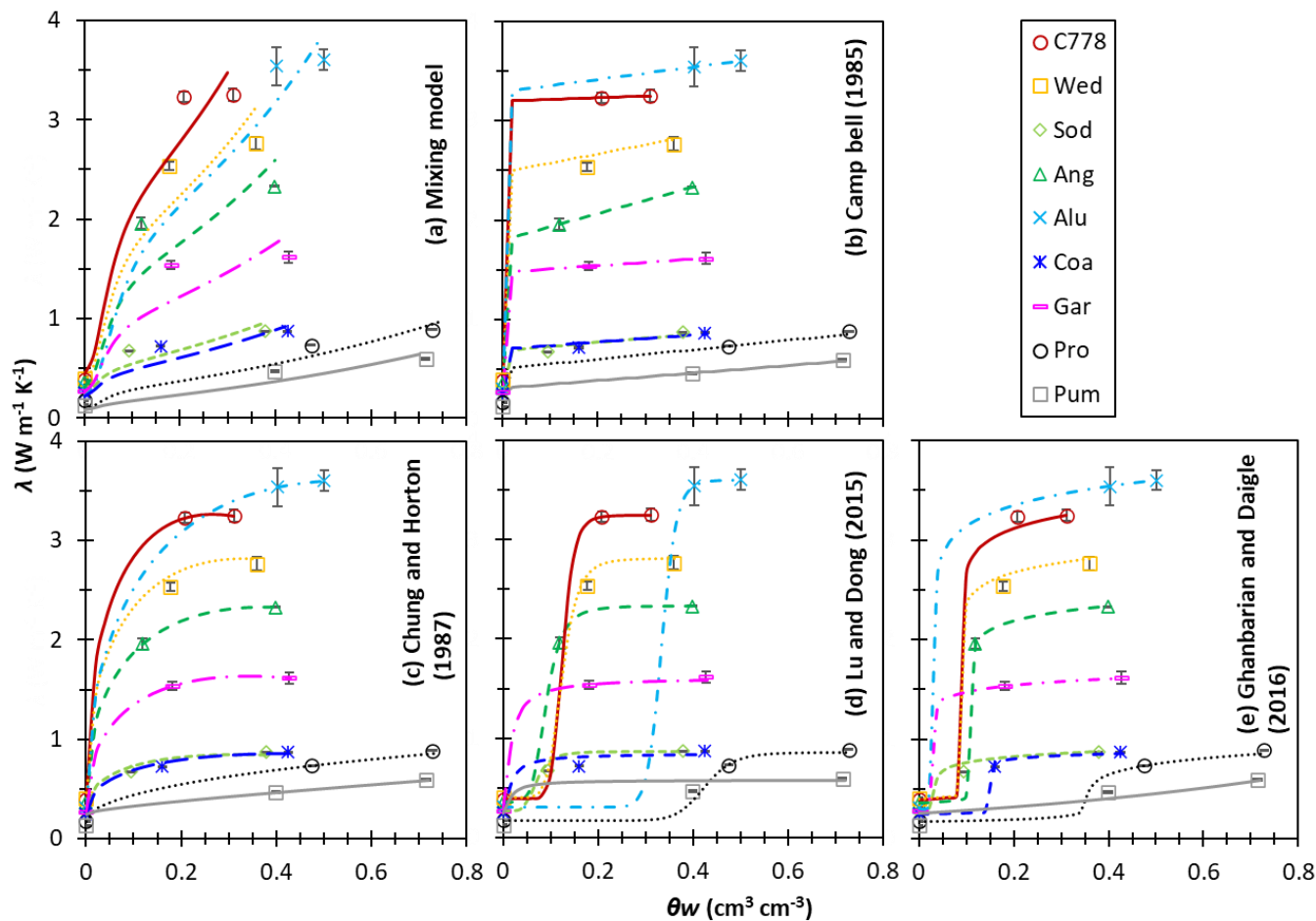


Fig. 4a–4e, respectively. Square symbols and the black bars represent the average and the standard deviation of λ estimates in Table 4, respectively. Fitted λ models are shown as lines in

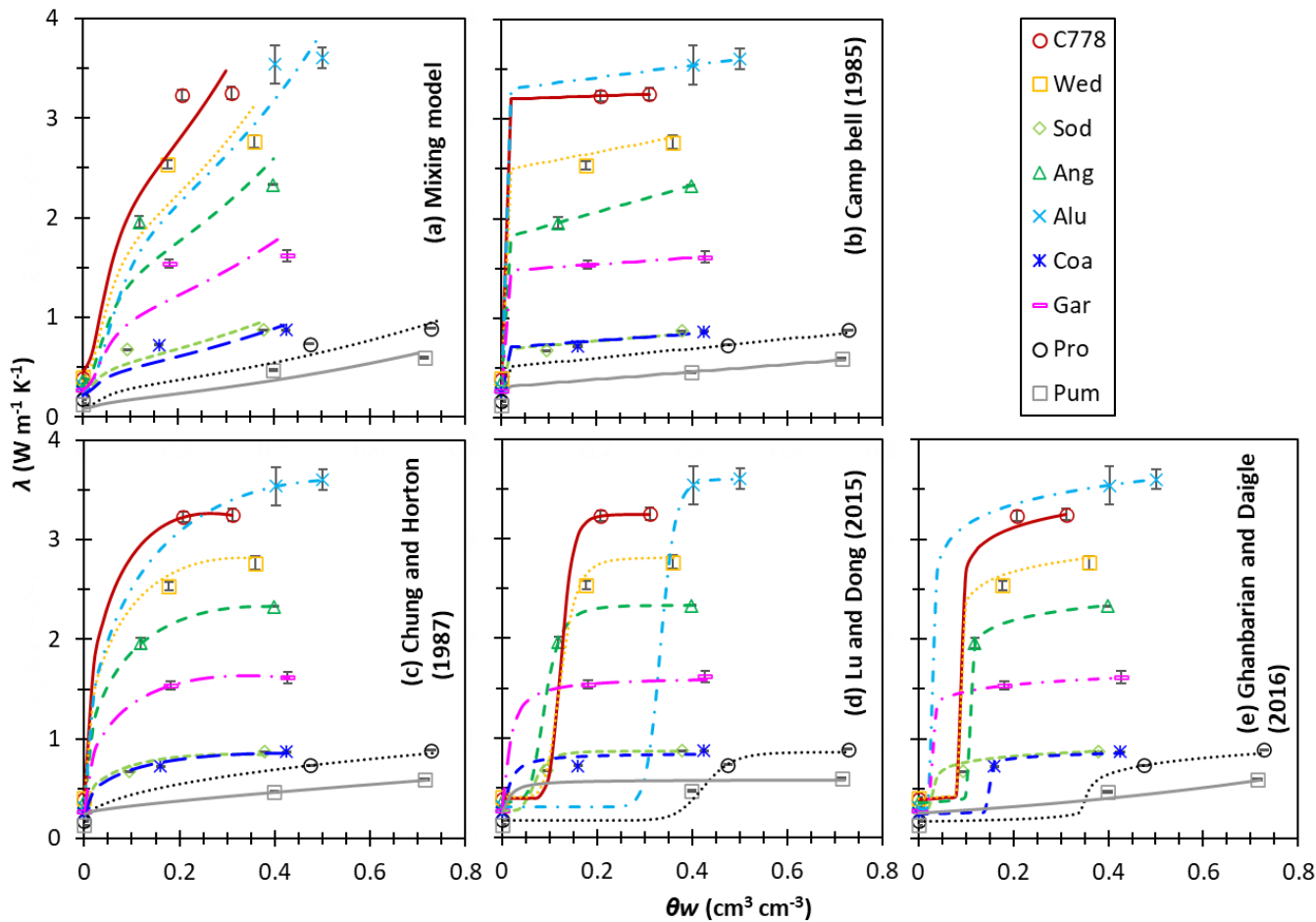


Fig. 4a–4e, and optimized model parameters are presented in **Error! Reference source not found.** With only three λ measurement points at three different θ_w conditions (i.e., oven-dry, saturated and drained) in coarse granular media, it was challenging to predict the transition point in the existing λ functions because of the lack of measurements at additional low θ_w . The model fitting could be improved if additional measurements of λ at low θ_w values were available.

In

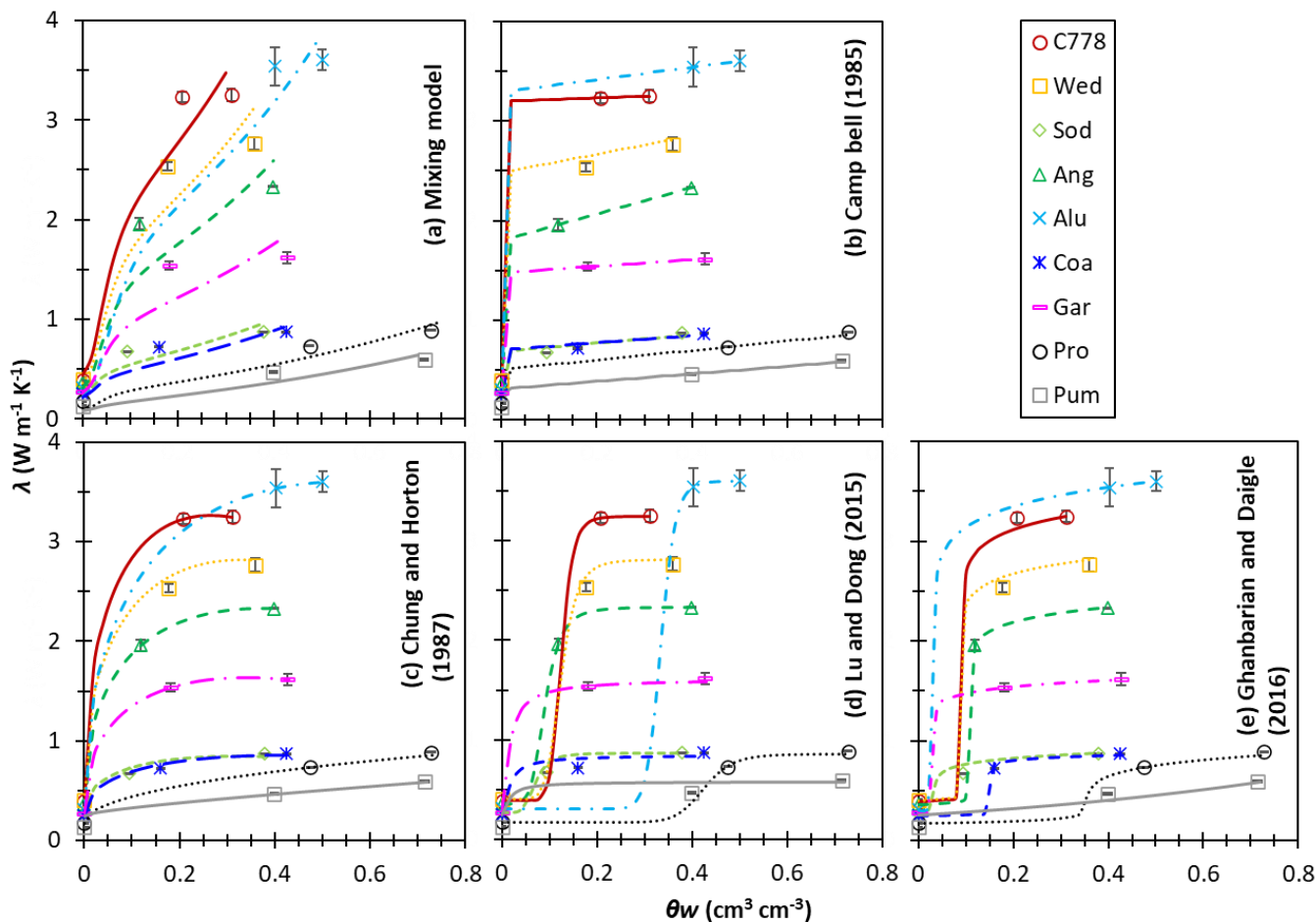


Fig. 4a, the mixing model agreed well with λ at the oven-dry condition in all media, however, the mixing model showed an underestimation of λ values at the drained θ_w while overestimating λ values at saturation. The Campbell (1985) model exhibited an earlier λ transition point at the θ_w value of around 0.04 cm³ cm⁻³ because the parameter, C , in the model was the only parameter to determine the transition point, and we assumed $C = 83$ due to the coarse texture of our media (see **Error! Reference source not found.**) as discussed earlier. Parameters presented in **Error! Reference source not found.** and were used to inform the empirical Campbell (1985) model shown in

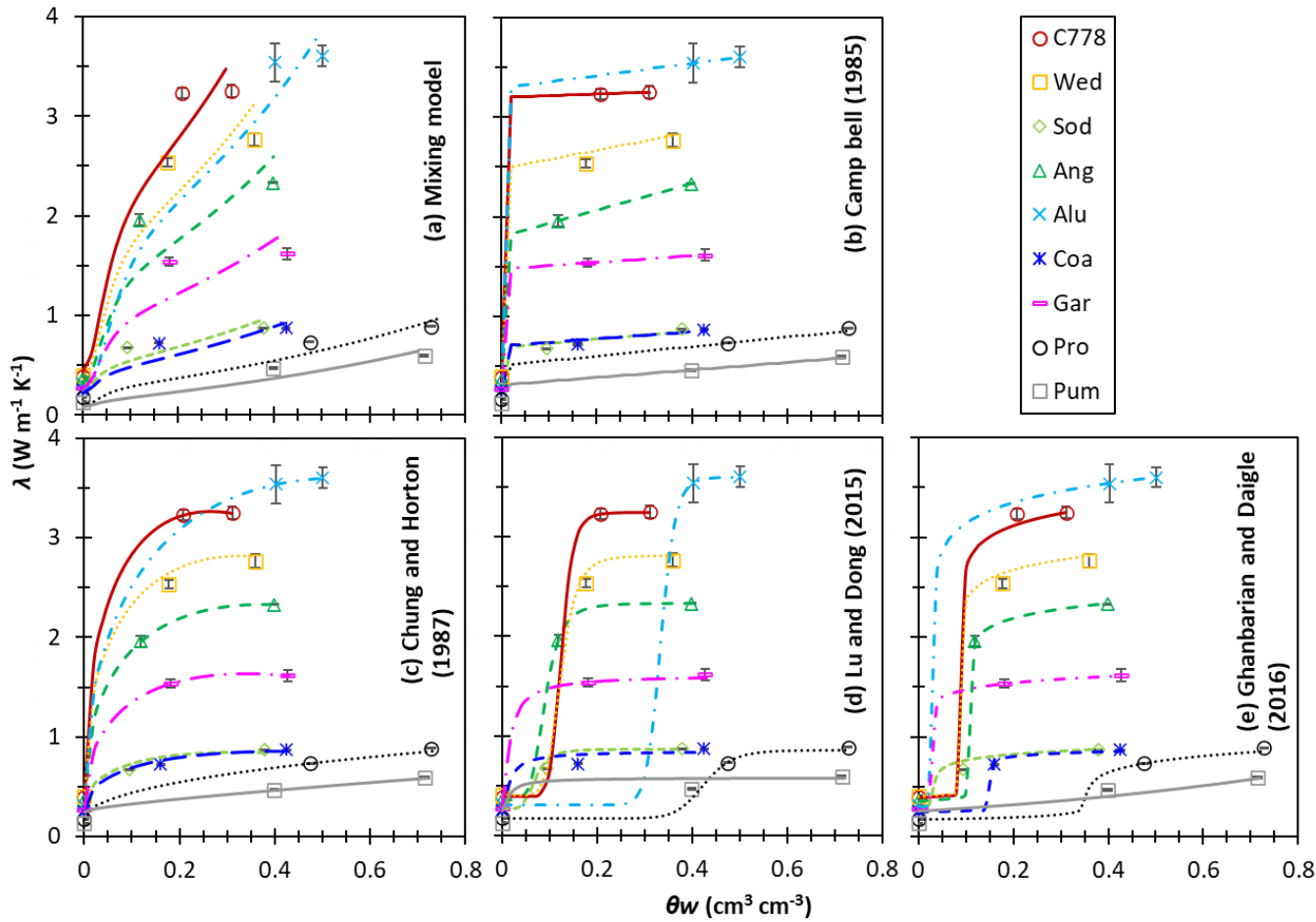


Fig. 4b. The empirical Chung and Horton (1987) model showed a smooth increase in λ at lower- θ_w ranges, unlike the Campbell (1985) model. The Chung and Horton (1987) model parameters, $b1$, $b2$ and $b3$ were presented in **Error! Reference source not found.**, and $b1$ determined the λ_{dry} was the same value in all media as parameter D in the Campbell (1985) model. The conceptual Lu and Dong (2015) model created a sigmoidal function in most media except for coal slag (Coa), garnet (Gar) and pumice (Pum). The model used the parameters of λ_{dry} and λ_{sat} as shown in Table 5 to set a lower- and higher- end of the model with curve shape parameters θ_f and m , therefore the Lu and Dong (2015) model exhibited a plateau at higher θ_w values. Lu and Dong (2015) provided the relationship between water retention characteristics and their curve shape parameters θ_f , which might

increase the accuracy of the model prediction if these water retention parameters were available. For example, Profile has almost 1:1 fraction of dual porosity structure described as inter-aggregate (0.37) and intra-aggregate pores (0.37) where water held in macro pores drain at the matric potential around -25 cm (Heinse et al., 2007). The θ_f value of Profile (Pro) in the Lu and Dong (2015) model was $0.42 \text{ cm}^3 \text{ cm}^{-3}$, which was close to the threshold θ_w ($0.37 \text{ cm}^3 \text{ cm}^{-3}$) of the dual porosity structure. The theoretical Ghanbarian and Daigle (2016) model produced a variety of $\lambda(\theta_w)$ curves where the curve exhibited a monotonic increase in P_{um} (gray) due to a larger t_s value ($t_s = 2$). The Ghanbarian and Daigle (2016) model also showed a curve similar to a step-function when t_s was close to 0, where λ showed a substantial increase at $\theta_w = \theta_{cw}$ as shown in **Error! Reference source not found.**

Unlike the sigmoid function by the Lu and Dong (2015) model, the Ghanbarian and Daigle (2016) still exhibited a monotonic increase after λ showed a substantial increase ($\theta_w > \theta_{wc}$) in some media (e.g., C778). The Ghanbarian and Daigle (2016) model in Profile (Pro) also showed a λ curve which was similar to the λ curve using the Lu and Dong (2015) model. Although the θ_{wc} optimization in Profile (Pro) showed a potential to relate the media's water retention characters and the θ_{wc} value, the θ_{wc} values optimized for finer granular media (e.g., aluminum oxide (Alu) and garnet (Gar)) could be poorly described due to our limited data. Since both aluminum oxide (Alu) and garnet (Gar) had finer particle sizes, the expected θ_{wc} values may be much greater than the optimized θ_{wc} values.

The accuracy of C_v and λ models in test media was evaluated by calculating RMSE (Eq. 15), and values are presented in Table 6. The C_v mixing model showed consistent RMSE values with a minimum RMSE of $0.11 \text{ MJ m}^{-3} \text{ K}^{-1}$ in coarse angular sand (Ang) and a maximum RMSE of $0.29 \text{ MJ m}^{-3} \text{ K}^{-1}$ in garnet (Gar). Garnet (Gar) exhibited

relatively large fluctuations in THPP C_v determinations, which increased RMSE in the C_v model fitting. Four of the five λ models (the mixing model was an exception) showed almost the same RMSE value in each test media. The λ mixing model RMSE values were more than double the values of the other media, and therefore we do not recommend the application of the mixing model of λ unless the model is well optimized with λ measurements at lower θ_w conditions.

Finally, Fig. 5 presents the THPP-determined C_v and λ values and the resulting values of κ ($\kappa = \lambda/C_v$) for coarse angular sand (Ang) at the oven-dried-, saturated- and drained- θ_w conditions. Fig. 5a–5e also includes the optimized mixing model results for C_v as blue lines, while each black curve represents the optimized λ model using (a) mixing model, (b) Campbell (1985) model, (c) Chung and Horton (1987) model, (d) Lu and Dong (2015) model and (e) Ghanbarian and Daigle (2016) model, respectively. The red curves represent κ values computed from the optimized models of C_v and λ as ($\kappa = \lambda/C_v$). The λ model selection directly affects κ values. For example, the computed κ using the mixing model of C_v and λ showed underestimations in the drained water values due to the underestimation of λ with the mixing model (Fig. 5a). Thermal property values at the water content lower than the drained water content values are especially important for simulating the transport of water, gas and energy under dry conditions, therefore selecting the most representative thermal conductivity model is important for an accurate representation of κ .

5. CONCLUSIONS

This study presented concepts for standardized estimated thermal properties of nine commercially available coarse granular media at different volumetric water content (θ_w) conditions using a Three-rod Heat Pulse Probe (THPP). Commercially available granular

media included spherical-, angular- and aggregated- materials. We reported particle size distribution for each media, and the particle density (ρ_s) values ranged from 1718 to 4019 kg m⁻³. The Multiple Sieving Pluviation (MSP) method provided highly repeatable packing represented by bulk density (ρ_b) values ranging from 488 to 2205 kg m⁻³ in these granular materials within 0.6 % of standard deviation. The Identical Cylindrical Perfect Conductors (ICPC) model was applied to the THPP temperature rise measurements to determine the thermal property values of each granular material at three different θ_w values. Oven-dry granular media exhibited thermal property values ranging from 0.52 to 1.6 MJ m⁻³ K⁻¹ for volumetric heat capacity (C_v), 0.13 to 0.4 W m⁻¹ K⁻¹ for thermal conductivity (λ) and 0.17 to 0.29 mm² s⁻¹ for thermal diffusivity (κ), and the thermal property values of saturated media ranged from 2.7 to 3.5 MJ m⁻³ K⁻¹ for C_v , 0.59 to 3.6 W m⁻¹ K⁻¹ for λ and 0.19 to 1.2 mm² s⁻¹ for κ . Estimated thermal properties (C_v , λ and κ) with a wide range of θ_w (i.e., from oven-dry to saturation) at highly repeatable ρ_b in various granular media improve thermal property sensor development and could also serve as additional calibration media. We also provided optimized parameters for existing thermal property (C_v and λ) models based on our granular media measurements. The C_v mixing model well described the THPP-determined C_v values as well as a linear model in all media. The λ mixing model showed more than double RMSE values in all media compared to the other four models including two empirical λ models by Campbell (1985) and Chung and Horton (1987), the conceptual λ model developed by Lu and Dong (2015), as well as the theoretical model developed by Ghanbarian and Daigle (2016). These four models showed more flexibility in characterizing THPP-determined λ values compared to the λ mixing model, however, insufficient λ data at low-range θ_w conditions leaves some uncertainty in the

optimal shape of the λ function. As mentioned, a limitation of this approach is the lack of THPP measurements at low-range θ_w conditions and additional information (e.g., soil hydraulic properties) of testing media could also improve the parameter optimization for λ models.

REFERENCES

ASTM Committee D-18 on Soil and Rock., 2006. Standard test methods for minimum index density and unit weight of soils and calculation of relative density. ASTM International, Philadelphia, Pa. :

ASTM International. Subcommittee D18. 12 on Rock Mechanic, 2008. Standard test method for determination of thermal conductivity of soil and soft rock by thermal needle probe procedure.

Bilskie, J.R., Horton, R., Bristow, K.L., 1998. Test of a dual-probe heat-pulse method for determining thermal properties of porous materials¹. *Soil science* 163, 346–355.

Bittelli, M., Campbell, G.S., Tomei, F., 2015. *Soil Physics with Python: Transport in the Soil–Plant–Atmosphere System* - Oxford Scholarship.

Bristow, K.L., 1998. Measurement of thermal properties and water content of unsaturated sandy soil using dual-probe heat-pulse probes. *Agric For Meteorol* 89, 75–84. [https://doi.org/10.1016/S0168-1923\(97\)00065-8](https://doi.org/10.1016/S0168-1923(97)00065-8)

Bristow, K.L., Kluitenberg, G.J., Horton, R., 1994. Measurement of Soil Thermal Properties with a Dual-Probe Heat-Pulse Technique. *Soil Science Society of America Journal* 58, 1288–1294. <https://doi.org/10.2136/sssaj1994.03615995005800050002x>

Campbell, G.S., 1985. Soil Temperature and Heat Flow, in: *Soil Physics with Basic*. Elsevier, pp. 26–39. [https://doi.org/10.1016/s0166-2481\(08\)70134-x](https://doi.org/10.1016/s0166-2481(08)70134-x)

Campbell, G.S., Calissendorff, C., Williams, J.H., 1991. Probe for Measuring Soil Specific Heat Using A Heat-Pulse Method. *Soil Science Society of America Journal* 55, 291–293. <https://doi.org/10.2136/sssaj1991.03615995005500010052x>

Campbell, G.S., Jungbauer, J.D., Bidlake, W.R., Hungerford, R.D., 1994. Predicting the effect of temperature on soil thermal conductivity. *Soil Sci* 158, 307–313. <https://doi.org/10.1097/00010694-199411000-00001>

Chung, S., Horton, R., 1987. Soil heat and water flow with a partial surface mulch. *Water Resour Res* 23, 2175–2186. <https://doi.org/10.1029/WR023i012p02175>

Cobos, D.R., Baker, J.M., 2003. In Situ Measurement of Soil Heat Flux with the Gradient Method. *Vadose Zone Journal* 2, 589–594. <https://doi.org/10.2113/2.4.589>

Dai, W., Hanaor, D., Gan, Y., 2019. The effects of packing structure on the effective thermal conductivity of granular media: A grain scale investigation. *International Journal of Thermal Sciences* 142, 266–279. <https://doi.org/10.1016/J.IJTHERMALSCI.2019.04.028>

Dane, J.H., Hopmans, J.W., 2002. Hanging water column, in: Dane, J.H., Topp, G.C. (Eds.), *Method of Soil Analysis: Part 4 Physical Methods*. Soil Science Society of America, pp. 680–683.

Dane, J.H., Topp, G.C., 2002. *Methods of Soil Analysis*, SSSA Book Series. Soil Science Society of America, Madison, WI, USA. <https://doi.org/10.2136/sssabookser5.4>

de Bisschop, F.R.E., Rigole, W.J.L., 1982. A physical model for liquid capillary bridges between adsorptive solid spheres: The nodoid of plateau. *J Colloid Interface Sci* 88, 117–128. [https://doi.org/10.1016/0021-9797\(82\)90161-8](https://doi.org/10.1016/0021-9797(82)90161-8)

de Vries, D. A., 1963. Thermal properties of soils, in: van Wijk, W.R. (Ed.), *Physics of Plant Environment*. North-Holland Publishing Company, Amsterdam, pp. 210–235.

Dong, Y., McCartney, J.S., Lu, N., 2015. Critical Review of Thermal Conductivity Models for Unsaturated Soils. *Geotechnical and Geological Engineering* 33, 207–221.

<https://doi.org/10.1007/s10706-015-9843-2>

Farouki, O.T., 1981. Thermal properties of soils.

Gan, J., Yu, A., 2020. DEM study on the packing density and randomness for packing of ellipsoids. *Powder Technol* 361, 424–434.

<https://doi.org/10.1016/J.POWTEC.2019.07.012>

Ghanbarian, B., Daigle, H., 2016. Thermal conductivity in porous media: Percolation-based effective-medium approximation. *Water Resour Res* 52, 295–314.

<https://doi.org/10.1002/2015WR017236>

Guaraglia, D.O., Pousa, J.L., 1999. An Electrical Model of Heat Flow in Soil. *Soil Science Society of America Journal* 63, 457–463.

<https://doi.org/10.2136/SSSAJ1999.03615995006300030006X>

Ham, J.M., Benson, E.J., 2004. On the Construction and Calibration of Dual-Probe Heat Capacity Sensors. *Soil Science Society of America Journal* 68, 1185–1190.

<https://doi.org/10.2136/sssaj2004.1185>

He, H., Zhao, Y., Dyck, M.F., Si, B., Jin, H., Lv, J., Wang, J., 2017. A modified normalized model for predicting effective soil thermal conductivity. *Acta Geotech* 12, 1281–1300. <https://doi.org/10.1007/S11440-017-0563-Z/FIGURES/5>

Heinse, R., Jones, S.B., Steinberg, S.L., Tuller, M., Or, D., 2007. Measurements and Modeling of Variable Gravity Effects on Water Distribution and Flow in Unsaturated Porous Media. *Vadose Zone Journal* 6, 713–724. <https://doi.org/10.2136/VZJ2006.0105>

Heitman, J.L., Horton, R., Sauer, T.J., DeSutter, T.M., 2008. Sensible Heat Observations Reveal Soil-Water Evaporation Dynamics. *J Hydrometeorol* 9, 165–171.

<https://doi.org/10.1175/2007JHM963.1>

Hopmans, J.W., Šimunek, J., Bristow, K.L., 2002. Indirect estimation of soil thermal properties and water flux using heat pulse probe measurements: Geometry and dispersion effects. *Water Resour Res* 38, 7-1-7–14. <https://doi.org/10.1029/2000wr000071>

Kluitenberg, G.J., Philip, J.R., 1999. Dual Thermal Probes near Plane Interfaces. *Soil Science Society of America Journal* 63, 1585–1591. <https://doi.org/10.2136/SSSAJ1999.6361585X>

Knight, J.H., Kluitenberg, G.J., Kamai, T., Hopmans, J.W., 2012. Semianalytical Solution for Dual-Probe Heat-Pulse Applications that Accounts for Probe Radius and Heat Capacity. *Vadose Zone Journal* 11. <https://doi.org/10.2136/vzj2011.0112>

Kodicherla, S.P.K., Gong, G., Fan, L., Moy, C.K.S., He, J., 2018. Effects of preparation methods on inherent fabric anisotropy and packing density of reconstituted sand. <http://www.editorialmanager.com/cogenteng> 5, 1–14. <https://doi.org/10.1080/23311916.2018.1533363>

Liu, G., Wen, M., Chang, X., Ren, T., Horton, R., 2013. A Self-Calibrated Dual Probe Heat Pulse Sensor for In Situ Calibrating the Probe Spacing. *Soil Science Society of America Journal* 77, 417–421. <https://doi.org/10.2136/SSSAJ2012.0434N>

Lu, N., Dong, Y., 2015. Closed-Form Equation for Thermal Conductivity of Unsaturated Soils at Room Temperature. *Journal of Geotechnical and Geoenvironmental Engineering* 141, 04015016. [https://doi.org/10.1061/\(ASCE\)GT.1943-5606.0001295](https://doi.org/10.1061/(ASCE)GT.1943-5606.0001295)

Lu, S., Lu, Y., Peng, W., Ju, Z., Ren, T., 2019. A generalized relationship between thermal conductivity and matric suction of soils. *Geoderma* 337, 491–497. <https://doi.org/10.1016/j.geoderma.2018.09.057>

Lu, Y., Lu, S., Horton, R., Ren, T., 2014. An Empirical Model for Estimating Soil

Thermal Conductivity from Texture, Water Content, and Bulk Density. *Soil Science Society of America Journal* 78, 1859–1868. <https://doi.org/10.2136/sssaj2014.05.0218>

Miura, S., Toki, S., 1982. A Sample Preparation Method and its Effect on Static and Cyclic Deformation-Strength Properties of Sand. *Soils and Foundations* 22, 61–77. <https://doi.org/10.3208/SANDF1972.22.61>

Naruke, C., Sheng, W., Zhou, R., Jones, S.B., 2021. Standardizing Heat Pulse Probe measurements for thermal property determination using ice and water. *Agric For Meteorol* 308–309, 108610. <https://doi.org/10.1016/J.AGRFORMET.2021.108610>

Ochsner, T.E., Sauer, T.J., Horton, R., 2007. Soil heat storage measurements in energy balance studies. *Agron J* 99, 311–319. <https://doi.org/10.2134/agronj2005.0103S>

Peng, W., Lu, Y., Ren, T., Horton, R., 2021. Application of infinite line source and cylindrical-perfect-conductors theories to heat pulse measurements with large sensors. *Soil Science Society of America Journal* 85, 1050–1059. <https://doi.org/10.1002/SAJ2.20250>

Peng, W., Lu, Y., Xie, X., Ren, T., Horton, R., 2019. An Improved Thermo-TDR Technique for Monitoring Soil Thermal Properties, Water Content, Bulk Density, and Porosity. *Vadose Zone Journal* 18, 1–9. <https://doi.org/10.2136/vzj2019.03.0026>

Rose, W., 1958. Volumes and Surface Areas of Pendular Rings. *J Appl Phys* 29, 687. <https://doi.org/10.1063/1.1723251>

Sadeghi, M., Ghanbarian, B., Horton, R., 2018. Derivation of an Explicit Form of the Percolation-Based Effective-Medium Approximation for Thermal Conductivity of Partially Saturated Soils. *Water Resour Res* 54, 1389–1399. <https://doi.org/10.1002/2017WR021714>

Shi, J., Haegeman, W., Mascini, A., Cnudde, V., 2021. X-ray analysis on the effect

of sample preparation on the microstructure of calcareous sands. *Marine Georesources and Geotechnology* 39, 302–311. <https://doi.org/10.1080/1064119X.2019.1698680>

Tabaroei, A., Abrishami, S., Hosseininia, E.S., 2017. Comparison between Two Different Pluviation Setups of Sand Specimens. *Journal of Materials in Civil Engineering* 29, 04017157. [https://doi.org/10.1061/\(ASCE\)MT.1943-5533.0001985](https://doi.org/10.1061/(ASCE)MT.1943-5533.0001985)

Tarara, J.M., Ham, J.M., 1997. Measuring soil water content in the laboratory and field with dual-probe heat-capacity sensors. *Agron J* 89, 535–542. <https://doi.org/10.2134/agronj1997.00021962008900040001x>

Tian, Z., Lu, Y., Horton, R., Ren, T., 2016. A simplified de Vries-based model to estimate thermal conductivity of unfrozen and frozen soil. *Eur J Soil Sci* 67, 564–572. <https://doi.org/10.1111/EJSS.12366>

van Genuchten, M.Th., 1980. A Closed-form Equation for Predicting the Hydraulic Conductivity of Unsaturated Soils. *Soil Science Society of America Journal* 44, 892–898. <https://doi.org/10.2136/SSSAJ1980.03615995004400050002X>

Yang, C., Sakai, M., Jones, S.B., 2013. Inverse method for simultaneous determination of soil water flux density and thermal properties with a penta-needle heat pulse probe. *Water Resour Res* 49, 5851–5864. <https://doi.org/10.1002/wrcr.20459>

Yu, A.B., An, X.Z., Zou, R.P., Yang, R.Y., Kendall, K., 2006. Self-assembly of particles for densest packing by mechanical vibration. *Phys Rev Lett* 97, 265501. <https://doi.org/10.1103/PHYSREVLETT.97.265501/FIGURES/4/MEDIUM>

Zhang, M., Lu, Y., Ren, T., Horton, R., 2020. In-situ probe spacing calibration improves the heat pulse method for measuring soil heat capacity and water content. *Soil Science Society of America Journal* 84, 1620–1629. <https://doi.org/10.1002/SAJ2.20124>

Table 1. Particle- and bulk densities (ρ_s and ρ_b), porosity and quartz (SiO₂) fraction of granular media.

Name	Code	ρ_s kg m ⁻³	ρ_b kg m ⁻³	Porosity	SiO ₂ fraction
Spherical granular media					
Fine sand	C778	2653±8.55	1829±1.77	0.31	0.95 – 0.99 ^{†‡}
Wedron sand	Wed	2674±17.3	1744±1.24	0.35	0.99 [§]
Soda-lime glass beads	Sod	2500 [†]	1556±1.78	0.38	0.65 – 0.75 [†]
Angular granular media					
Coarse angular sand	Ang	2637±11.0	1607±0.84	0.39	0.9 [‡]
Aluminum Oxide	Alu	4019±16.8	1995±2.27	0.50	0.007 (Al ₂ O ₃ 0.96) [#]
Coal slag	Coa	2776±45.6	1616±1.65	0.42	0.41 – 0.53 ^{††}
Garnet	Gar	3900±8.67	2205±1.30	0.43	n/a
Aggregated granular media					
Profile	Pro	2525±12.1	693±4.18	0.73	0.74 [¶]
Pumice	Pum	1718±28.3	488.3±1.17	0.72	n/a

[†] Mo-sci (2020): <https://mo-sci.com/wp-content/uploads/product-docs/glass-microspheres/GL0191-Data-Sheet.pdf>; [‡] Unimin (2020): https://www.coviacorp.com/media/dquhr5ed/granusil_tds_emmett_026_0719_bld_eng.pdf#search=granusil%202075; [§] Wedron Silica (2020): <https://www.smooth-on.com/tb/files/WedronSilica.pdf>; [¶] Profile (2020): <http://www.profileevs.com/resources/article/greens-grade-emerald-standard-specifications>; [#] Washintonmills (2020): <https://www.washingtonmills.com/products/brown-fused-aluminum-oxide>; ^{††} Blackbeauty (2020): https://www.blackbeautyabrasives.com/application/files/2015/8644/1909/SDS__Original_BLACK_BEAUTY_Jan_2020.pdf; ^{‡‡} US Silica (2020): <https://www.ussilica.com/support/guides-working-safely>

Table 2. Calibrated apparent rod spacing in agar-stabilized water (r_c) and thermistor rod dimensions and volumetric heat capacities of the THPP components (after Naruke et al. (2021)).

	Calibration	Thermistor rod dimension				Volumetric heat capacity		
	r_c	r_{phy}	L	d_o	d_e	C_{SS}	C_E	C_o
			mm				$\text{MJ m}^{-3} \text{K}^{-1}$	
T_a	6.96	6.87	50	2.4	0.61	4	2.03	3.87
T_b	6.96	6.94	"	"	"	"	"	"

Table 3. Diameters through which, respectively, 90%, 50% and 10% of the selected granular media passed. (% Fines is the mass of particles passing the 0.053 mm sieve)

Granular media	d_{90}	d_{50}	d_{10}	Fines
		mm		%
C778	0.500	0.425	0.355	0
Wed	0.400	0.250	0.150	2.7
Sod	0.600	0.500	0.425	0
Ang	1.18	0.850	0.600	0
Alu	0.212	0.150	0.125	0.3
Coa	0.600	0.400	0.355	0.1
Gar	0.212	0.150	0.125	1.2
Pro	0.710	0.600	0.425	0
Pum	2.00	1.70	1.00	

Table 4. Average and standard deviation (Stdev) of estimated C_v and λ , calculated $\kappa (= C_v / \lambda)$ in granular media at oven-dry, saturated- and drained-water content (θ_w) conditions using the THPP measurements.

Granular media	θ_w	C_v		λ		$\kappa (= C_v / \lambda)$	
		Average	Stdev	Average	Stdev	Average	Stdev
	$\text{cm}^3 / \text{cm}^3$	$\text{MJ m}^{-3} \text{K}^{-1}$		$\text{W m}^{-1} \text{K}^{-1}$		$\text{mm}^2 \text{s}^{-1}$	
C778	0	1.3	0.019	0.39	0.0036	0.29	0.0046
	0.21	2.3	0.16	3.2	0.053	1.4	0.11
	0.31	2.7	0.15	3.3	0.061	1.2	0.092
Wed	0	1.4	0.046	0.40	0.014	0.28	0.0060
	0.18	2.1	0.11	2.5	0.043	1.2	0.080
	0.36	2.7	0.25	2.8	0.065	1.0	0.071
Sod	0	1.5	0.072	0.27	0.015	0.18	0.004
	0.095	1.7	0.024	0.68	0.0018	0.39	0.0056
	0.38	2.8	0.0077	0.87	0.0022	0.32	0.00022
Ang	0	1.3	0.011	0.36	0.0041	0.28	0.00093
	0.12	1.8	0.051	0.91	0.054	1.1	0.057
	0.40	2.7	0.0016	2.3	0.0022	0.85	0.00030
Alu	0	1.5	0.061	0.31	0.014	0.20	0.0011
	0.40	3.2	0.16	3.5	0.19	1.1	0.11
	0.50	3.5	0.20	3.6	0.10	1.0	0.087
Coa	0	1.3	0.034	0.25	0.0062	0.20	0.0067
	0.16	2.0	0.067	0.41	0.0075	0.36	0.0082
	0.43	2.9	0.011	0.87	0.0043	0.31	0.0023
Gar	0	1.6	0.080	0.28	0.018	0.17	0.0038
	0.18	2.5	0.15	1.5	0.042	0.61	0.025
	0.43	3.0	0.17	1.6	0.059	0.55	0.029
Pro	0	0.63	0.013	0.17	0.0026	0.27	0.0094
	0.48	2.6	0.012	0.73	0.0035	0.29	0.0025
	0.73	3.5	0.035	0.89	0.0042	0.25	0.0037
Pum	0	0.52	0.015	0.13	0.0022	0.25	0.011
	0.40	2.0	0.096	0.47	0.0093	0.23	0.0066
	0.71	3.1	0.033	0.59	0.0090	0.19	0.0024

Table 6. RMSE and bias of thermal property functions in various testing media.

C778	Wed	Sod	Ang	Alu	Coa	Gar	Pro	Pum
C_v – mixing model								
0.13	0.18	0.17	0.11	0.15	0.14	0.29	0.12	0.19
λ – mixing model								
0.30	0.36	0.13	0.34	0.29	0.095	0.25	0.10	0.12
λ – Campbell (1985) model								
0.043	0.057	0.032	0.029	0.12	0.040	0.039	0.022	0.015
λ – Chung and Horton (1987) model								
0.043	0.057	0.022	0.029	0.12	0.040	0.039	0.022	0.015
λ – Lu and Dong (2015) model								
0.043	0.057	0.0092	0.029	0.12	0.052	0.043	0.022	0.066
λ – Ghanbarian and Daigle (2016) model								
0.073	0.057	0.0092	0.029	0.14	0.040	0.039	0.022	0.031

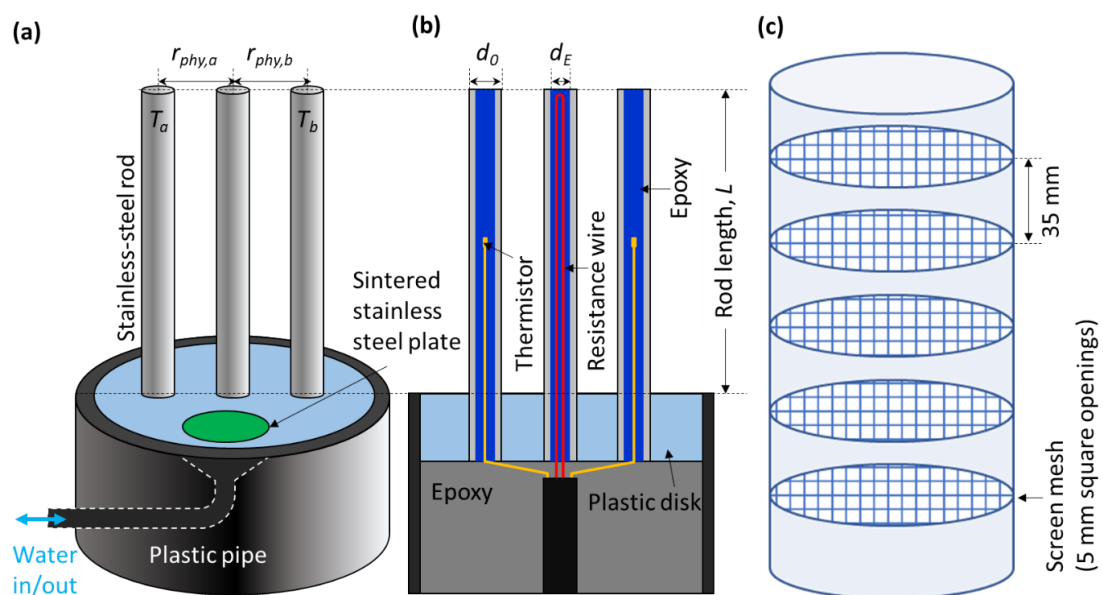


Fig. 1. (a) A pictorial drawing of THPP, (b) cross-section of THPP and (c) a pictorial drawing of a layered screen column.

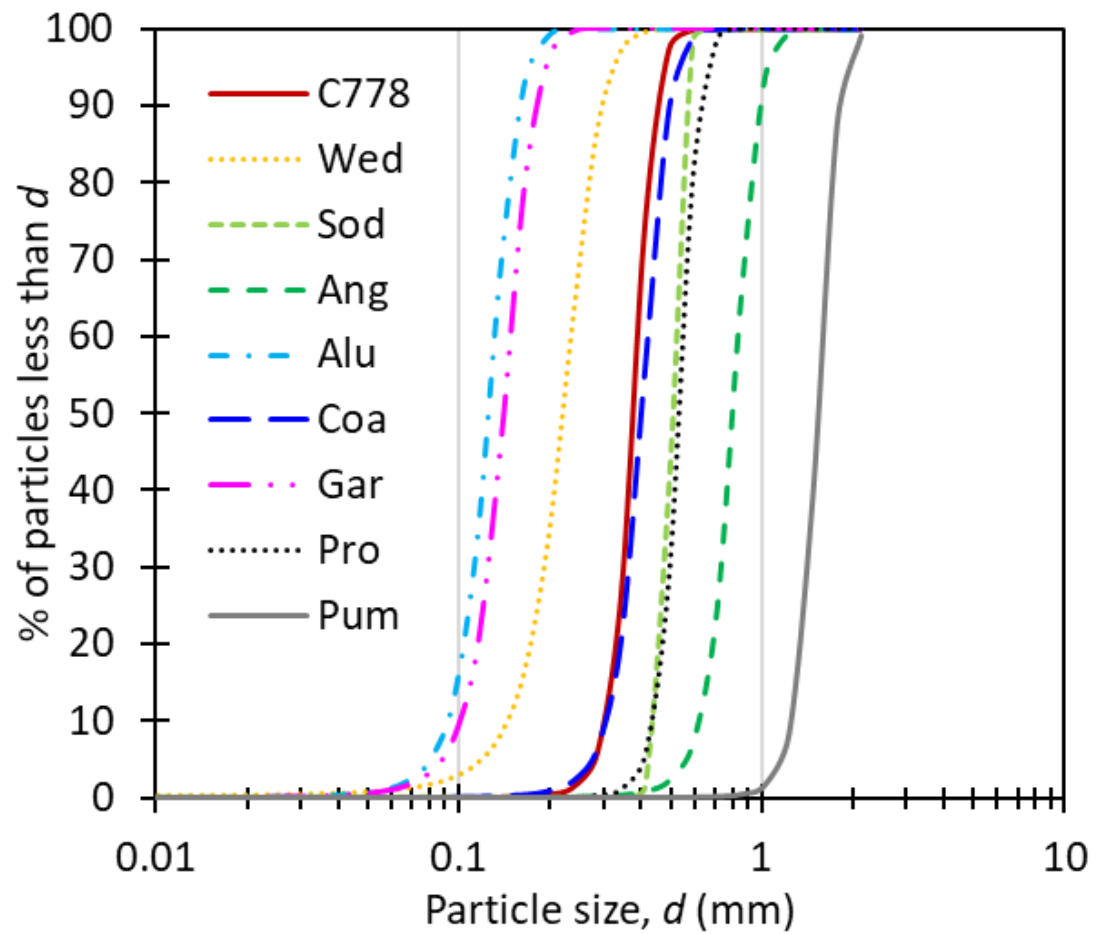


Fig. 2 Particle size distribution of coarse granular media based on the parameters shown in Table 3. **Error! Reference source not found..**

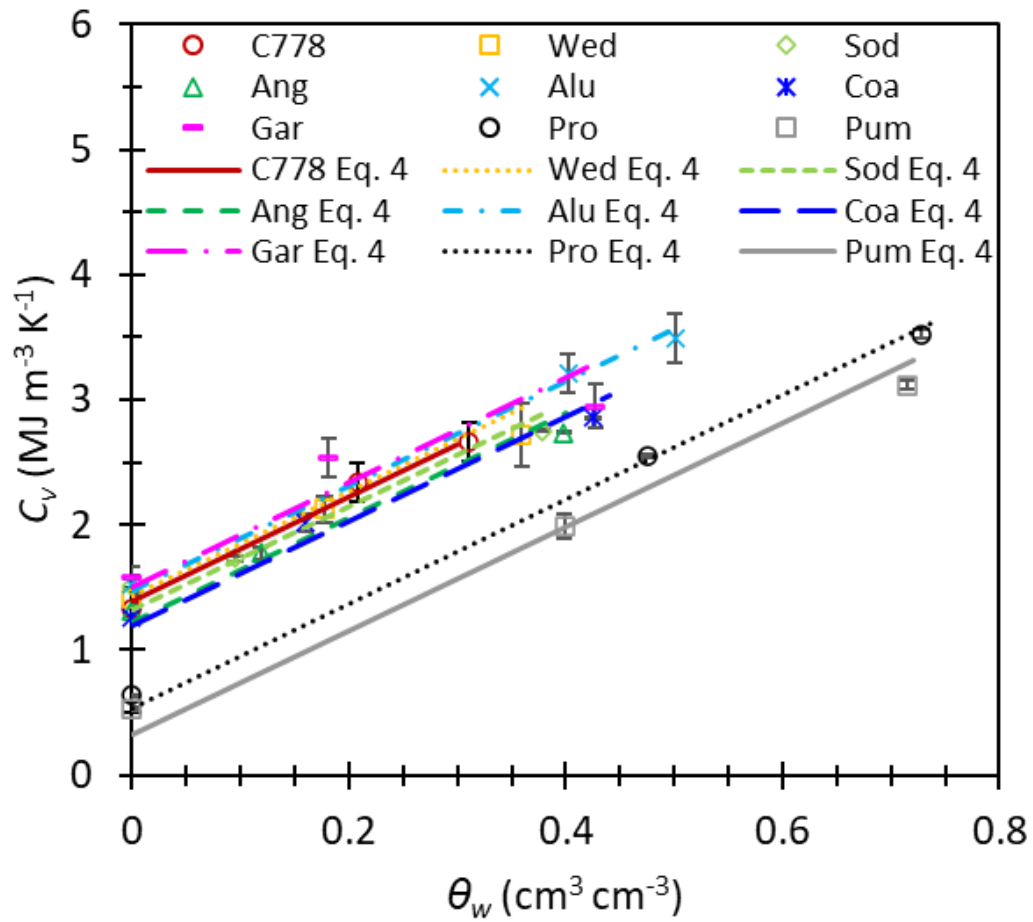


Fig. 3 The volumetric heat capacity (C_v) function of water content determined by THPP (symbols) and the mixing model (lines) using the fitted parameter shown in Table 4. The standard deviation of estimated C_v by THPP measurements was shown as solid black bars.

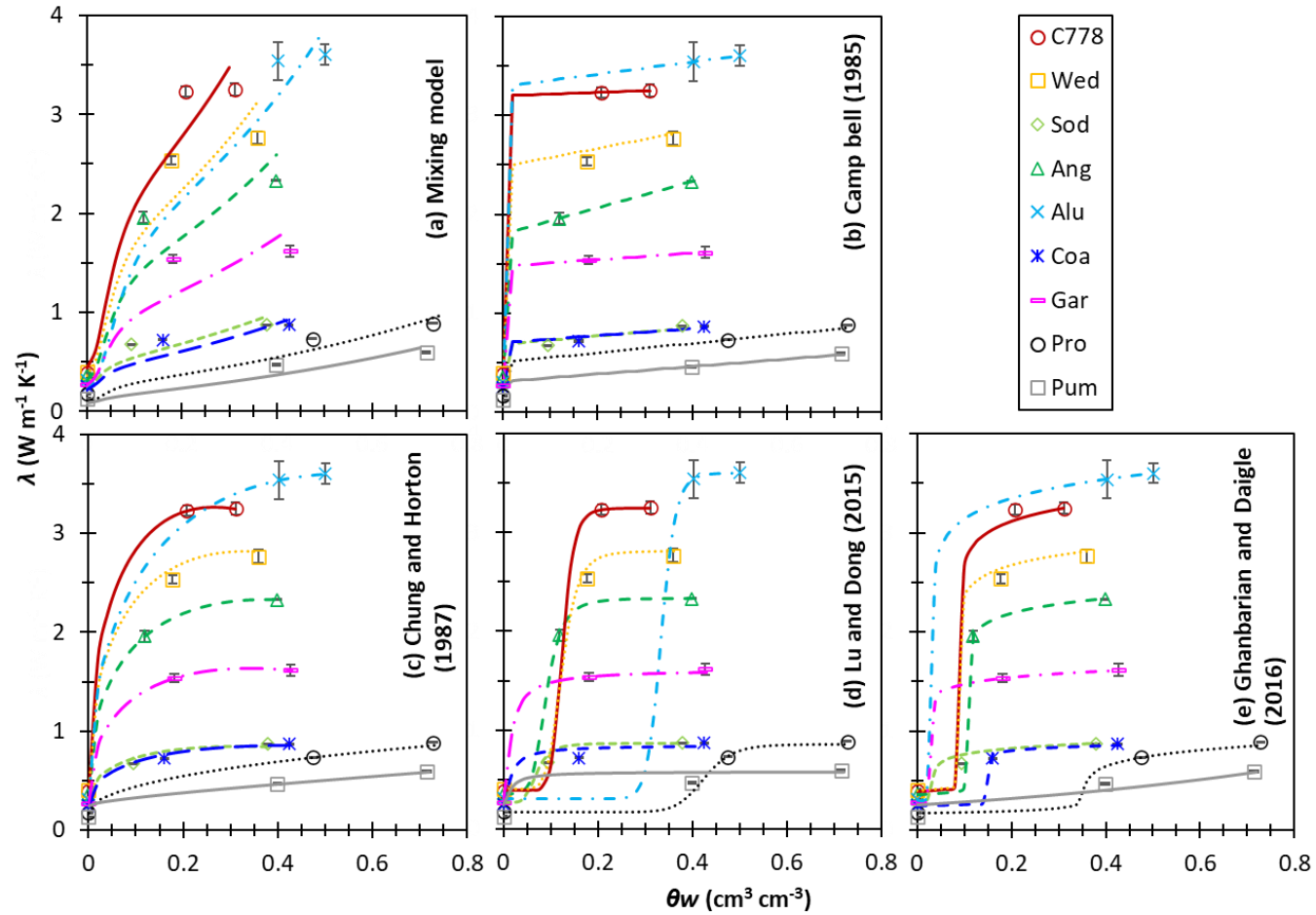


Fig. 4. The average λ functions determined by THPP (symbols) with the black bar representing the standard deviation. The fitted λ models, (a) the mixing model, (b) Campbell (1985) model, (c) Chung and Horton (1987) model, (d) Lu and Dong (2015) model and (e) Ghanbarian and Daigle (2016) model using the fitted parameter values shown in Table 5 are exhibited as lines.

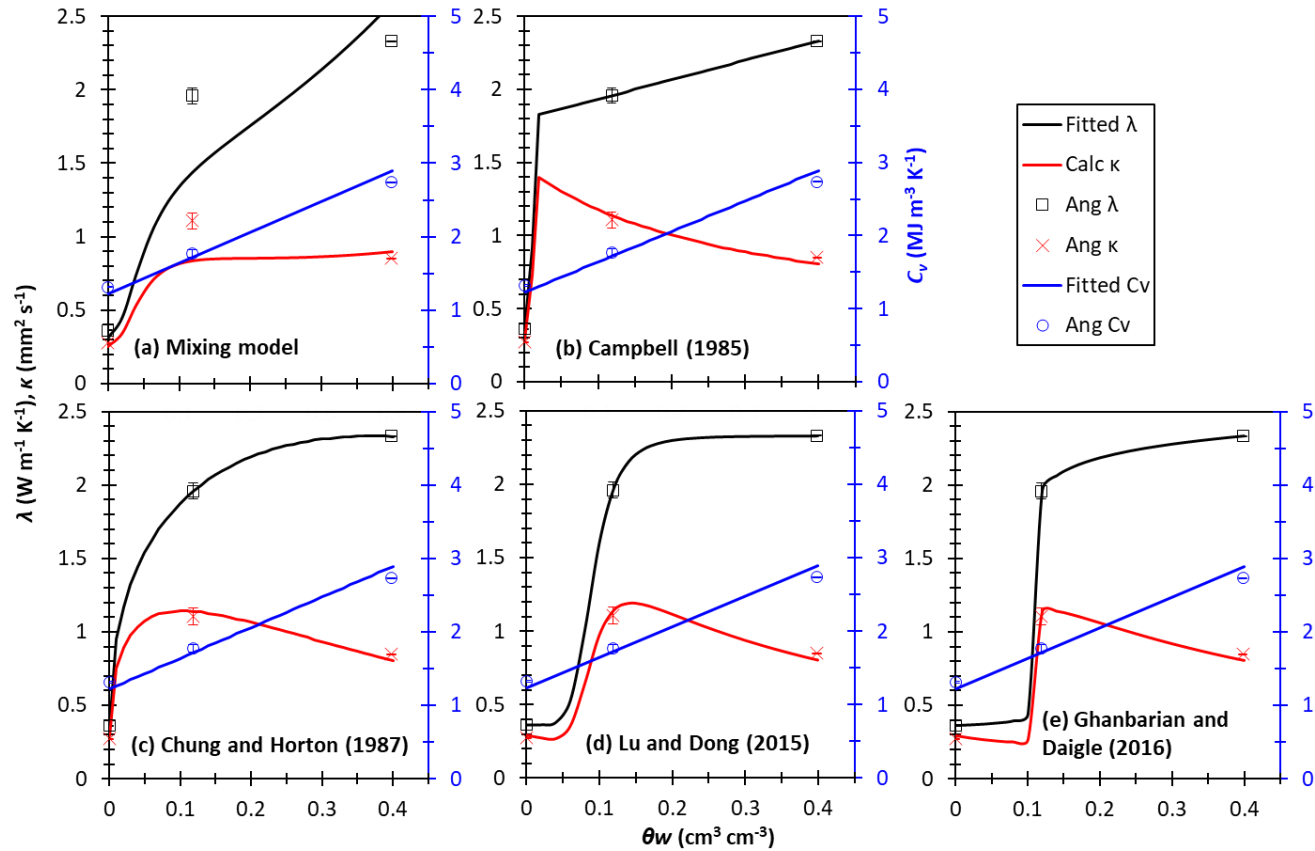


Fig. 5 Volumetric heat capacity (C_v) and thermal- conductivity (λ) from THPP estimations as well as resulting computed thermal diffusivity ($\kappa = \lambda/C_v$) in coarse angular sand (symbols). The blue line represents the optimized mixing model of C_v and each black lines represents λ models using (a) mixing model, (b) Campbell (1985), (c) Chung and Horton (1987), (d) Lu and Dong (2015) and (e) Ghanbarian and Daigle (2016) model. The red line illustrates the computed κ using the C_v mixing model and optimized λ model.

CHAPTER IV

AUTOMATED HANGING WATER COLUMN FOR CHARACTERIZING WATER
RETENTION AND HYSTERESIS OF COARSE-TEXTURED POROUS MEDIA

ABSTRACT

Modeling and characterizing hysteretic water retention is critical for predicting hydrodynamic behavior in porous media. This is especially true in coarse-textured media used in geotechnical engineering-, greenhouse- and landscape-industries, where subtle changes in water status may lead to plant stress. However, based on the traditional hanging water column method, water retention measurements are laborious and time-consuming because of the stepwise manual water potential adjustments and wait-time requirements for equilibrium conditions to develop. Therefore, we designed and fabricated an automated system to collect wetting- and drying-water retention data from coarse porous media. The basic system consisted of 1) a compound pressure transducer (± 70 cm range) providing both the porous medium's volumetric water content (θ) and matric potential (h) determinations, 2) a 70 cm linear actuator to vertically position a 50 ml burette, and 3) a diffuse laser distance sensor positioned by a 10 cm linear actuator to monitor the burette's vertical position relative to the sample position. This automated system determined the initial drying process beginning with a fully saturated sample ($h = 0$ cm) and determined subsequent wetting- and drying-water retention curves. Our automated water retention measurements in quartz sand (ASTM-C778) exhibited maximum- and minimum-standard deviation in θ of 0.013 and $0.00044 \text{ cm}^3 \text{ cm}^{-3}$, respectively. Parameters of the hysteretic

water retention model of quartz sand were characterized using repeated measurements. Results of this research included the creation of an automated water retention system and the well-characterized hydraulic parameters for the original well-graded- and narrowly sieved particle sizes of quartz sand.

1. INTRODUCTION

The porous medium's water retention relates a material's (i.e., soil) hydraulic energy state or matric potential (h) in saturated and unsaturated conditions with its volumetric water content (θ). This relationship depends on the pore size distribution of the porous medium and the properties of air, water and solid interfaces (Hillel, 1998). Water retention plays essential roles in soil-physics, -biology, -chemistry and beyond, and it is used for simulating the fundamental mass and transport of water, solute and gas through porous media. In addition, understanding the water retention character of porous media is critical for understanding processes, including evapotranspiration, surface energy balance, plant growth and microbial activities for both in-situ field- and laboratory-experiments. An important concept of water retention is hysteresis, defined by the Glossary of the SSSA Terms as "*A nonunique relationship between two variables, wherein the curves depend on the sequences or starting point used to observe the variables. Examples include the relationships (i) between soil-water content and soil-water matric potential, ...*". Pham et al. (2005) thoroughly reviewed the hysteretic character of water retention. The mechanisms of hysteretic water retention character have been identified as 1) the "ink bottle" effect, 2) different liquid-solid contact angles for advancing/receding water menisci, 3) air-entrapment within the porous media, 4) swelling and shrinking of the media, creating different pathways of water held in the pore structure during the drying- and wetting-

processes (Philip, 1964; Poulouvassilis, 1970; Stonestrom and Rubin, 1989; Lehmann et al., 1998; Likos et al., 2004). The hysteretic water retention consists of a) the initial (or primary) drying process, b) the main (or secondary) drying- and wetting-processes and c) potential intermediate scanning branches. The initial drying process starts with theoretical complete saturation, followed by the drying process to an arbitrary lower h condition. The wetting process is then facilitated by the existing hydraulic connection from the initial drying process and refills the air-filled pore space as h approaches zero (saturation). The main drying process may start from the same θ value as the initial drying at saturation (a complete hysteresis loop), however, the media likely entrains air during the wetting process, leading to a reduced 'saturated θ ' value (Haines, 1930). When the main drying (or wetting) process is reversed abruptly before completing its process from the saturation to residual θ condition, the water retention diverges to follow a wetting (or drying) scanning process, which generally scales between the main drying- and wetting-water retention curves. These effects of hysteresis on water retention behavior have been recognized as critical for accurately modeling hydrodynamics in all types of porous media, which relates to infiltration, solute transport and multiphase flow (Kool and Parker, 1987; Parker and Lenhard, 1987).

The water retention is characterized by pairing correlated θ and h measurements at the hydraulic equilibration state during both the drying- and wetting-processes (Dane and Hopmans, 2018). For example, Haines (1930) demonstrated the hanging water column, which uses a fritted Buchner funnel connected to a burette via water-filled tubing to create a hydraulic connection between the burette and the funnel. The system induces a suction (negative potential, h) at the base of the test sample on the funnel's frit, as the burette is

incrementally lowered in small steps relative to the sample position. After the water in the burette reaches equilibrium, the water level is used to compute the test media's θ and h values. Various steady-state measurements have been demonstrated for characterizing water retention with an h range limited by the method chosen. These include hanging water columns ($h > -2$ m), pressure cells ($h > -8.5$ m) and pressure plate systems ($-5 > h > -150$ m) (Dane and Hopmans, 2018). The measurement time is highly variable in each method, and a longer equilibration time is required as h becomes smaller (i.e., more negative). However, there is no single method to characterize a continuous water retention process across the full range of h (Assouline, 2021).

Ongoing advances in technology have allowed us to reduce human-error and -labor by automating systems. Automations range from simple data collection to integrated analysis, such as image recognition and machine learning. Raeesi et al. (2014) demonstrated an automated multistep inflow-outflow apparatus to provide hysteretic water retention measurements for consolidated porous media. Our objective was to demonstrate repeatable hysteretic water retention measurements in quartz sand using our developed automated hanging water column system.

2. THEORETICAL

2.1 Water Retention Model

The widely used continuous water retention model developed by van Genuchten (1980) (hereafter the VG model) is expressed as:

$$\theta = \theta_r + (\theta_s - \theta_r)[1 + (\alpha|h|)^n]^{-m} \quad (1)$$

where θ_r and θ_s are the residual- and saturated-water content ($\text{cm}^3 \text{cm}^{-3}$), respectively, and the parameter α (cm^{-1}) affects the curve shape and is commonly considered equivalent to

the reciprocal of the air-entry potential of the porous medium. Coarse-textured materials are typically characterized by a low air-entry value, leading to a greater value of α . Two other curve shape parameters, m and n , are related to the pore size distribution, and m is often written in terms of n as $m = 1 - 1/n$. Porous media with a narrow particle size distribution also exhibit drainage/absorption over a commensurately narrow h range. This step-like water retention model is characteristic of larger values of n . The hysteretic nature of water retention in porous media can be characterized using Equation (1) with superscripted parameters where the superscripts $d0$, d and w represent the initial drying, the main drying and the main wetting processes, respectively. For example, θ_r^{d0} , θ_s^{d0} , α^{d0} , n^{d0} represent the initial drying parameters, and θ_r^d , θ_s^d , α^d , n^d and θ_r^w , θ_s^w , α^w , n^w represent the main drying and the main wetting parameters, respectively.

3. MATERIALS AND METHODS

3.1 Automated Hanging Water Column Measurements

FIGURE 1a presents the automated water retention measurement system, which primarily consists of 1) a custom-configured compound ± 1 psi (± 70 cm w.c.; ± 5 vdc output) pressure transducer (Item Number: MMCG001BIV5P3A2T1A1; Omega Engineering Inc., Norwalk, CT), 2) a diffuse laser (OPT2011, Wenglor, Munich, Germany) mounted on a 10 cm linear actuator (10 cm stroke-linear stage actuator, Twowin, Amazon.com; Sfu1402 Nema17 Stepper Motor), 3) a 50 ml burette (Pyrex # 2124, Corning Inc., Glendale AZ) attached to a 70 cm linear actuator (Liukouuu8ty26hzdc-05; Liukouu, Amazon.com; 12 vdc; 1500 N load; stroke 20–75 cm), 4) a 350 ml fritted Buchner funnel (Pyrex #36060, Corning Inc., Glendale AZ) and 5) a 2" T-slot-based outer aluminum frame, which secured the position of the various components as well as the control panel.

The panel contained a datalogger (CR1000, Campbell Scientific Inc., Logan UT), a relay driver (A6REL-12, Campbell Scientific Inc., Logan UT) and three DC power supplies of 12-, 24-, and 28-VDC. FIGURE 1b shows the enlarged view for the water retention measurement system showing the porous media (1 cm height) placed in the Buchner funnel (i.d. 7.5 cm) with a 10–15 μm fritted porous disk with a hydraulic connection through tubing to the burette and the pressure transducer. The pressure transducer provided a 0.056 cm resolution of the h value measured at the porous medium sample base. The 70 cm linear actuator at the left side of the aluminum frame in FIGURE 1a moved the 50 ml burette up/down to induce a positive/negative h gradient within the porous media based on the adjusted vertical position between the varied water level in the burette (z_b) and the sample base (reference, z_0). The 10 cm linear actuator mounted at the top of the frame moved the diffuse laser sensor horizontally. The laser sensor provided a 0.1 cm resolution of two vertical distance measurements from the laser to z_0 and z_b , respectively. The horizontal movement using the 10 cm linear actuator was calibrated and programmed in the CR-Basic language of the datalogger, to estimate these two vertical positions. These vertical distance measurements were used to validate the positioning of system components as well as to calculate the volume of outflow water in the burette ($V_{out} = 0.88 \times (h - z_b - z_0)$), where 0.88 was the calibration coefficient to convert the height in the burette into the volume via the internal cross-sectional area. The computed V_{out} value was used to calculate the change of θ in the test media. The combination of the compound pressure transducer and the diffuse laser distance sensor provided a water estimate resolution of ± 0.13 ml for the V_{out} , which corresponded to a resolution of ± 0.0021 cm^3 cm^{-3} for detecting subtle changes in the sample's θ .

3.2 Automated Measurement Protocol

The automated system was controlled by a CR-Basic program written using LoggerNet software (Campbell Scientific Inc., Logan UT), and that program is provided in the supplemental material section. FIGURE 2 lays out and describes the program and function of the automated system. The system started by measuring the initial drying process within a completely saturated sample, where the sample base's h value was near zero. The h value was monitored using the pressure transducer every second to compute the moving average of h (h_{ave}), which was used to determine the equilibrium state. When the h_{ave} value was maintained within the resolution of the pressure transducer, i.e., 0.056 cm, for 5 minutes, the program concluded that the sample reached the target equilibrium condition. The 10 cm linear actuator mounted at the top of the frame then moved the diffuse laser distance sensor horizontally to measure the two vertical positions of the sample reference and the burette, z_0 and z_b , respectively. The new sample θ value was computed using V_{out} with measured h , z_0 and z_b ($V_{out} = 0.88 \times (h - z_b - z_0)$) and subtracted from the initial estimate of the saturated water content (θ_{mi} , in this case, $0.4 \text{ cm}^3 \text{ cm}^{-3}$) for the first set of measurements. The computed sample θ was used for the next θ calculation at the new h . This cyclical process described the measurements involved in the automated system that recorded pairs of h and θ , leading to the water retention data during both the drying- and wetting-processes. The automated system repeated the main measurements under the drying process by moving the burette's vertical position downward with the 70 cm linear actuator to decrease h stepwise. The increment of the burette's repositioning was initially set as 5 cm for the drying- and wetting-processes. Note that the 5 cm change in the burette's vertical position generally resulted in a smaller change in the internal water column height

(Δh) due to in/out flows from/to the sample. However, the increment value can be manually adjusted in the program. This process was repeated until the burette position reached the maximum of 70 cm (maximum length of the 70 cm linear actuator), or the change of recorded θ was negligibly small ($\Delta\theta < 0.005$) within any three consecutive measurement sets. If $\Delta\theta < 0.005 \text{ cm}^3 \text{ cm}^{-3}$ in three consecutive measurements (total h change of -15 cm), the program diagnosed the sample θ reached the residual water content condition, and the drying process was switched from the drying process to the wetting process before reaching to the maximum burette position of 70 cm. The wetting process of water retention data measurements followed the same procedure described, except the measurements started from the driest condition (the lowest burette level) to near-saturation (the initial burette level). The V_{out} was again used to calculate θ as h values became less negative. These drying and wetting cycles were triplicated with an additional drying process to stop the system at the lowest burette level. After completing the final drying cycle, the sample was removed from the Buchner funnel to compute the final θ by oven-drying at 105°C for 24 hours. All θ values were then corrected based on the oven-dried θ value.

3.3 System Cleaning

Our automated measurement system was programmed to conduct the hysteretic water retention with incremental changes in h using a minimum resolution of 1 cm and to provide repeated measurements. When water flow in the system was substantially reduced, i.e., to less than 0.01 cm min^{-1} for 5 minutes or more in our system, the automated control algorithm assumed the equilibration condition had been reached. Biofilm caused by bacteria/algae growth in water-based systems may lead to reduced flows, which was reported by Eching and Hopmans (1993). Biofilm build-up in water tubes, the Buchner

funnel's fritted disk and test media, could lead to erroneous determination of the equilibrium condition based on these criteria, especially when measurement cycles result in lengthy experiments. Hydrogen peroxide is the most common reagent for removing organic matter and biofilm (Mickelson et al., 1989; Christensen et al., 2009). After removing the test media from the Buchner funnel, the ceramic plate in the funnel and tubing connected to the burette were thoroughly cleaned with 30% hydrogen peroxide and distilled water.

3.4 Media Preparation

Coarse-textured quartz sand (C778 ASTM graded silica sand, US Silica, Ottawa, IL, USA) was selected as a well-characterized ("ASTM C778-21, Standard Specification for Standard Sand," 2021) and readily available granular porous media. This graded sand exhibits uniform spherical-shaped grains and adheres to the specified particle size distribution ranging from 150- to 1180- μm . The detailed cumulative particle size distribution of the graded sand characterized by Dixon et al. (2023) is compared to the manufacturer-provided data (US Silica, 2021) in FIGURE 3. The fine-incremented sieve determinations by Dixon et al. (2023) are highly correlated to the manufacturer-provided particle size distribution (US Silica, 2021). The original graded sand along with narrow sieved fractions separated at 850-, 710-, 600-, 500-, 425-, 355-, 250- and 212- μm were used in our study. We did not use particles greater than 850 μm and smaller than 212 μm due to the lack of sample volume ($> 60 \text{ cm}^3$) collected from these sieve sizes for measurements. TABLE 1 lists the particle size range, the difference between the minimum and maximum particle size, particle density (ρ_s), bulk density (ρ_b) and computed porosity ($\phi = 1 - \rho_b/\rho_s$) values in each test media determined prior to water retention measurements.

The ρ_s of quartz sand was determined using the water displacement method (Dane and Topp, 2002). Each sample tested was packed into a 200 ml column (i.d. = 7.4 cm) using the multiple sieving pluviation (MSP) method described in Dixon et al. (2023) in order to determine packing ρ_b , with results presented in TABLE 1. The MSP method used a five-layer screen column with square opening sizes of 1×1 cm. A funnel (opening diameter of 0.5 cm) was mounted above the top screen within the column, to aid in pouring sand and to maintain a consistent input of sand to ensure random scattering at the base of the screen column. The MSP method provided highly reproducible ρ_b values for the granular media shown in TABLE 1 (Miura and Toki, 1982; Dixon et al., 2023).

A 1 cm depth of each test media sample was packed into the Buchner funnel using the MSP method, resulting in "assumed ρ_b values" presented in TABLE 1. The Buchner funnel was in hydrological contact with the 50 ml burette filled with water during the sample preparation, which increased the θ value of the sample by wicking the bulk water while packing. After packing, water was slowly injected from the three-way valve attached to the tubing to saturate the test media in the Buchner funnel for at least 24 hours to ensure complete saturation. After 24 hours of saturation, the excess water was removed from the three-way valve, and the $h = 0$ cm condition at the bottom was maintained before initiating the automated measurements.

3.5 Data Correction on Water Retention Curve Measurements

Although the Buchner funnel containing the test sample was covered by parafilm to minimize surface evaporation during measurements, ignoring water losses may create a bias in measured h and computed θ values, leading to altered hysteretic water retention character. During measurements, we observed a linear decrease in the maximum water

drainage volume in the burette at the lowest h setting, resulting from minor evaporative water losses from the media's surface and tubing surfaces (Dane and Hopmans, 2018). The actual water loss by evaporation from the sand surface was assumed to be at a constant rate, and it was determined by comparing the initial drainage volume from the test media and subsequent drained volume in each cycle. The θ values were then reconciled by accounting for the estimated temporal water loss through evaporation.

As mentioned earlier, hanging water column measurements assume the sample is at hydrostatic equilibrium when collecting the pair of h and θ , where both h and θ represent the average property within the sample profile. However, correction is recommended when the sample's maximum pore size and sample height exceed critical thresholds (Jalbert and Dane, 2001). The sample's non-uniform water content distribution can induce bias in estimating the sample's water retention character as sample height increases. We evaluated if there was a need for sample height correction based on criteria outlined in Jalbert and Dane (2001), which computes a critical pore radius at a known sample height as a necessary correction. The computed critical pore radius for a sample with a 1 cm height was determined to be 3 mm (3000 μm). With a maximum particle diameter for our largest sand sample (TABLE 1) of 1180 μm (approximating pore size between 0.33 and 0.25 of the particle size), no correction is needed for any of our samples based on the critical pore radius and 1 cm height criteria.

3.6 Hydraulic Parameter Fitting

The VG model parameters, θ_r and θ_s (Equation (1)), which represent the residual- and saturated- θ values, respectively, were computed as the average value of repeated automated measurements during the main drying- and main wetting-processes. Since the

initial drying process did not have repeated data, a single set of θ_r and θ_s values was used. The other two water retention parameters, α and n ($m = 1-1/n$) in the initial drying-, main drying- and main wetting-processes, were optimized using the measured θ_r and θ_s values. The parameter optimization for α and n was conducted by minimizing the objective function (OF) as follows;

$$OF = \sum[\theta_m - \theta]^2 \quad (2)$$

where θ_m is the volumetric water content during the automated measurements, and θ is the computed volumetric water content using Equation (1).

4. RESULTS AND DISCUSSION

4.1 Hysteretic Water Retention Measurements

TABLE 1 presents the particle size range, ρ_s , ρ_b , and the computed φ ($= 1 - \rho_b/\rho_s$) of the graded sand and other particle size ranges. The MSP method yielded ρ_b values of 1.85 ± 0.0054 g cm⁻³ in the graded sand while values for the sieved media expressed generally decreasing values from 1.89 to 1.79 g cm⁻³, moving from the coarser particles (20/25, 710–850 μm) to the finer particle sizes (60/70, 212–250 μm). Potential reasons for this decreasing trend may arise from the overall complexity of particle packing in addition to a reduction in kinetic energy of the air-pluviation packing method as particle size decreases (Vaid and Negussey, 1984). There is also an impact of generally reducing particle size range for smaller size classes, e.g., 140 μm for 20/25 vs. 38 μm for 60/70.

FIGURE 4 shows hysteretic water retention measurements from three individual graded sand (graded sand (1), graded sand (2) and graded sand (3)), each including an initial drying-, five repeated drying- and five repeated wetting-processes. Squares and circles represent drying- and wetting-measurements with the label graded sand (1),

respectively, and black crosses represent graded sand (2) and gray triangles for graded sand (3). The numbers on the labels in graded sand (1) represent the repetitions of the drying- and wetting-processes. We highlighted the water retention measurements migration as the drying- and wetting- processes repeated. For example, the measurements initiated from the drying process and the label d0 (red squares) represent the initial drying measurements. The automated system then switched from drying to wetting, and the label, w1 (yellow circles), represents the first wetting measurements. Different colored symbols represent half cycles of repeated water retention measurements from the six drying- and five wetting-processes. The initial drying process (d0) exhibited the highest θ at saturation, while repeated drying measurements (d1, d2, ... and d5) exhibited lower 'saturated' θ because the re-wetting process entrained air into the wetting media. Air entrainment is a common phenomenon during hysteretic water retention measurements (Pham et al., 2005). As the drying- and wetting- processes repeated, part of the water initially filling the media's porosity was replaced with entrained air, and the excess water remained in the 50 ml burette, leading to a slightly positive potential at the bottom of the sample at saturation. The average hourly system evaporation loss was estimated at $0.015 \text{ cm}^3 \text{ h}^{-1}$, equivalent to the reduction in θ of $0.00025 \text{ cm}^3 \text{ cm}^{-3} \text{ h}^{-1}$. The initial drying measurements exhibited substantially greater θ in both saturated and unsaturated conditions compared to the θ values from each repeated drying measurement within an h range from -30 to 0 cm, while θ values from the initial drying measurements merged with θ values of the repeated drying measurements for $h < -30$ cm. All three datasets of water retention measurements (graded sand (1), graded sand (2) and graded sand (3)) in FIGURE 4 include an initial drying cycle from saturation and five repetitions of drying and wetting processes that do not reach

saturation due to air entrapment during the re-wetting cycles. All three datasets presented small variations in θ at the wet end ($h > -14$ cm) and at the dry end ($h < -35$ cm) while exhibiting greater fluctuations in between, around $h = -20$ cm, which corresponded to the approximate peak value of the water retention curve's slope ($d\theta/dh$). For example, graded sand (1), graded sand (2) and graded sand (3) exhibited the largest standard deviation values in θ of 0.013, 0.0084 and 0.0062 $\text{cm}^3 \text{cm}^{-3}$ at h values between -16 and -19 cm, respectively, while the smallest standard deviation values in θ of 0.0010, 0.0014 and 0.00044 $\text{cm}^3 \text{cm}^{-3}$ occurred at h values between -41 and -42 cm, respectively. Repeated drying- and wetting-measurements in graded sand (3) in FIGURE 4 exhibited the most stable main drying- and wetting-water retention, yielding standard deviations of 0.00044 and 0.0062 $\text{cm}^3 \text{cm}^{-3}$, respectively. The repeated wetting water retention measurements showed less fluctuation in θ than the repeated drying measurements. The repeated drying water retention measurements in graded sand (1) showed a gradual decrease in the apparent θ_s value from 0.28 to 0.27 $\text{cm}^3 \text{cm}^{-3}$ and a more substantial decrease in the θ value under unsaturated conditions. For example, repeated drying measurements from d1 (yellow squares) to d5 (blue squares) showed the largest decrease in θ from 0.20 to 0.18 $\text{cm}^3 \text{cm}^{-3}$ at around an h value of -19 cm. A minor gradual decrease in θ was also observed in graded sand (2) and graded sand (3). On the other hand, the repeated wetting water retention measurements showed almost stable water retention with a slight increase in θ . This θ migration led to a shift in the water retention measured data, especially in the main drying process.

We observed increasingly elongated measurement times to complete each drying and wetting cycle. This was likely due to gradual pore-clogging in the porous plate,

reducing water flow. Pore-clogging was easily cleaned with a hydrogen peroxide solution; however, we did not find an effective way to prevent the porous plate from clogging while conducting the measurements. The automated measurements required about 10 hours to complete one measurement cycle of the drying- and wetting-process. The time required to obtain a pair of θ and h was related to the measurement increment of h to create the pressure gradient at the bottom of the media and the media's water retention and hydraulic conductivity, which were critically related to the particle size distribution and its range. For example, all media showed a peak time at the intermediate θ condition during the drying- and wetting-processes where the water retention curve shape showed a drastic change (greater $d\theta/dh$), inducing a greater water volume change in the test media. This demonstration of the automated hanging water column measurement system used coarse-textured sand with an h range between $-50 < h < 0$ cm. We acknowledge that it is possible to extend the h range below -50 cm using a longer linear actuator, however, the compound pressure transducer may require a commensurate pressure range increase and a finer pore-sized fritted plate in the Buchner funnel, ultimately leading to slower response times at the dry end. Application of finer textured media with lower hydraulic conductivity would also be possible, however, an extended measurement time requirement is expected, and the finer particles could induce pore clogging of the fritted plate, further extending the measurement time.

4.2 Hysteretic Water Retention Parameters

FIGURE 5 shows the optimized water retention curves using the VG model (Equation (1)) of the eight quartz sand size classes described in TABLE 1. The initial drying, main drying and main wetting process are presented as dotted-, solid- and dashed-

lines, respectively. The cross-, square- and circle-symbols represent automated measurements of initial drying-, the average of repeated drying-, and the average of repeated wetting-processes, respectively. Bars in the symbols represent the standard deviation values from triplicated measurements. The graded sand (FIGURE 5a) and coarser-textured sand such as 20/25 (FIGURE 5b), 25/30 (FIGURE 5c), 30/35 (FIGURE 5d), and 35/40 (FIGURE 5e) exhibited distinct initial drying (black dotted line), which showed substantially greater θ values in a relatively wet condition compared to the main drying process (solid red line). Although the VG model describes an almost constant θ value from saturation to the air-entry value, all media in the initial drying-, main drying- and main wetting-processes showed a gradual decrease in θ from saturation to the air-entry value. Therefore, modeled θ values were overestimated near the saturation condition.

TABLE 2 lists all fitted VG model parameters, including θ_r , θ_s , α and n , describing the initial drying (d_0)-, main drying (d)- and main wetting (w)-processes. The θ_r and θ_s values ranged from 0.012 to 0.064 and between 0.26 to 0.35 cm³ cm⁻³, respectively. We note that θ_r and θ_s parameters demonstrated sensitivity to the value of ρ_b , where lower ρ_b values in finer particles (TABLE 1) yielded greater θ_r and θ_s values. Values of $\theta_s^{d_0}$ in most samples were greater than θ_s^d and θ_s^w . Although θ_s values were similar to the computed ϕ values in TABLE 1, media with finer particle size (e.g., 45/60) presented greater values of θ_s than of the value of ϕ . The parameter α exhibited a range from 0.031 to 0.18 cm⁻¹, which is correlated to the air-entry value and the particle size range and its distribution. Samples with a finer particle size exhibited smaller α values due to smaller pore sizes, leading to more negative air-entry pressures. The parameter n , which is correlated to the slope of the water retention curve, i.e., resulting from particle size distribution, exhibited a range of

values from 3.0 to 13. Values of n for the drying process were slightly greater than for the wetting processes

We compared our optimized parameters listed in TABLE 2 with reported parameters (θ_r , θ_s , α and n) of spherical quartz sand (Accusand, Unimin Corporation, Le Sueur, MN) reported by Schroth et al. (1996), and reproduced here in TABLE 3. Their work included determining the sand's drying water retention with somewhat broader sieve (particle) size ranges of 12/20 (850–1700 μm), 20/30 (600–850 μm), 30/40 (425–600 μm) and 40/50 (300–425 μm). The θ_r values were smaller and with a narrower range between 0.012 and 0.02 $\text{cm}^3 \text{cm}^{-3}$, while all media exhibited θ_s value of 0.35 $\text{cm}^3 \text{cm}^{-3}$, which was equal to the maximum value of our optimized θ_s value. Although Schroth et al. (1996) also applied a packing method similar to the MSP method we used, their ρ_b values may have been smaller than our ρ_b values, inducing greater θ_s values. Their α values exhibited a narrower range from 0.045 to 0.15 cm^{-1} , compared to our optimized values, while their n values ranged from 7.4 to 13, slightly greater than our optimized n values. Our work also extended the hysteretic water retention model parameterization and included a wider particle size range.

5. CONCLUSIONS

We designed, fabricated and demonstrated an automated hanging water column measurement system driven by our need for more accurate and efficient retention data collection. The system consists of a compound pressure transducer and provides both porous medium matric potential (h) and volumetric water content (θ) determinations in combination with a 50 ml burette. A 70 cm linear actuator was used to position the burette and a diffuse laser distance sensor, positioned by a 10 cm horizontal linear actuator,

facilitated monitoring of the burette's vertical position relative to the sample reference elevation. Beginning with a fully saturated sample ($h = 0$ cm), the automated system determined the initial drying water retention data and the subsequent wetting- and drying-water retention measurements within a minimum h of -50 cm. The repeated drying- and wetting-processes of water retention measurements were critical to characterizing hysteretic water retention behavior, such as the initial drying-, main drying- and main wetting-processes. The automated measurements using ASTM-graded sand provided an initial drying process and five repeated main drying- and wetting-data sets with the largest standard deviation of $0.013 \text{ cm}^3 \text{ cm}^{-3}$ in θ at an h value of -19 cm and the minimum standard deviation value of $0.00044 \text{ cm}^3 \text{ cm}^{-3}$ in θ at the dry end ($h = -41$ cm). However, in one of three data sets, we observed drifting θ values over the five repeated drying- and wetting-measurement cycles, leading to a shift in water retention data. Air entrapment in the test media usually resulted in a decrease in θ_s values for repeated measurement cycles. We also observed increasing times to complete automated measurement cycles, likely due to pore-clogging by bacterial growth. The graded sand was sieved into seven different particle size ranges and was used to obtain detailed water retention measurements for these size ranges. The van Genuchten (1980) water retention model parameters (θ_r , θ_s , α and n) were optimized and compared to values from earlier work by Schroth et al. (1996). Our automated hanging water column apparatus reduced manual labor requirements, expedited the measurement process and resulted in highly repeatable water retention data through as many as five wetting and drying cycles.

REFERENCES

Assouline, S. 2021. What Can we Learn from the Water Retention Characteristic of a Soil Regarding its Hydrological and Agricultural Functions? Review and Analysis of Actual Knowledge. *Water Resour. Res.* 57(12): e2021WR031026. doi: 10.1029/2021WR031026.

ASTM C778-21, Standard Specification for Standard Sand. 2021. ASTM International, in: *Annual Book of ASTM Standards*. Vol. 14.04.

Christensen, B.E., H.N. TrønneS, K. Vollan, O. Smidsrød, and R. Bakke. 2009. Biofilm removal by low concentrations of hydrogen peroxide. <http://dx.doi.org/10.1080/08927019009378142> 2(2): 165–175. doi: 10.1080/08927019009378142.

Dane, J.H., and J.W. Hopmans. 2018. 3.3.2 Laboratory. *Methods of Soil Analysis, Part 4: Physical Methods*: 675–720. doi: 10.2136/SSSABOOKSER5.4.C25.

Dane, J.H., and G.C. Topp. 2002. *Methods of Soil Analysis* (J.H. Dane and G. Clarke Topp, editors). Soil Science Society of America, Madison, WI, USA.

Dixon, C., W. Sheng, R. Zhou, R. Horton, and S.B. Jones. 2023. Thermal property standards using granular media with air-pluviation and heat pulse probe measurements. *Agric For Meteorol* 330: 109303. doi: 10.1016/J.AGRFORMET.2022.109303.

Eching, S.O., and J.W. Hopmans. 1993. Optimization of Hydraulic Functions from Transient Outflow and Soil Water Pressure Data. *Soil Science Society of America Journal* 57(5): 1167–1175. doi: 10.2136/SSSAJ1993.03615995005700050001X.

van Genuchten, M.Th. 1980. A Closed-form Equation for Predicting the Hydraulic Conductivity of Unsaturated Soils 1. *Soil Science Society of America Journal* 44(5): 892–

898. doi: 10.2136/sssaj1980.03615995004400050002x.

Haines, W.B. 1930. Studies in the physical properties of soil. V. The hysteresis effect in capillary properties, and the modes of moisture distribution associated therewith. *J Agric Sci* 20(1): 97–116. doi: 10.1017/S002185960008864X.

Hillel, D. 1998. *Environmental soil physics: Fundamentals, applications, and environmental considerations*. Elsevier.

Jalbert, M., and J.H. Dane. 2001. Correcting Laboratory Retention Curves for Hydrostatic Fluid Distributions. *Soil Sci. Soc. Am. J.* 65(3): 648–654. doi: 10.2136/SSSAJ2001.653648X.

Kool, J.B., and J.C. Parker. 1987. Development and evaluation of closed-form expressions for hysteretic soil hydraulic properties. *Water Resour Res* 23(1): 105–114. doi: 10.1029/WR023i001p00105.

Lehmann, P., F. Stauffer, C. Hinz, O. Dury, and H. Flühler. 1998. Effect of hysteresis on water flow in a sand column with a fluctuating capillary fringe. *J Contam Hydrol* 33(1–2): 81–100. doi: 10.1016/S0169-7722(98)00066-7.

Likos, W.J., M. Asce, and N. Lu. 2004. Hysteresis of Capillary Stress in Unsaturated Granular Soil. *J Eng Mech* 130(6): 646–655. doi: 10.1061/(ASCE)0733-9399(2004)130:6(646).

Mickelson, M., J.C. Converse, and E.J. Tyler. 1989. Hydrogen Peroxide Renovation of Clogged Wastewater Soil Absorption Systems in Sands. *Trans. ASAE* 32(5): 1662–1668. doi: 10.13031/2013.31206.

Miura, S., and S. Toki. 1982. A Sample Preparation Method and its Effect on Static and Cyclic Deformation-Strength Properties of Sand. *Soils Found.* 22(1): 61–77. doi:

10.3208/SANDF1972.22.61.

Parker, J.C., and R.J. Lenhard. 1987. A model for hysteretic constitutive relations governing multiphase flow: 1. Saturation-pressure relations. *Water Resour Res* 23(12): 2187–2196. doi: 10.1029/WR023I012P02187.

Pham, H.Q., D.G. Fredlund, and S.L. Barbour. 2005. A study of hysteresis models for soil-water characteristic curves. <https://doi.org/10.1139/t05-071> 42(6): 1548–1568. doi: 10.1139/T05-071.

Philip, J.R. 1964. Similarity hypothesis for capillary hysteresis in porous materials. *J Geophys Res* 69(8): 1553–1562. doi: 10.1029/JZ069I008P01553.

Poulovassilis, A. 1970. The Effect of the Entrapped Air on the Hysteresis Curves of a Porous Body and on its Hydraulic Conductivity. *Soil Sci* 109(3): 154–162. https://journals.lww.com/soilsci/citation/1970/03000/the_effect_of_the_entrapped_air_on_the_hysteresis.3.aspx (accessed 11 October 2022).

Raeesi, B., N.R. Morrow, G. Mason, and V. Zone. 2014. Capillary Pressure Hysteresis Behavior of Three Sandstones Measured with a Multistep Outflow–Inflow Apparatus. *Vadose Zone Journal* 13(3): 1–12. doi: 10.2136/VZJ2013.06.0097.

Schroth, M.H., J.D. Istok, S.J. Ahearn, and J.S. Selker. 1996. Characterization of Miller-Similar Silica Sands for Laboratory Hydrologic Studies. *Soil Science Society of America Journal* 60(5): 1331–1339. doi: 10.2136/SSSAJ1996.03615995006000050007X.

Stonestrom, D.A., and J. Rubin. 1989. Water content dependence of trapped air in two soils. *Water Resour Res* 25(9): 1947–1958. doi: 10.1029/WR025I009P01947.

Vaid, Y.P., and D. Negussey. 1984. RELATIVE DENSITY OF PLUVIATED SAND SAMPLES. *Soils and Foundations* 24(2): 101–105. doi:

10.3208/SANDF1972.24.2_101.

TABLE 1. Particle size range, particle density (ρ_s), bulk density (ρ_b) and computed porosity ($\phi = 1 - \rho_b/\rho_s$) of quartz sand.

	Size range	Difference	ρ_s	ρ_b	ϕ
	μm	μm	g cm^{-3}	g cm^{-3}	
Graded sand	< 1180		2.65 ^a	1.85±0.0054	0.303
20/25	710-850	140	2.65 ^a	1.89±0.0074	0.286
25/30	600-710	110	2.65 ^a	1.87±0.0035	0.294
30/35	500-600	100	2.65 ^a	1.85±0.0036	0.301
35/40	425-500	75	2.65 ^a	1.84±0.0074	0.307
40/45	355-425	70	2.65 ^a	1.79±0.0035	0.325
45/60	250-355	105	2.65 ^a	1.77±0.0067	0.333
60/70	212-250	38	2.65 ^a	1.79±0.0084	0.323

^aDixon et al. (2023)

TABLE 2. Hysteretic water retention parameters (van Genuchten, 1980) for the initial drying (d0)-, main drying (d)- and main wetting (w)-curves of quartz sand.

		Particle size range by sieve number							
		Graded sand	20/25	25/30	30/35	35/40	40/45	45/60	60/70
		Particle size range (μm)							
		< 1180	710-850	600-710	500-600	425-500	355-425	250-355	212-250
Initial drying process (d0)									
θ_r^{d0}	$\text{cm}^3 \text{cm}^{-3}$	0.019	0.022	0.013	0.013	0.020	0.022	0.036	0.064
θ_s^{d0}	$\text{cm}^3 \text{cm}^{-3}$	0.30	0.27	0.28	0.28	0.29	0.32	0.35	0.33
α^{d0}	cm^{-1}	0.047	0.086	0.088	0.079	0.058	0.051	0.040	0.031
n^{d0}		6.0	11	9.6	8.6	9.8	7.7	8.3	13
Main drying process (d)									
θ_r^d	$\text{cm}^3 \text{cm}^{-3}$	0.019	0.022	0.012	0.014	0.020	0.026	0.037	0.057
θ_s^d	$\text{cm}^3 \text{cm}^{-3}$	0.29	0.26	0.27	0.26	0.28	0.32	0.34	0.33
α^d	cm^{-1}	0.058	0.091	0.093	0.099	0.063	0.056	0.044	0.033
n^d		4.4	8.7	7.7	4.9	7.2	5.7	6.5	8.5
Main wetting process (w)									
θ_r^w	$\text{cm}^3 \text{cm}^{-3}$	0.019	0.021	0.012	0.014	0.020	0.024	0.036	0.044
θ_s^w	$\text{cm}^3 \text{cm}^{-3}$	0.29	0.26	0.27	0.26	0.28	0.32	0.34	0.33
α^w	cm^{-1}	0.11	0.15	0.15	0.18	0.10	0.091	0.072	0.054
n^w		3.0	6.4	6.2	4.0	6.4	4.1	4.5	5.0

TABLE 3. Water retention parameters (van Genuchten, 1980) for quartz sand (Accusand) (after Schroth et al. (1996)).

		Particle size range by sieve number			
		12/20	20/30	30/40	40/50
		Particle size range (μm)			
		850–1700	600–850	425–600	300–425
θ_r	$\text{cm}^3 \text{cm}^{-3}$	0.012	0.016	0.018	0.02
θ_s	$\text{cm}^3 \text{cm}^{-3}$	0.35	0.35	0.35	0.35
α	cm^{-1}	0.15	0.10	0.068	0.045
n		7.4	11	13	12

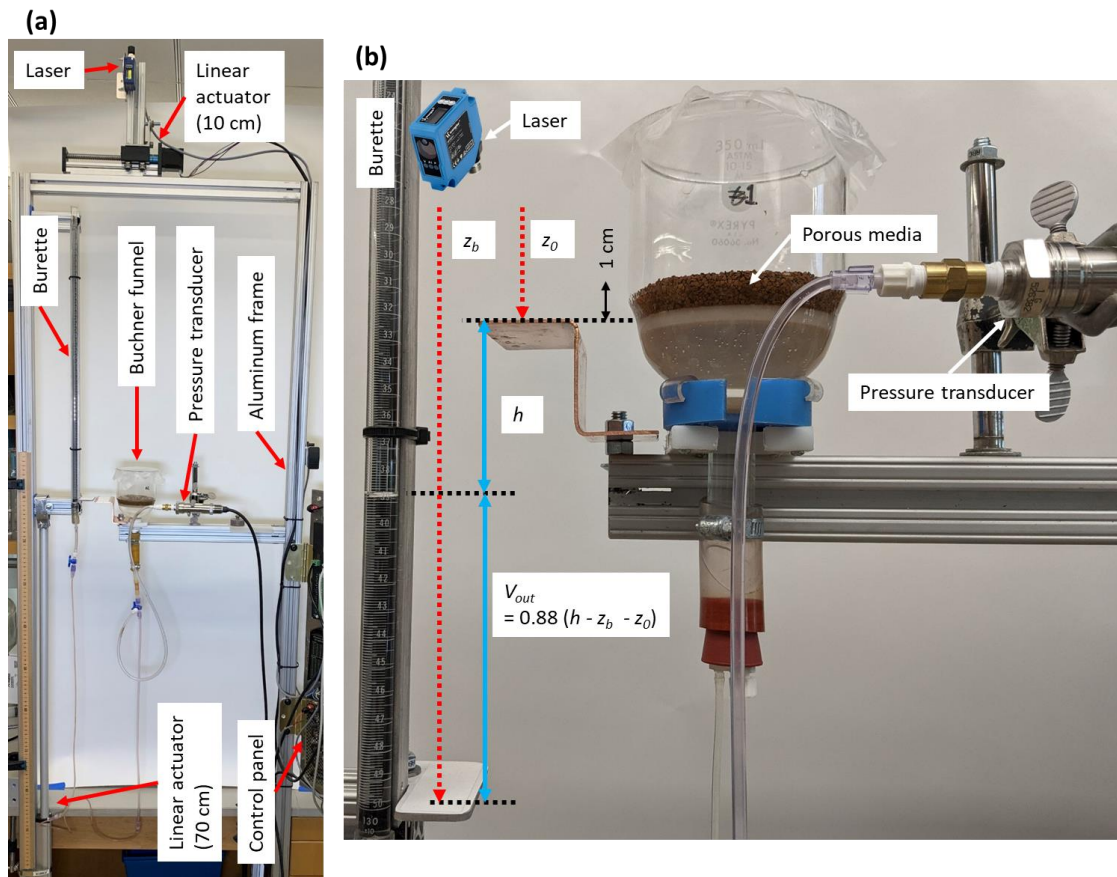


FIGURE 1. (a) Automated water retention measurement system consisting of a compound pressure transducer, a diffuse laser mounted on a 10 cm linear actuator, a 50 ml burette attached to a 70 cm linear actuator, a fritted Buchner funnel, a T-slot-based outer aluminum frame and the control panel and (b) a magnified picture of the coarse-textured porous medium water retention measurement system. The laser read two vertical distances of the reference height (z_0) and the burette position (z_b). The pressure transducer output h values at the base of the test media, and the outflow/inflow of the porous media (V_{out}) was then computed using measurements of h , z_b and z_0 .

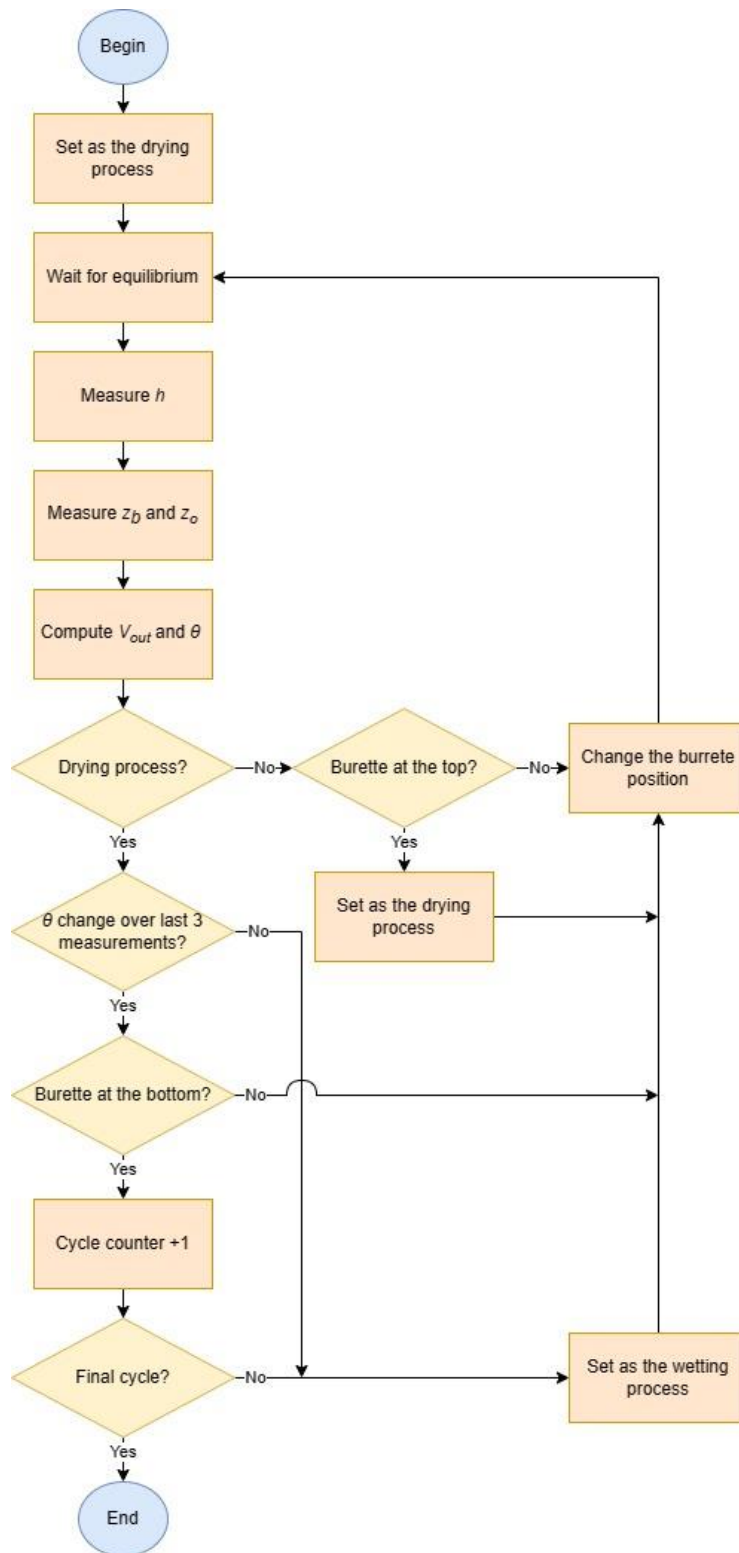


FIGURE 2. Automated water retention measurement system flowchart.

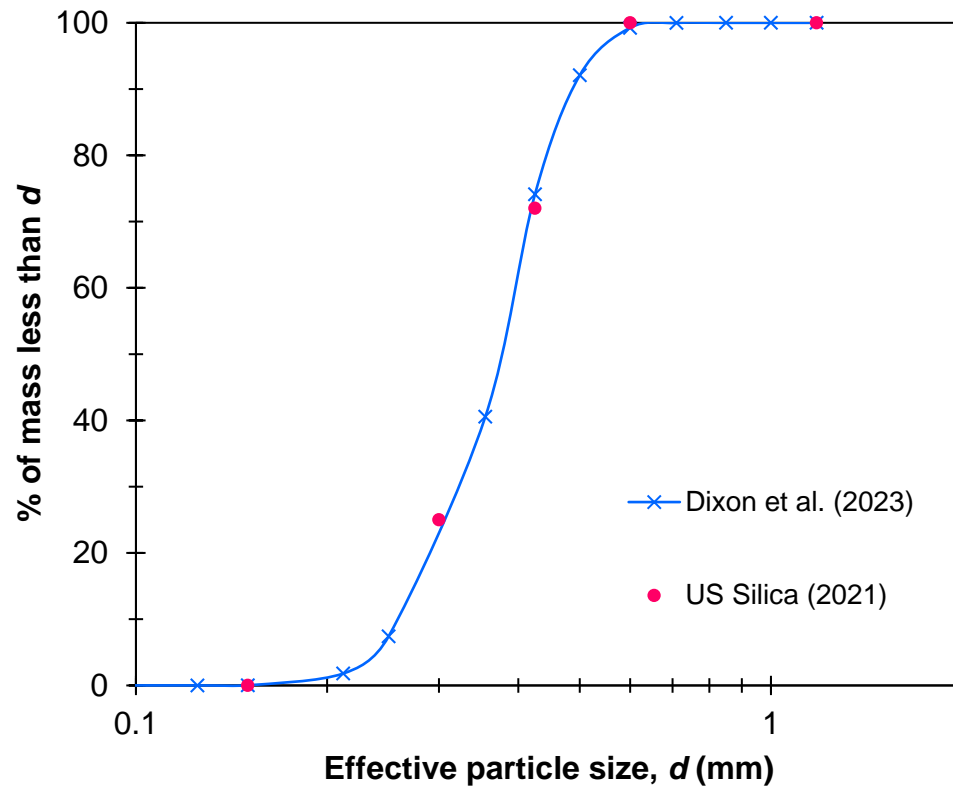


FIGURE 3. Cumulative particle distribution of graded sand.

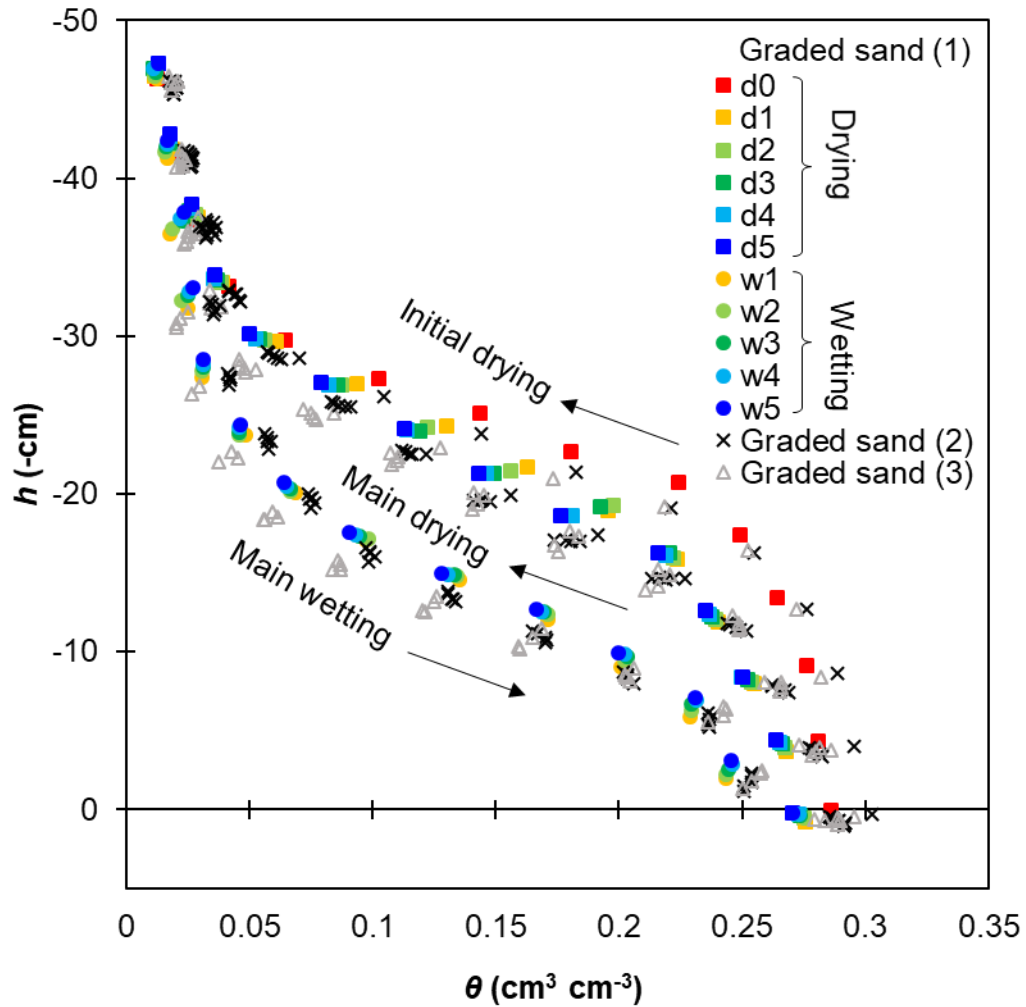


FIGURE 4. Triplicated measurements of the automated hysteretic water retention in graded sand. Colored squares and circles represent the first set of “graded sand (1)” measurements illustrating some drift in the data. Black crosses and gray triangles labeled “graded sand (2)” and “graded sand (3)”, represent the second and the third measurement sets. Drying cycle measurements included the fully saturated sample’s initial drying cycle labeled “d0” (graded sand (1)) with adjacent graded sand (2) and graded sand (3) data also presented.

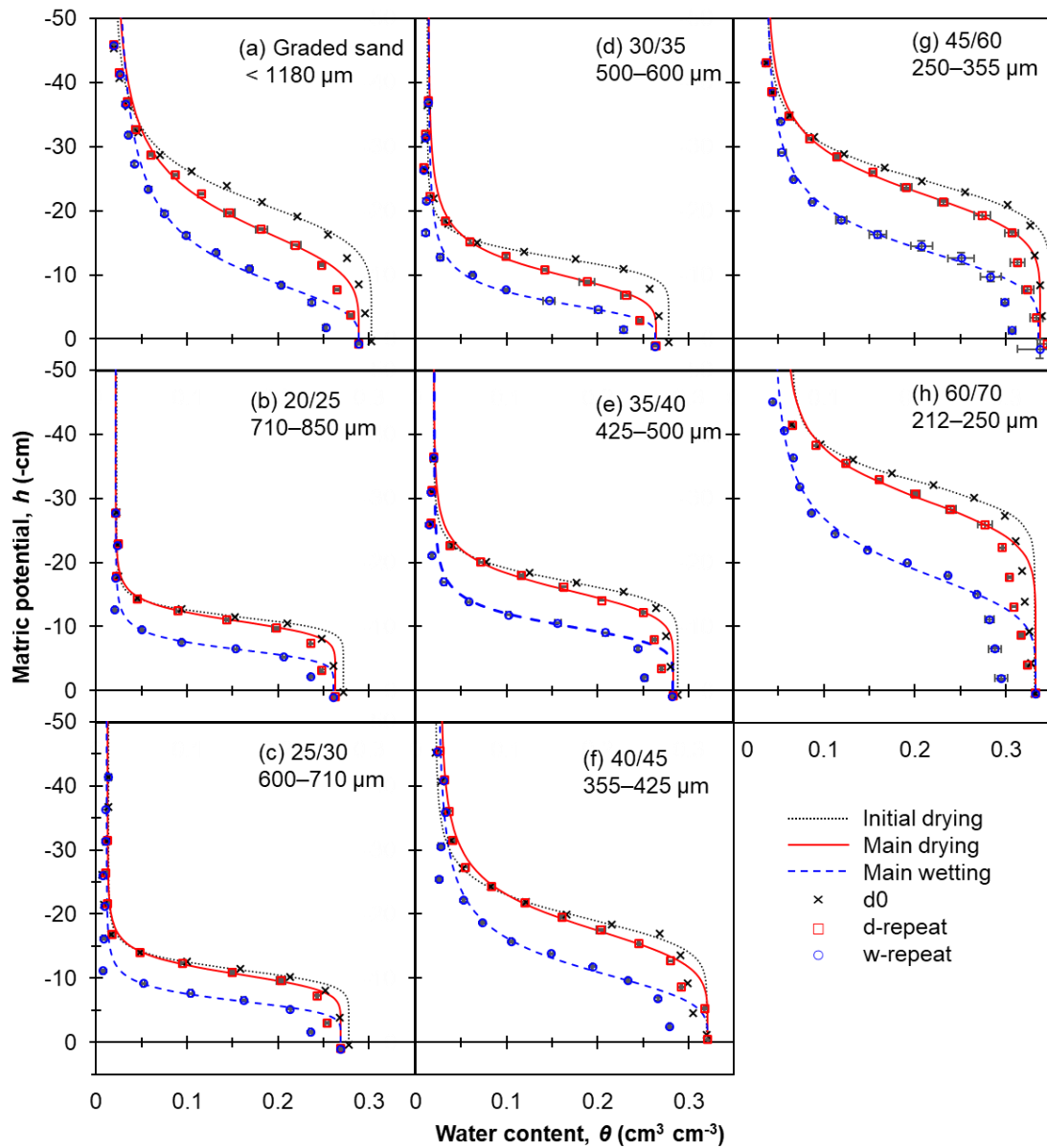


FIGURE 5. Hysteretic water retention measurements and fitted van Genuchten (1980) (VG) water retention models describing (a) C778 graded- and (b)–(h) sieved-quartz sand (ASTM-C778). Optimized VG model parameters are presented in Table 2. Vertical- and horizontal- bars represented standard deviation values for each symbol from triplicate measurements.

CHAPTER V

CHARACTERIZING HYSTERETIC WATER RETENTION OF SYNTHETIC- AND
NATURAL-FIBERS AS CANDIDATE PLANT GROWTH MEDIA

Abstract

Water retention in granular growth media has been extensively studied, however, limited research has explored the water retention of fibrous materials as candidate plant growth media. This study investigates the physical properties and hysteretic water retention characteristics of various lightweight fibrous media as potential candidates for supporting plant growth. The research encompasses both synthetic fibers, including woven microfibers and a non-woven capillary mat, and natural fibers such as peat moss, jute, linen, and a cellulosic sponge. Utilizing an automated hanging water column apparatus, water retention measurements were conducted over a matric potential (h) range of $0 < h < -50$ cm, focusing on fabric media usage in plant growth systems. The hysteretic water retention curves of synthetic and natural fibers resembled decreasing hyperbolic functions observed in typical plant growth media, with natural fibers exhibiting drastic water retention curves from saturation (θ_s) to residual water content (θ_r) within the h range between -20 and 0 cm. Conversely, synthetic fibers displayed reduced θ_s values, potentially due to larger pores between weaving structures compacted near-saturation. Additionally, certain woven synthetic fibers demonstrated significant volume changes during drying and wetting processes, emphasizing the need for corrections in water retention measurements. The study also demonstrates the feasibility of plant growth in

woven synthetic fibers, particularly microfibers, highlighting their potential as viable alternatives for plant growth media. Further optimization is recommended to determine the ideal water status, container geometry, and bulk density (ρ_b) to enhance containerized plant cultivation using fabric media. Overall, this research provides valuable insights for designing fabric-based plant growth media, offering opportunities to tailor media formulations to specific plant requirements for more efficient and sustainable agricultural practices.

1. Introduction

Climate change poses a significant threat to global agriculture by disrupting seasonal precipitation and temperature patterns, resulting in events such as flooding and drought (Malhi et al., 2021). Amidst these challenges and the increasing demand for food and water security, there is growing interest in crop production within controlled environments such as greenhouses and households, using containerized porous growth media (also called substrate), particularly as an alternative to conventional field-grown methods (Fields et al., 2021). Furthermore, containerized crop production has garnered attention for its potential application in reduced gravity conditions, aiming to support astronauts' dietary and mental well-being (Haeuplik-Meusburger et al., 2014).

Soilless media, characterized by their lightweight coarse-textured porous nature and sterilizability, have gained traction in both commercial and residential settings (Caron et al., 2015). Peat moss, a staple in horticulture due to its high porosity (ϕ) and cation exchange capacity, has traditionally been widely used. However, concerns about its environmental impact, including greenhouse gas emissions associated with peat bog extraction, have led to a search for sustainable alternatives (Yu et al., 2010; IUCN, 2023).

Consequently, there has been a surge of interest in exploring various alternative soilless media, with fabric media emerging as a particularly promising option.

Fabric media, characterized by their lightweight, affordability, availability, and porous structure, offer several advantages as soilless growth media. For instance, mineral wool, hemp fiber storck mats (Dirkes et al., 2021), and knitted fabrics (Storck et al., 2019; Dirkes et al., 2021) are being explored for low-cost vertical farming, including hydroponic, aeroponic, and aquaponic systems. Studies have demonstrated the applicability of materials like sponges (Kyriacou et al., 2020; Paradiso et al., 2020; Zhao et al., 2022) and 3D-printed foams (Takeuchi, 2019) for cultivating a variety of crops in a controlled environment. Additionally, both woven and non-woven fabrics have been utilized as growth media for uniform water distribution, aiming for sustainable crop production under reduced gravity conditions, such as the Svet Space Greenhouse (Bingham et al., 2000) and VEGGIE (Massa et al., 2017).

With the growing interest in various fibrous media, understanding their hydraulic properties, particularly their hysteretic water retention characteristics, is essential for designing and optimizing plant growth systems. Studies also revealed that the different weave structures and fabric densities affect the water absorption in fibrous media (e.g., Tang et al., 2005; Nyoni and Brook, 2006; Mhetre and Parachuru, 2010; Maqsood et al., 2016). Water retention in porous media relates to the media's volumetric water content (θ) and the hydraulic energy state, namely matric potential (h) in saturated and unsaturated conditions. Hysteretic water retention behavior, which involves different pathways of water held in the pore structure during drying and wetting processes, is influenced by phenomena such as the ink bottle effect, varying liquid-solid contact angles, air entrapment,

and volume changes due to swelling/shrinking of the porous media (Pham et al., 2005). This understanding is crucial as evapotranspiration and irrigation subject the porous media to alternating drying and wetting processes. Inadequate comprehension of the hysteretic water retention in growth media can lead to errors in estimating root zone water- and air-filled porosity, potentially resulting in hypoxia or drought stress. Thus, there is a pressing need to characterize the hydraulic properties, especially hysteretic water retention characteristics of various growth media.

Past studies explored the mechanism and the characterization of hydraulic properties in fibrous media, laying the groundwork for our research (e.g., Preston and Nimkar, 1949; Hollies et al., 1957; Morton and Hearle, 2008; Azeem et al., 2017). While existing methods (ASTM International, 2018, 2021) provide valuable insights into water retention characteristics of fabric media, they fall short in capturing the hydraulic properties within an ideal and practical h range for plant growth (i.e., $-100 < h < 0$ cm) (Pecanha et al., 2021; Heiskanen, 1995). Preston and Nimkar (1949) introduced the hanging water column experiment which was originally demonstrated by Haines's (1930) for characterizing water retention in mineral soils, however, their study was applied in limited fabric media including cotton. Dixon et al. (2023) demonstrated an automated water retention measurement system based on the traditional hanging water column method initially introduced by Haines (1930). The system comprises 1) a compound pressure transducer for media's θ and h determinations, 2) linear actuators, 3) a burette, and 4) a diffuse laser distance sensor. This automated water retention system offers repeatable data for coarse-textured media with a higher h range between 0 and -50 cm for both drying and wetting processes.

In this study, we focus on characterizing fabric plant growth media, classifying them into two main categories: synthetic fibers and natural fibers. Synthetic fibers include woven fabric (e.g., microfiber) and non-woven fibers, while natural fibers encompass traditional indoor plant growth media like peat moss and traditional woven plant fibers such as jute and linen, as well as non-woven materials like cellulosic sponge. Together, these fall under the broader category of candidate plant growth fibrous media. The primary objective of this research was to characterize the hysteretic water retention of various fibrous media, including both synthetic and natural fibers with a focus on evaluating physical and hydraulic properties for containerized crop production. In addition to characterizing the physical and hydraulic properties of various fibrous media, this study also included a subset of plant growth experiments to demonstrate plant growth in woven synthetic fibers. While the primary focus remains on assessing the suitability of these media for containerized crop production, the plant growth experiments serve as a practical demonstration of their potential applications in containerized horticulture. By examining both the physical properties and growth outcomes, this study aims to provide a comprehensive understanding of the role of fabric media in sustainable agricultural practices.

2. THEORETICAL

2.1 Physical Properties

We outline fundamental physical properties commonly used in horticulture and soil science, including material density (ρ_s in g cm^{-3}), bulk density (ρ_b in g cm^{-3}), and porosity (φ) as follows

$$\rho_s = M_s/V_s, \rho_b = M_s/V_t \quad (1)$$

where M and V represent the mass and the volume, and subscripts of s and t represent the material and the total bulk media. The term V_t is the sum of the volume of air (V_a), water (V_w), and material (V_s). The term ρ_s refers to the density of the material itself, while ρ_b encompasses the bulk porous media, accounting for the total volume including the fabric medium and pore space. The φ is defined as the ratio of pore space volume to the bulk volume of the media and is commonly calculated as $\varphi = 1 - \rho_s/\rho_b$. Additionally, we introduce the concept used in the textile industry, Grams per Square Meter (GSM in g m^{-2} , also called fabric aerial density) which describes the fabric dry mass of fabric per square meter of sheet. The term GSM is a common physical property used in textile fields to characterize the density of fabric media (e.g., Iftikhar et al., 2020). It is important to note that while ρ_b is a volumetric concept, GSM is associated with area measurements.

2.2 Water Retention Model

The widely spread model for describing continuous water retention of porous media, $\theta(h)$, is developed by van Genuchten (1980):

$$\theta(h) = \theta_r + (\theta_s - \theta_r) \left[\frac{1}{1 + (\alpha|h|)^n} \right]^m \quad (2)$$

where θ_s and θ_r are the volumetric water content values ($\text{cm}^3 \text{cm}^{-3}$) at the saturation- and residual-condition, respectively. The parameter, α (cm^{-1}) influences the curve shape and is often interpreted as the reciprocal of the air-entry potential (cm) of the media. Two dimensionless curve shape parameters, m and n , are related to the pore size distribution with m often calculated as $m = 1 - 1/n$. The hysteretic water retention encompasses the initial (or primary) drying process, the main (or secondary) drying and wetting processes, and potential intermediate scanning branches. The common approach to characterize the hysteretic water retention of the main drying and the main wetting processes is to apply

individual parameters of the water retention model (Equation (1)) in each process (Pham et al., 2005). For example, parameters such as θ_r^d , θ_s^d , α^d , n^d , and m^d represent the main drying parameters, while θ_r^w , θ_s^w , α^w , n^w , and m^w represent the main wetting parameters.

3. MATERIALS AND METHODS

3.1 Candidate Growth Media Selection

We selected ten fibrous media, categorized into two groups: a) synthetic fibers and b) natural fibers as presented in Figure 1. Synthetic fibers included five microfibers with various weave structures from The Rag Company, Boise, ID, namely Spa and Yoga (SY), The Gauntlet (GA), Creature Edgeless (CR), Platinum Pluffle (PL), and Dry Me A River (DR), along with the capillary mat (CA) (CapMat II, Phytotronics Inc., Earth City, MO). Natural fibers consisted of jute (JU) (Natural Burlap Ribbon, LWR CRAFTS, <http://www.lwrcrafts.com/>), linen (LI) (Linen Fabric Ribbon, Firefly Imports), a cellulosic sponge (CE) (3M, Saint Paul, MN), and coarse peat moss (PE) (Sunterra Horticulture, Winnipeg, Manitoba, Canada).

Table 1 presents the chemical composition of each fabric, the manufacturer-provided GSM value, and the pile/weave structure. Pile refers to the elevated surface composed of upright loops or strands of yarn, while weave describes how the yarn on the surface is oriented to create woven fabric. Synthetic fibers exhibit various weave structures including terry, twist loop, plush, waffle, and plain, with the *GSM* value in synthetic fiber ranging from 365 to 900 g m⁻². In contrast, both jute and linen display a plain weave pattern, indicating a visible pore size of approximately 1 mm in jute, which may influence water retention near saturation. The cellulosic sponge also features large pores exceeding

5 mm, suggesting a reduced θ value near saturation.

The major components of synthetic and natural fibers were polyester and cellulose, respectively, as detailed in Table 1. While each bundle of synthetic fibers often exhibits hydrophobicity due to a high contact angle ($> 90^\circ$) (Parvinzadeh Gashti, 2012), synthetic fibers often display hydrophilicity by reducing fiber thickness and altering the cross-sectional shape of the fiber during the manufacturing process (Park et al., 2001). In contrast, natural fibers containing cellulose intrinsically exhibit hydrophilicity due to small contact angles (Kontturi et al., 2011; Monteiro et al., 2011; Schellbach et al., 2016). Various chemical and thermal treatments can also modify the contact angle and alter water absorbency in both synthetic and natural fibers (Cameron et al., 1997; Li et al., 2007; Ferrero and Periolatto, 2015), however, due to the challenge of defining treatments for each commercially available fabric, all fabrics were rinsed with water and air-dried for at least 24 hours before the experiment.

3.2 Physical Property Measurements

The ρ_s value of fibrous media was determined using the water displacement method with 100 ml volumetric flasks (Flint and Flint, 2018). Air-dried fabric strips weighing between 4 and 9 g were added to each flask and triplicated measurements were conducted to obtain average mean and standard deviation values. The ρ_b value was calculated based on the oven-dried mass at 80°C divided by the volume of the fibrous media used for water retention measurements. The φ values were then computed using measured ρ_s and ρ_b values ($\varphi = 1 - \rho_b/\rho_s$).

The particle size distribution of peat moss was determined by sieving three sets of

50g air-dried samples with an averaged gravimetric water content of 1.1 g g^{-1} . Eight sieves with descending opening sizes (8.00-, 6.35-, 4.75-, 2.00-, 0.85-, 0.425-, 0.250-, 0.150-mm) based on ASTM mesh sizes were used. Initial hand sieving was conducted using two stacked sieves with coarser mesh sizes (8.00- and 6.35 mm), and particles passing through the 6.35 mm sieve were collected and sieved with finer meshes. A sieve shaker (CE Tyler RX-24, Combustion Engineering, New York, NY) was employed to sieve each sample for 15 minutes with stacked sieves with descending opening sizes (4.75-, 2.00-, 0.85-, 0.425-, 0.250-, 0.150-mm). The particles remaining on each sieve and those collected in the pan ($< 0.150 \text{ mm}$) were oven-dried at 80°C for 24 hours and weighed to compute particle size distribution. Triplicated measurements were performed to obtain average and standard deviation values.

3.3 Water Retention Measurements

The automated hanging water column measurement, as demonstrated by Dixon et al. (2023), was employed to measure the hysteretic water retention of all fibrous media. This method involves monitoring and collecting data on the fibrous media's h and θ at different h conditions. The automated system utilized a high-precision pressure transducer, a diffuse laser, two linear actuators, a 50 ml burette, and a 350 ml fritted Buchner funnel (inner diameter = 7.4 cm). Data monitoring and collection were programmed and controlled using a datalogger (CR1000, Campbell Scientific Inc., Logan UT). Further details of the automated hanging water column measurements, including the algorithm and the code written in the CR-Basic program, can be found in Dixon et al. (2023).

The automated measurements involved an initial drying water retention starting

from fully saturated media, followed by repeatable drying and wetting water retention within a h range between -50 and 0 cm (saturation). Before initiating the measurements, hydraulic connections were ensured from the testing media through the Buchner funnel, all water lines, and the pressure transducer. All testing media, except for the cellulosic sponge, were cut into a disk shape (diameter of 7.4 cm) to fit the sample and make good contact with the fritted ceramic plate in the funnel. To ensure the sample height of 1 cm at saturation, stacking of fabric media was carried out for those fabrics with a single layer thickness of less than 1 cm. Refer to Table 1 for information on the total thickness of each medium and the number of layers used for water retention measurements. The cellulosic sponge was cut into a square sheet ($3.0 \times 3.0 \times 1.0$ cm) and placed on the ceramic plate.

Saturating each medium in the Buchner funnel for a minimum of 12 hours was essential to ensure complete saturation. The cellulosic sponge, due to its large-trapped air during saturation, required manual squeezing to remove trapped air slowly. After saturation, excess water was removed from the three-way stop-cock, and the h value was set to $h = 0$ cm at the bottom before commencing the automated measurements.

The automated measurements provided initial drying water retention, followed by triplicated main drying- and main wetting-water retention. Following the completion of the automated measurements at the lowest h value ($h < -50$ cm), the sample was removed from the Buchner funnel. The final θ of the sample was computed by oven-drying at 80°C for 24 hours. All θ values were then corrected based on the oven-dried θ value.

3.4 Parameter Optimization for Hysteretic Water Retention Model

Water retention parameters (θ_r , θ_s , α , and n) for initial drying, main drying, and

main wetting processes were individually determined through automated measurements. This separation was employed because the main drying process might exhibit discrepancies from the initial drying process due to air entrainment in the media (Dixon et al., 2023). The final θ measurement and the computed φ value in Table 3 of each medium served as initial guess values for each process. Parameters for each process were then simultaneously optimized by minimizing the objective function (OF) given by:

$$OF = \sum[\theta_m - \theta]^2 \quad (3)$$

where θ_m is the volumetric water content from the automated measurements, and θ is the computed volumetric water content using Equation (1).

3.5 Plant Growth Experiments in Synthetic Fibers

We demonstrated the in-situ 30-day plant growth experiment using a subset of tested synthetic fibers, including Spa and Yoga (SY), The Gauntlet (GA), Creature Edgeless (CR), Platinum Pluffle (PL) and Dry Me A River (DR). Figure 2a shows the plant growth experiment on day 2 in Spa and Yoga. Each fabric medium was packed into a plastic column with a diameter of 10.8 cm and a height of 10 cm. Each medium was packed with the ρ_b value in Table 3. Air-dried fabric strips were rolled to accommodate the air stone, which was positioned at the center of the medium. This air stone served as a subsurface irrigation emitter, delivering water from the middle of the medium. Each container's air stone was connected to a pressure-regulating check valve (details) and a Mariotte bottle (McCarthy, 1934; Holden, 2004) filled with Hoagland nutrient solution (solution electrical conductivity of 1 dS m⁻¹). This irrigation system maintained unsaturated conditions in each fabric medium during the growth period by regulating the h

value in the middle of the medium at $h = -5$ cm. A pressure transducer installed between the check valve and the air stone, along with a three-way stop-cock, validated the h value in the growth medium. Pressure transducers were connected to a datalogger CR1000X (Campbell Scientific, Logan UT), recording measurements every 10 seconds and calculating the 1-minute moving average of measurements.

As shown in Figure 2a, the container's surface was covered by a disk with two holes (diameter of 3 cm) to prevent salt precipitation from the nutrient solution due to evaporation. The light source provided a 16-hour photoperiod with the photosynthetic photon flux density (PPFD) of $300 \mu\text{mol m}^{-2} \text{s}^{-1}$ at the surface of plant leaves, followed by the 8-hour dark period. The distance between the light source to the surface of the leaves was adjusted as plants grew to maintain a distance of at least 10 cm between the light source and the leaf surface.

Before sowing, all fibrous media were initially saturated with the nutrient solution and then drained to $h = -5$ cm. Three Romaine Lettuce ('Outrageous') seeds were sown on the exposed fabric surface where the hole was made. After germination, each containerized medium selected two seedlings. Thirty days after sowing, lettuce shoot mass was collected, and the shoots were oven-dried at 80°C for 2 days after harvesting. The dry shoot mass of each container was measured, and the average and standard deviation values were calculated. The experiment was designed in a completely randomized design with three replications for each fabric medium.

4. RESULTS

4.1 Physical Properties of Fibrous Media

Table 3 presents the measured values of ρ_s and ρ_b , along with the computed porosity ($\phi = 1 - \rho_b/\rho_s$) of fibrous media. While typical ρ_s values for polyester and polyamide are reported as 1.39 and 1.38 g cm⁻³, respectively (Deopura and Padaki, 2015), and plant fibers generally range from 1.4 to 1.5 g cm⁻³ (Chakravarty, 1961; Mwaikambo and Ansell, 2001), our measurements exhibited slightly smaller values. For instance, synthetic fibers showed ρ_s values ranging between 1.26 and 1.4 g cm⁻³, while jute and linen exhibited ρ_s values of 1.36 and 1.45 g cm⁻³, respectively. All fibrous media demonstrated ρ_b values significantly smaller than the typical ρ_b value in mineral soils (e.g., 1.25 g cm⁻³ in quartz sand), with minimum and maximum ρ_b values of 0.039 and 0.13 g cm⁻³. Consequently, these lightweight fibrous media resulted in higher ϕ values, ranging from 0.91 in Dry Me A River, CapMatII and jute to 0.96 in Creature Edgeless, Platinum Pluffle, and the cellulose sponge.

Table 2 displays the average and standard deviation values of the effective particle size distribution of peat moss. The particle size distribution revealed a bimodal structure, including 30.9±5.1% of peat moss particles ranging from 0.425 to 0.850 mm, while 13.5±3.6% of particles did not pass the 8.00 mm mesh sieve. Particles passing through the 2.00 mm mesh primarily consisted of peat moss fibers, while most lightly decomposed tree branches or roots and large peat moss aggregates remained above 2.00 mm. This composition may contribute to a lower ρ_b value of 0.09 g cm⁻³ and a higher ϕ value of 0.93 (refer to Table 3).

4.2 Hysteretic Water Retention Measurements

Figure 3a–3j display the measurements of hysteretic water retention for various

fibrous media, including synthetic and natural fibers (symbols), along with modeled water retention curves (lines). The determined hysteretic water retention parameters for each medium in the initial drying ($d0$), main drying (d), and main wetting (w) processes are listed in Table 4.

In all fibrous media, except for the drying processes of Capmat II (Figure 3f), the water retention measurements resembled a decreasing hyperbolic function, as typical in soilless media, as described in (Wallach, 2008). This was characterized by a gradual decrease in θ from saturation ($h = 0$ cm) to the unsaturated condition ($h = -50$ cm), with the air-entry matric potential approaching near saturation or being hardly visible.

The primary distinction in water retention between synthetic fibers (Figure 3a–3e) and peat moss (Figure 3j) was observed in the lower θ values ($\theta < 0.8$ cm³ cm⁻³) at saturation for synthetic fibers, while peat moss approached $\theta = 1.0$ cm³ cm⁻³. Synthetic fibers, such as Spa and Yoga, The Gauntlet, Creature Edgeless, Platinum Pluffle, and Dry Me A River, retained less water in the media at saturation compared to other fibrous media.

The initial drying (black crosses) and main drying (red circles) processes of Capmat II in Figure 3f revealed an air-entry matric potential value around $h = -12$ cm, with a substantial discrepancy in the main wetting water retention (blue circles). For instance, the main drying process showed $\theta = 0.82$ cm³ cm⁻³ at $h = -12$ cm, while the main wetting process exhibited $\theta = 0.34$ cm³ cm⁻³. The main wetting process of Capmat II showed almost no increase in the θ value at 0.35 cm³ cm⁻³ despite the h increase up to -7 cm. Then, the θ value drastically increased from 0.35 to 0.90 cm³ cm⁻³ within the h range of $-7 < h < -1$ cm. Ignoring this discrepancy between drying and wetting water retention characteristics could lead to failure in determining the optimal water- and air-filled porosities of Capmat

II.

Natural fibers, such as jute (Figure 3g) and the cellulosic sponge (Figure 3i), exhibited similar water retention for all processes, with the θ value substantially dropping from $0.9 \text{ cm}^3 \text{ cm}^{-3}$ (saturation) to the residual θ value within the h value of -10 cm . In contrast, linen (Figure 3h) showed water retention curves similar to synthetic fibers (Figure 3a–3e). The larger pore size in the jute and the cellulosic sponge (Figure 1) contributed to the higher θ_s values with drastic water retention slopes. Conversely, the relatively smaller pore size in linen (Figure 1) compared to jute and the cellulosic sponge provided a gradual water retention slope for all processes.

4.3 Water Retention Parameters

In Table 4, most fibrous media exhibited a zero value for θ_r , except for Capmat II, jute, the cellulosic sponge, and peat moss. While our study focused on characterizing water retention within the h range of $-50 < h < 0 \text{ cm}$, additional measurements for the lower h range (e.g., Tempe cells, pressure plate, or WP4) could reveal non-zero values in the θ_r parameter, offering reliable water retention parameters in drier conditions.

The maximum value of θ_s was observed in the initial drying process for all fibrous media, while reduced θ_s values in the main drying and main wetting processes were influenced by air entrainment in the media (Pham et al., 2005). The large pore space in certain media (e.g., jute and the cellulosic sponge) did not contribute to retaining water at saturation. Natural fibers, such as jute, linen, the cellulosic sponge, and peat moss, exhibited higher θ_s values in all processes, ranging from 0.76 to $0.99 \text{ cm}^3 \text{ cm}^{-3}$, while synthetic fibers, except for Capmat II, showed smaller θ_s values ranging from 0.59 to 0.75

$\text{cm}^3 \text{cm}^{-3}$. Although the φ values for all fibrous media were above 0.9 (Table 3), the pore space in the lightweight synthetic fibers could collapse or expand, altering its volume during wetting and drying processes, leading to a decrease in θ_s values.

Changes in the media height in fibrous media, especially in synthetic woven fibrous were observed. Especially the medium with a longer pile (refer to Table 1 and Figure 1), Creature Edgeless and Pluffle, exhibited a substantial change in sample height, altering the sample volume. However, natural fibers, such as jute, cellulosic sponge, and peat moss, did not show a substantial height change during water retention measurements. Non-linear height decreases were observed during the drying process, while height increases were observed during the wetting process. Volume changes, such as shrinking and swelling, are common phenomena in textiles (Suh, 1967) and organic fibrous media (Seidel et al., 2023). Specifically, an increase in the θ value during the drying process was attributed to shrinkage, while a decrease in the θ value during the wetting process was the consequence of swelling as water enters and leaves the pore space. Although we implemented distance measurements from the laser sensor to the medium surface, the laser sensor's resolution of ± 0.1 cm exhibited noise in height measurements (data not shown). This noise could also be attributed to the surface roughness of the media, especially the fibrous media with a long pile structure in Platinum Pluffle, showing inconsistent changes in sample height. Due to the poor resolution and inconsistency in height measurements, we did not correct the volume change in fibrous media for water retention measurements. Employing high-resolution sample height measurements during water retention measurements would provide a better understanding of the dynamics of the volume fraction of solid, water, and air in fibrous media.

4.4 Plant Growth Experiment in Synthetic Fibers

Table 5 presents the average value of h measurements over the 30-day growth experiment period. It's noteworthy that certain containers experienced flooding during the first and second weeks due to leakage in the Mariotte bottle. Consequently, the average h values for Platinum Pluffle were influenced by the elevated h levels during these flooding incidents. The h measurements also exhibited diurnal fluctuations ranging from 0.9 to 1.9 cm (Table 5) likely due to the combination of evapotranspiration and fluid redistribution, as well as the variation of the opening pressure value of individual check valves.

The average and standard deviation values of dry lettuce shoot yield are summarized in Table 5. Despite the challenges encountered during the plant growth experiment, all synthetic fibers displayed similar yields, ranging from 0.022 to 0.053 g cm⁻². However, it's essential to acknowledge the relatively high standard deviation values observed, ranging from 0.013 to 0.040 g cm⁻², which may indicate variability in growth performance within each medium type.

Figure 2b provides visual insights into the post-harvest condition of the containerized medium, focusing on Spa and Yoga. The image reveals air gaps between the container wall and the fabric, as well as between fabric layers, a phenomenon observed across all synthetic fibers. Additionally, the surface of the media exhibited green and black spots, indicative of bacterial or/and fungal growth. Notably, synthetic fibers with longer loop structures, such as Creature Edgeless and Platinum Pluffle (refer to Figure 1), exhibited noticeable changes in height during the experiment.

5. DISCUSSION

5.1 Hysteretic Water Retention of Fibrous Media

Understanding water retention dynamics in fabric media involves nuanced considerations of factors such as media composition, surface treatments, and pore structure geometry. Our study focused on a larger h range ($-50 < h < 0$ cm), where water retention primarily occurs due to capillarity rather than water absorption and diffusion within individual fibers. While surface hydrophilicity and hydrophobicity of fibers (e.g., cellulose and polymer) play a role, they may not fully account for the observed differences in θ_s values between natural fibers (composed of cellulose) and synthetic fibers (composed of polymer). These surface properties are more influential in drier conditions where water absorption becomes dominant (Das et al., 2009). As previously mentioned, water retention measurements using Tempe Cells, pressure plate apparatus, and WP4 could provide insightful information determining water retention characteristics at relatively small h ranges.

The variations in θ_s values among different fabric media could be attributed to weaving structure as well as pore size range, pore size distribution, and ρ_b . These physical properties similarly alter the water retention of granular porous media. Fibrous media containing larger pore structures, such as jute, the cellulosic sponge, and peat moss exhibited higher θ_s values. Despite synthetic fibers demonstrating the computed φ values of at least 0.9 (refer to Table 3), they retained less water at saturation compared to natural fibers and the non-woven synthetic fiber (e.g., Capmat II). The impact of weaving structure on water retention characteristics in synthetic fibers remains unclear, however, it's

speculated that larger pore structures between coarse weavings may remain empty under near-saturation conditions due to gravitational potential overcoming capillarity.

Our θ measurements were also influenced by volume changes in the media during the drying and wetting cycles. Synthetic fibers with longer-loop structures, such as Creature Edgeless and Platinum Pluffle, exhibited alterations in pore structure as they expanded and collapsed during these processes. While we monitored media height using a diffuse laser sensor during water retention measurements, inconsistent volume changes were observed. This inconsistency, likely due to individual fiber collapse during drying and expansion near saturation, was not corrected due to fluctuations in the laser sensor's resolution.

Most of the fibrous media showed similar water retention characteristics during the drying- and wetting-processes except for CapMat II. Daily evapotranspiration and irrigation practice induce the water retention characteristics to shift to the scanning branch of the water retention, which falls between the main wetting- and drying-water retention characteristics. The irrigation design should incorporate the hysteretic behavior of water retention, especially using media with substantial differences in hysteretic water retention characteristics such as CapMat II. Jones et al. (2012) addressed that the h value in the media is preferably used to control the irrigation rather than controlled by the θ value because plant root water and nutrient uptake are mainly driven by the potential gradient between the plant root surface and the growth media.

During water retention measurements, we maintained a media thickness between 0.7 and 1.2 cm (as detailed in Table 1), following the recommendation by Dixon et al. (2023), to mitigate the influence of gravitational potential gradient on water distribution

within the media. However, variations in fabric resulted in discrepancies in the number of layers present, such as a single layer in The Gauntlet versus ten layers in linen. This discrepancy in layering may introduce bias in the pore structure between layers, potentially impacting water retention characteristics. Moreover, the orientation of layering, whether horizontal or vertical relative to the direction of water movement during drying and wetting cycles should also be considered.

5.2 Exploring Candidate Plant Growth Fibrous Media

While our study did not explore the mechanical or chemical treatments applied to the surface of the fibrous media, it is important to acknowledge that natural fibers such as jute, linen, and cellulosic sponge are often subjected to various chemical treatments and surface modifications (Li et al., 2007). These treatments are typically employed due to the inherent susceptibility of cellulose-based materials to degradation (Li et al., 2007). However, obtaining detailed information about the specific treatment applications on fabric posed a challenge, especially for imported fabrics.

Despite our initial attempts to conduct plant growth tests on natural fibers like jute, linen, and cellulosic sponge (data not shown), these media failed to support plant growth. This could potentially be attributed to the combined effects of the hydraulic properties of the fabric, which we will address later, and chemical treatments on the fabric. One potential solution to support plant growth in natural fibers could be to source the media labeled as food-grade or medical-grade, as these are likely to have undergone fewer chemical treatments, thereby reducing the risk of exposure to potentially toxic substances.

Furthermore, during the plant growth experiment, we observed bacterial and/or

microbial growth on synthetic fabrics. Although our plant growth experiments did not focus on the effect of bacterial and/or microbial growth on fabric on plant growth, it's worth considering fabric media with anti-bacterial or anti-microbial properties, such as silver nanoparticle-coated fabrics (Li et al., 2013), which could potentially improve food safety aspects in plant cultivation practices. Future research could also explore the long-term effects of fabric media's water retention characteristics on plant growth and the root zone fauna, considering factors such as microbial activity, nutrient cycling, and root development.

5.3 Designing Plant Growth System using Fibrous Media Water Retention

In our study, we demonstrated successful plant growth in five readily available synthetic fibers. Our approach maintained the h value close to -5 cm in the middle of each growth medium container (10 cm height) using a pressure-regulating inline check valve and a Mariotte bottle. While we exhibited successful plant growth in five different media, it is also important to note that we also observed no plant growth in three media, jute, linen and cellulosic sponge. The water retention curve in both jute and cellulosic sponge (Figures 3g and 3i) exhibited a fairly steep slope from saturation to the residual θ condition within the h value between 0 and -10 cm. These steep water retention curves in jute and cellulosic sponge exhibited substantial change in the vertical distribution of θ within a container, for example, most of the water remains bottom half of the container and very little water is available near the surface for seedlings to take water and nutrients when the plants are small. Our five synthetic fibers which showed plant growth, did not exhibit such a steep water retention curve. Instead, synthetic fiber showed gradual vertical distribution of the θ

value, where the estimated saturation value near the surface in these synthetic fibers exceeded at least 0.41, whereas the estimated saturation in jute and cellulosic sponge was only 0.25 and 0.10, respectively. Gradual distribution of water- and air-filled porosity in the media provided flexibility in the irrigation management for the 10 cm tall container. On the other hand, a shallower container (< 10 cm) can be used for plant cultivation in the media with a steep water retention slope due to the narrow control range of h and θ values. Further research can address the plant yield altered by the water retention slope and the container height in the growth medium.

The target h value within the container could be further optimized based on the hysteretic water retention characteristics of each medium and the specific water requirements of different plant varieties. While we set $h = -5$ cm in the middle of the container in this study, it is important to note that this condition induced saturation ($h = 0$ cm) at the bottom of the containers, potentially leading to hypoxia due to oxygen deprivation and the reduced root zone volume for water and nutrient uptake.

Managing the h value of media is emphasized as a key aspect for improving plant growth and yield. The environmental conditions including the container geometry and irrigation (and drainage) method also influence the control range of h in the media. As noted by Jones and Or (1998), the control range of h in the plant growth media is determined not only by the growth media's hydraulic properties but also by the properties of irrigation interfaces. For example, the air-entry potential value in the subsurface irrigation emitter used in this study was -60 ± 6.5 cm, therefore inducing a lower h value than -60 cm in the growth media induces air entry in the irrigation emitter and hydraulic discontinuity between the emitter and the growth medium, which could alter water

distribution.

The container geometry, including the volume and height, also affects the water and air storage in the porous media (Bilderback and Fonteno, 1987; Caron et al., 2015). Understanding the water retention characteristics helps comprehend the water distribution across the growth media. The fibrous media we tested showed the α value in the van Genuchten's (1980) water retention parameter (Equation (2)) ranging between 0.049 and 5.33 (cm^{-1}), which resulted in the air-entry potential value ranging between -25 and -0.19 cm. Although the upper end of the ideal and practical matric potential value for plant cultivation under controlled environments is $h = -10$ cm (Pecanha et al., 2021; Heiskanen, 1995), the ideal matric potential range can be adjusted based on the selection of growth media.

Our findings have implications beyond agronomy and soil science, with potential applications in materials engineering and textile manufacturing. As demonstrated by Takeuchi (2019) in the fabrication of 3D-printed porous growth media for hydroponic systems, engineering ideal fibrous materials and weaving structures for containerized crop production could enhance sustainable crop production.

6. CONCLUSIONS

In this study, we introduced the physical property measurements and determination of hysteretic water retention characteristics in various lightweight fibrous media as candidate plant growth media. Our research encompassed a) synthetic fibers including woven microfibers and a non-woven capillary mat, as well as b) natural fibers including a traditional horticultural growth medium, peat moss, and traditional woven plant fibers such as jute and linen, as well as a cellulosic sponge.

Employing an automated hanging water column apparatus enabled efficient measurement of water retention data and estimation of van Genuchten model parameters describing the drying and wetting water retention within a relatively large h range of $0 < h < -50$ cm, with a specific emphasis on fibrous media usage in plant growth systems. The water retention curves in synthetic and natural fibers (e.g., linen) resembled a decreasing hyperbolic function observed in typical plant growth media, such as peat moss. Notably, large pore structures present in natural fibers, particularly jute, and the cellulosic sponge, exhibited a rapid drying process from saturation (θ_s) to residual water content (θ_r) within a h range between -20 and 0 cm in the water retention curve. In contrast, synthetic fibers exhibited reduced θ_s values, possibly due to the presence of the larger pores between the weaving structures, likely compressed and of limited contribution to the increase in θ_s values. Further investigation of water retention characteristics at lower h range as well as the impact of fabric layers and orientation of the fabric media provides a better understanding of the hydraulic properties of fabric media.

Furthermore, our study also demonstrated the feasibility of plant growth in woven synthetic fibers, particularly readily available microfibers, as viable alternatives for plant growth media. Gradual water retention slope in synthetic fiber maintained a minimum saturation value of 0.41 near the surface, promoting germination and plant growth. However, further optimization is required in determining ideal water status, container geometry and the ρ_b value accounted for hysteretic water retention characteristics to enhance containerized plant cultivation using fibrous media.

This study provides valuable insights for designing fabric-based plant growth media, with a focus on optimizing water retention characteristics to support plant growth.

By understanding how different fiber types and treatments influence water retention characteristics, we can tailor media formulations to specific plant requirements, leading to more efficient and sustainable agricultural practices.

REFERENCES

ASTM International. 2018. ASTM D2402-07 (2018): Standard Test Method for Water Retention of Textile Fibers (Centrifuge Procedure).

ASTM International. 2021. ASTM C1559-15 (2021): Standard Test Method for Determining Wicking of Fibrous Glass Blanket Insulation.

Azeem, M., A. Boughattas, J. Wiener, and A. Havelka. 2017. Mechanism of Liquid Water Transport in Fabrics; A Review. *Fibres and Textiles* 24(4).

Bilderback, T.E., and W.C. Fonteno. 1987. Effects of Container Geometry and Media Physical Properties on Air and Water Volumes in Containers. *J Environ Hortic* 5(4): 180–182. doi: 10.24266/0738-2898-5.4.180.

Bingham, G.E., S.B. Jones, D. Or, I.G. Podolski, M.A. Levinskikh, et al. 2000. Microgravity effects on water supply and substrate properties in porous matrix root support systems. *Acta Astronaut* 47(11): 839–848. doi: 10.1016/S0094-5765(00)00116-8.

Cameron, B.A., D.M. Brown, M.J. Dallas, and B. Brandt. 1997. Effect of Natural and Synthetic Fibers and Film and Moisture Content on Stratum Corneum Hydration in an Occlusive System. *Textile research journal* 67(8): 585–592.

Caron, J., R. Heinse, and S. Charpentier. 2015. Organic Materials Used in Agriculture, Horticulture, Reconstructed Soils, and Filtering Applications. *Vadose Zone Journal* 14(6): vzj2015.04.0057. doi: 10.2136/VZJ2015.04.0057/111897.

Chakravarty, A.C. 1961. Measurement of density of fibers of jute by density gradient column. *Journal of Polymer Science* 54(160): S52–S56. doi: 10.1002/POL.1961.1205416040.

Das, B., A. Das, V. Kothari, R. Fanguiero, and M.D. Araujo. 2009. Moisture Flow

through Blended Fabrics – Effect of Hydrophilicity. *J Eng Fiber Fabr* 4(4): 155892500900400. doi: 10.1177/155892500900400405.

Deopura, B.L., and N. V. Padaki. 2015. Synthetic Textile Fibres: Polyamide, Polyester and Aramid Fibres. *Textiles and Fashion: Materials, Design and Technology*: 97–114. doi: 10.1016/B978-1-84569-931-4.00005-2.

Dirkes, L., J.D. Massanés, R. Böttjer, J.L. Storck, and A. Ehrmann. 2021. Outdoor vertical farming on textile substrates. *IOP Conf Ser Mater Sci Eng* 1031(1): 012020. doi: 10.1088/1757-899X/1031/1/012020.

Dixon, C., A. Blakeslee, M. Mills, W. Sheng, and S.B. Jones. 2023. Automated hanging water column for characterizing water retention and hysteresis of coarse-textured porous media. *Soil Science Society of America Journal*. doi: 10.1002/saj2.20596.

Ferrero, F., and M. Periolatto. 2015. Modification of Surface Energy and Wetting of Textile Fibers. In: Aliofkhazraei, M., editor, *Wetting and Wettability*. InTech

Fields, J.S., J. Owen, A. Lamm, J.E. Altland, B.E. Jackson, et al. 2021. Soilless substrate science: a North American needs assessment to steer soilless substrate research into the future. *Acta Hort* (1317): 313–318. doi: 10.17660/ACTAHORTIC.2021.1317.36.

Flint, A.L., and L.E. Flint. 2018. 2.2 Particle Density. *Methods of Soil Analysis, Part 4: Physical Methods*: 229–240. doi: 10.2136/SSSABOOKSER5.4.C10.

van Genuchten, M.Th. 1980. A Closed-form Equation for Predicting the Hydraulic Conductivity of Unsaturated Soils 1. *Soil Science Society of America Journal* 44(5): 892–898. doi: 10.2136/sssaj1980.03615995004400050002x.

Haeuplik-Meusburger, S., C. Paterson, D. Schubert, and P. Zabel. 2014.

Greenhouses and their humanizing synergies. *Acta Astronaut* 96(1): 138–150. doi: 10.1016/j.actaastro.2013.11.031.

Haines, W.B. 1930. Studies in the physical properties of soil. V. The hysteresis effect in capillary properties, and the modes of moisture distribution associated therewith. *J Agric Sci* 20(1): 97–116. doi: 10.1017/S002185960008864X.

Heiskanen, J. 1995. Water Status of Sphagnum Peat and a Peat–Perlite Mixture in Containers Subjected to Irrigation Regimes. *HortScience* 30(2): 281–284. doi: 10.21273/HORTSCI.30.2.281.

Holden, J. 2004. Mariotte Bottle—Use in Hydrology. *Water Encyclopedia*. Wiley. p. 503–504

Hollies, N.R.S., M.M. Kaessinger, B.S. Watson, and H. Bogaty. 1957. Water Transport Mechanisms in Textile Materials. *Textile Research Journal* 27(1): 8–13. doi: 10.1177/004051755702700102.

Iftikhar, F., T. Hussain, Z. Ali, A. Nazir, D.C. Adolphe, et al. 2020. Investigation of Thermo-Physiological Comfort and Mechanical Properties of Fine Cotton Fabrics for Ladies' Summer Apparel. *Journal of Natural Fibers* 17(11): 1619–1629. doi: 10.1080/15440478.2019.1588185.

IUCN. 2023. Peatlands and climate change. IUCN.

Jones, S.B., and D. Or. 1998. Design of Porous Media for Optimal Gas and Liquid Fluxes to Plant Roots. *Soil Sci. Soc. Am. J.* 62(3): 563–573. doi: 10.2136/sssaj1998.03615995006200030002x.

Jones, S.B., D. Or, R. Heinse, and M. Tuller. 2012. Beyond Earth: Designing Root Zone Environments for Reduced Gravity Conditions. *Vadose Zo. J.* 11(1). doi:

10.2136/vzj2011.0081.

Kontturi, E., M. Suchy, P. Penttilä, B. Jean, K. Pirkkalainen, et al. 2011. Amorphous Characteristics of an Ultrathin Cellulose Film. *Biomacromolecules* 12(3): 770–777. doi: 10.1021/bm101382q.

Kyriacou, M.C., C. El-Nakhel, A. Pannico, G. Graziani, G.A. Soteriou, et al. 2020. Phenolic constitution, phytochemical and macronutrient content in three species of microgreens as modulated by natural fiber and synthetic substrates. *Antioxidants* 9(3). doi: 10.3390/ANTIOX9030252.

Li, J.-H., X.-S. Shao, Q. Zhou, M.-Z. Li, and Q.-Q. Zhang. 2013. The double effects of silver nanoparticles on the PVDF membrane: Surface hydrophilicity and antifouling performance. *Appl Surf Sci* 265: 663–670. doi: 10.1016/j.apsusc.2012.11.072.

Li, X., L.G. Tabil, and S. Panigrahi. 2007. Chemical Treatments of Natural Fiber for Use in Natural Fiber-Reinforced Composites: A Review. *J Polym Environ* 15(1): 25–33. doi: 10.1007/s10924-006-0042-3.

Malhi, G.S., M. Kaur, and P. Kaushik. 2021. Impact of Climate Change on Agriculture and Its Mitigation Strategies: A Review. *Sustainability* 2021, Vol. 13, Page 1318 13(3): 1318. doi: 10.3390/SU13031318.

Maqsood, M., Y. Nawab, K. Shaker, M. Umair, M. Ashraf, et al. 2016. Modelling the Effect of Weave Structure and Fabric Thread Density on Mechanical and Comfort Properties of Woven Fabrics. *Autex Research Journal* 16(3): 160–164. doi: 10.1515/aut-2015-0032.

Massa, G.D., N.F. Dufour, J.A. Carver, M.E. Hummerick, R.M. Wheeler, et al. 2017. VEG-01: Veggie hardware validation testing on the international space station. *Open*

Agric 2(1): 33–41. <https://www.degruyter.com/document/doi/10.1515/opag-2017-0003/html> (accessed 16 May 2021).

Mccarthy, E.L. 1934. Mariotte’s Bottle. *Science* (1979) 80(2065): 100.

Mhetre, S., and R. Parachuru. 2010. The effect of fabric structure and yarn-to-yarn liquid migration on liquid transport in fabrics. *Journal of the Textile Institute* 101(7): 621–626. doi: 10.1080/00405000802696469.

Monteiro, S.N., F.P.D. Lopes, A.P. Barbosa, A.B. Bevitori, I.L.A. Da Silva, et al. 2011. Natural Lignocellulosic Fibers as Engineering Materials—An Overview. *Metallurgical and Materials Transactions A* 42(10): 2963. doi: 10.1007/s11661-011-0789-6.

Morton, W., and J. Hearle. 2008. *Physical Properties of Textile Fibres*, Fourth Edition (W. Morton and J. Hearle, editors). CRC Press.

Mwaikambo, L.Y., and M.P. Ansell. 2001. The determination of porosity and cellulose content of plant fibers by density methods. *J Mater Sci Lett* 20(23): 2095–2096. doi: 10.1023/A:1013703809964.

Nyoni, A.B., and D. Brook. 2006. Wicking mechanisms in yarns—the key to fabric wicking performance. *Journal of the Textile Institute* 97(2): 119–128. doi: 10.1533/joti.2005.0128.

Paradiso, R., A. Ceriello, A. Pannico, S. Sorrentino, M. Palladino, et al. 2020. Design of a Module for Cultivation of Tuberos Plants in Microgravity: The ESA Project “Precursor of Food Production Unit” (PFPU). *Front Plant Sci* 11: 417. doi: 10.3389/fpls.2020.00417.

Park, M.-J., S.H. Kim, S.J. Kim, S.H. Jeong, and J. Jaung. 2001. Effect of Splitting

and Finishing on Absorption/Adsorption Properties of Split Polyester Microfiber Fabrics. *Textile Research Journal* 71(9): 831–840. doi: 10.1177/004051750107100913.

Parvinzadeh Gashti, M. 2012. Surface modification of synthetic fibers to improve performance: Recent approaches. *Global Journal of Physical Chemistry* 3(2): 1–10.

Peçanha, D.A., T.P.L. da Cunha-Chiamolera, Y. Chourak, E.Y. Martínez-Rivera, and M. Urrestarazu. 2021. Effect of the Matric Potential on Growth and Water, Nitrate and Potassium Absorption of Vegetables under Soilless Culture. *J. Soil Sci. Plant Nutr.* 21(4): 3493–3501. doi: 10.1007/S42729-021-00622-W/FIGURES/4.

Pham, H.Q., D.G. Fredlund, and S.L. Barbour. 2005. A study of hysteresis models for soil-water characteristic curves. <https://doi.org/10.1139/t05-071> 42(6): 1548–1568. doi: 10.1139/T05-071.

Preston, J.M., and M. V. Nimkar. 1949. MEASURING THE SWELLING OF FIBRES IN WATER. *Journal of the Textile Institute Proceedings* 40(7): P674–P688. doi: 10.1080/19447014908664692.

Schellbach, S.L., S.N. Monteiro, and J.W. Drelich. 2016. A novel method for contact angle measurements on natural fibers. *Mater Lett* 164: 599–604. doi: 10.1016/j.matlet.2015.11.039.

Seidel, R., U. Dettmann, and B. Tiemeyer. 2023. Reviewing and analyzing shrinkage of peat and other organic soils in relation to selected soil properties. *Vadose Zone Journal* 22(5). doi: 10.1002/vzj2.20264.

Storck, Böttjer, Vahle, Brockhagen, Grothe, et al. 2019. Seed Germination and Seedling Growth on Knitted Fabrics as New Substrates for Hydroponic Systems. *Horticulturae* 5(4): 73. doi: 10.3390/horticulturae5040073.

Suh, M.W. 1967. A Study of the Shrinkage of Plain Knitted Cotton Fabric, Based on the Structural Changes of the Loop Geometry Due to Yarn Swelling and Deswelling. *Textile Research Journal* 1: 417–431.

Takeuchi, Y. 2019. 3D Printable Hydroponics: A Digital Fabrication Pipeline for Soilless Plant Cultivation. *IEEE Access* 7: 35863–35873. doi: 10.1109/ACCESS.2019.2905233.

Tang, X., J.D. Whitcomb, Y. Li, and H.-J. Sue. 2005. Micromechanics modeling of moisture diffusion in woven composites. *Compos Sci Technol* 65(6): 817–826. doi: 10.1016/j.compscitech.2004.01.015.

Wallach, R. 2008. Physical characteristics of soilless media. *Soilless Culture: Theory and Practice*. Elsevier. p. 41–116

Yu, Z., J. Loisel, D.P. Brosseau, D.W. Beilman, and S.J. Hunt. 2010. Global peatland dynamics since the Last Glacial Maximum. *Geophys Res Lett* 37(13). doi: 10.1029/2010GL043584.

Zhao, Z., T. Xu, X. Pan, Susanti, J.C. White, et al. 2022. Sustainable Nutrient Substrates for Enhanced Seedling Development in Hydroponics. *ACS Sustain Chem Eng* 10(26): 8506–8516. doi: 10.1021/acssuschemeng.2c01668.

Table 1. Fibrous media's compositions, structure, GSM, thickness and number of layers used for the automated water retention measurements.

	Composition(s)	Weave	GSM	Thickness	No. Layers
			g m^{-2}	cm	
		a) Synthetic fiber			
Spa and Yoga (SY)	80% Polyester, 20% Polyamide	Terry	365	0.4	3
The Gauntlet (GA)	70% Polyester, 30% Polyamide	Twist Loop	900	1	1
Creature Edgeless (CR)	70% Polyester, 30% Polyamide	Dual Pile (long fibers/ tighter terry weave)	420	0.7	1
Platinum Pluffle (PL)	70% Polyester, 30% Polyamide	Hybrid Weave (half plush/ half waffle)	480	0.8	1
Dry Me A River (DR)	70% Polyester, 30% Polyamide	Waffle	390	0.4	3
Capillary Mat (CA)	Polypropylene, polyester and rayon			0.2	5
		b) Natural fiber			
Jute (JU)	Cellulose	Plain		0.4	2
Linen (LI)	Cellulose	Plain		0.1	10
Cellulosic sponge (CE)	Cellulose			1.1	1

Table 2. Mean and standard error values of effective particle size distribution of peat moss.

Opening size	Mean	Standard error
mm		%
8.00 <	13.5	3.6
6.35–8.00	8.1	0.70
4.75–6.35	4.8	2.2
2.00–4.75	13.3	1.7
0.850–2.00	19.7	1.4
0.425–0.850	30.9	5.1
0.250–0.425	6.7	3.8
0.150–0.250	1.7	0.90
< 0.150	1.2	0.68

Table 3. Physical properties including material density (ρ_s), bulk density (ρ_b) and computed porosity ($\varphi = 1 - \rho_s / \rho_b$).

	ρ_s	ρ_b	φ
	g cm ⁻³		
a) Synthetic fiber			
Spa and Yoga (SY)	1.26	0.083	0.93
The Gauntlet (GA)	1.28	0.10	0.92
Creature Edgeless (CR)	1.26	0.052	0.96
Platinum Pluffle (PL)	1.33	0.056	0.96
Dry Me A River (DR)	1.31	0.12	0.91
Capillary Mat (CA)	1.4	0.13	0.91
b) Natural fiber			
Jute (JU)	1.36	0.12	0.91
Linen (LI)	1.47	0.10	0.93
Cellulosic sponge (CE)	1.45 [†]	0.039	0.96
Peat moss (PE)	1.45	0.09	0.93

[†]Ramamoorthy et al. (2015)

Table 4. Water retention parameters of the van Genuchten (1980) model for the initial drying (d0)-, main drying (d)- and main wetting (w)-processes.

		θ_r	θ_s	α	n
		cm^3	cm^{-3}	cm^{-1}	
a) Synthetic fibers					
Spa and Yoga (SY)	Initial drying (d0)	0	0.73	0.094	1.9
	Main drying (d)	0	0.68	0.133	1.7
	Main wetting (w)	0	0.68	0.604	1.4
The Gauntlet (GA)	Initial drying (d0)	0	0.75	0.19	1.5
	Main drying (d)	0	0.69	0.37	1.3
	Main wetting (w)	0	0.69	1.49	1.2
Creature Edgeless (CE)	Initial drying (d0)	0	0.75	0.048	2.4
	Main drying (d)	0	0.68	0.071	1.9
	Main wetting (w)	0	0.74	0.993	1.3
Platinum Pluffle (PL)	Initial drying (d0)	0	0.75	0.37	1.5
	Main drying (d)	0	0.68	1.1	1.3
	Main wetting (w)	0	0.70	14	1.2
Dry Me A River (DR)	Initial drying (d0)	0	0.65	0.14	1.4
	Main drying (d)	0	0.61	0.50	1.2
	Main wetting (w)	0	0.59	2.2	1.1
Capmat II (CA)	Initial drying (d0)	0.32	0.97	0.060	6.8
	Main drying (d)	0.27	0.91	0.054	4.9
	Main wetting (w)	0.33	0.91	0.46	3.0
b) Natural fibers					
Jute (JU)	Initial drying (d0)	0.19	0.95	0.61	2.4
	Main drying (d)	0.17	0.85	0.74	2.0
	Main wetting (w)	0.075	0.80	4.0	1.4
Linen (LI)	Initial drying (d0)	0	0.90	0.083	2.1
	Main drying (d)	0	0.76	0.095	1.8
	Main wetting (w)	0	0.76	0.23	1.5
Cellulosic sponge (CE)	Initial drying (d0)	0.11	0.89	0.26	5.0
	Main drying (d)	0.090	0.81	0.37	3.1
	Main wetting (w)	0.039	0.87	2.4	1.7
Peat moss (PE)	Initial drying (d0)	0.34	0.99	0.15	2.4
	Main drying (d)	0.33	0.97	0.17	2.2
	Main wetting (w)	0.30	0.95	0.35	1.8

Table 5. The average and standard deviation values of triplicated h measurements and the plant dry shoot mass per unit area (g cm^{-2}) in synthetic woven fibers. The surface area of the container was 86.6 cm^2 .

	Daily average h	Dry shoot
	cm	g cm^{-2}
Spa and Yoga (SY)	-6.5 ± 1.7	0.022 ± 0.022
The Gauntlet (GA)	-5.8 ± 1.9	0.042 ± 0.034
Creature Edgeless (CR)	-5.9 ± 1.9	0.043 ± 0.013
Platinum Pluffle (PL)	-3.9 ± 0.9	0.043 ± 0.022
Dry Me A River (DR)	-6.7 ± 1.7	0.053 ± 0.040



Figure 1. Soiless media (left to right) including (a) synthetic fibers: Spa and Yoga (SY), The gauntlet (GA), Creature Edgeless (CR), Platinum Pluffle (PL), Dry Me A River (DR), CapMat II (CA) and (b) natural fibers: jute (JU), linen (LI), cellulosic sponge (CE) and peat moss (PE).

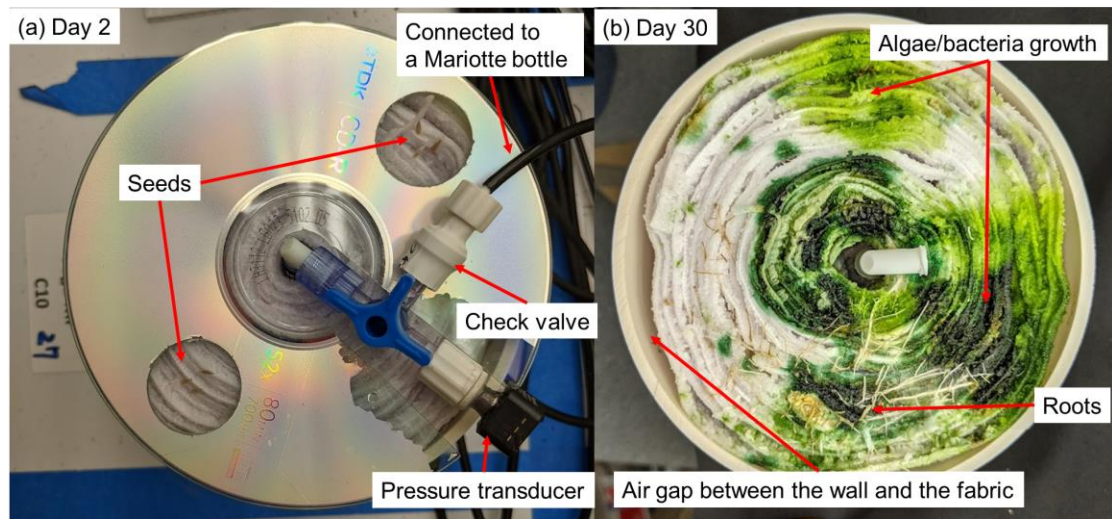


Figure 2. (a) Initial setup and (b) post-harvesting plant growth media, Spa and Yoga.

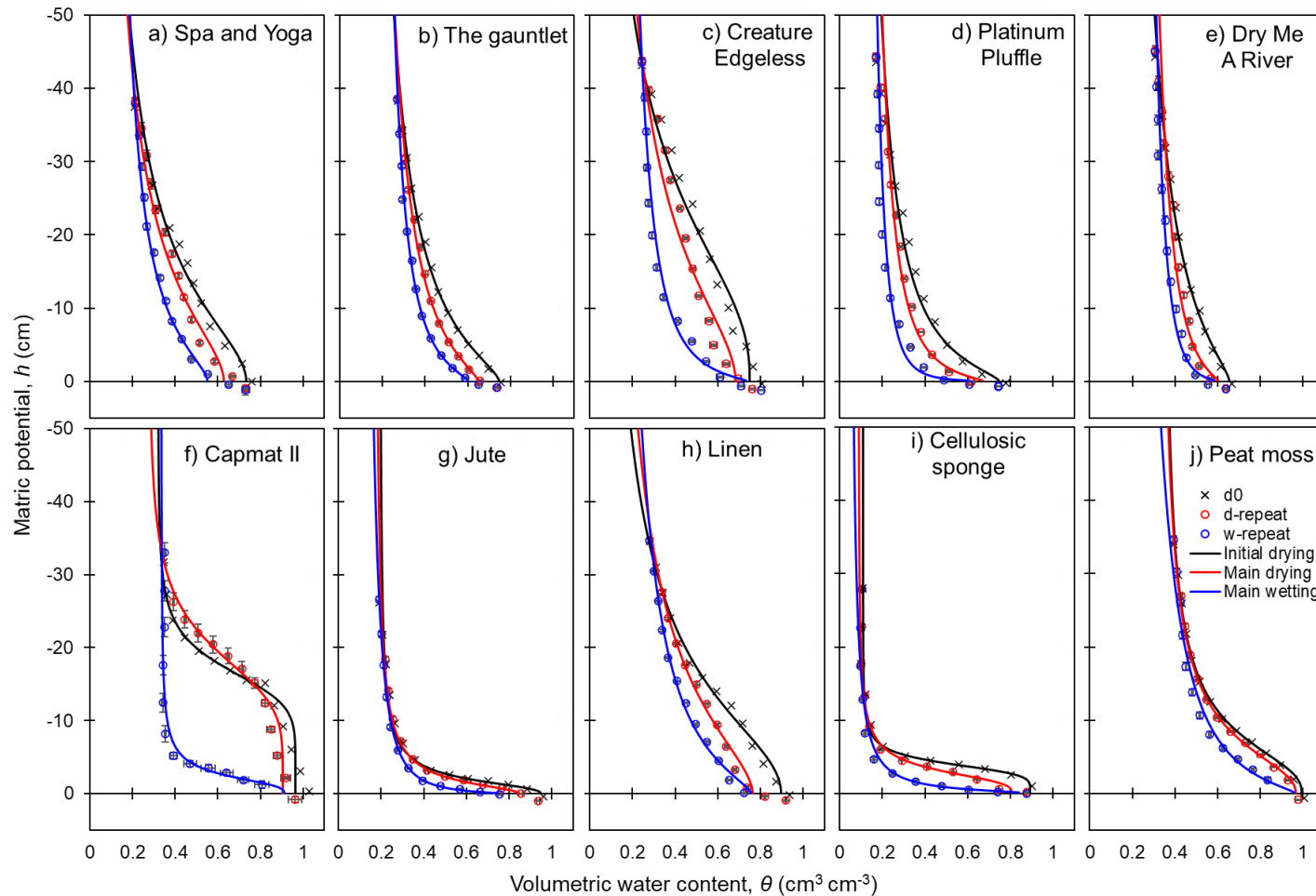


Figure 3. Hysteretic water retention measurements (symbols) including the first drying process (d0) and repeated drying (d-repeat)- and repeated wetting (w-repeat)-processes as well as fitted van Genuchten (1980) water retention models (lines) describing (a)–(f) Synthetic fibers and (g)–(i) natural fibers. Optimized water retention parameters are presented in **Error! Reference source not found.** Vertical- and horizontal- bars represented standard deviation values for each symbol from triplicated measurements.

CHAPTER VI

A PLANT-OPTIMAL IRRIGATION SYSTEM FOR REDUCED GRAVITY
CONDITIONS

ABSTRACT

Containerized plant production under reduced gravity conditions (i.e., 0g) is crucial for sustaining astronauts' well-being during extended space exploration. However, previous plant cultivation studies in space yielded mixed results, highlighting challenges in understanding porous media hydraulic properties (water retention characteristics) and fluid transport mechanisms (matric potential and gravitational potential) under reduced gravity. These challenges hinder precise fluid delivery through the root zone. This study addresses challenges, particularly over-irrigation in the root zone, faced by past plant cultivation in reduced gravity. Notably, the VEGGIE system in orbit, which pioneered the non-powered passive capillary-driven irrigation system, encountered these challenges. We presented a potential solution, the plant-optimal irrigation system incorporating the determination of target water status based on the hysteretic water retention characteristics of growth porous media. The plant-optimal irrigation system comprised key components, including 1) hydraulic potential regulation using a check valve connected to 2) a water reservoir with a Mariotte bottle and 3) containerized porous media with three different particle size ranges of aggregated calcined clay: Profile (0.25–1.0 mm), Turface (1.0–2.0 mm) and Mix (0.25–2.0 mm). Target matric potential (h_t) values of $h_t = -9.1$, -5.1 and -9.8 cm, based on the hysteretic water retention characteristics of each porous medium, were

determined to achieve 60% effective saturation ($0.6S_e$) during a total of 60 days of consecutive plant cultivation experiments with romaine lettuce ('Outrageous'). The proposed innovation introduced a check valve to the irrigation system, creating an automated 'plant-optimal' mechanism that adapts to reduced gravity, preventing over-irrigation challenges while compensating for the lack of gravitational potential in the Mariotte bottle under Earth gravity conditions. While this work established the foundation for plant-optimal irrigation, further validation and exploration of check valve characteristics were recommended for practical long-term plant production both on Earth and in reduced gravity conditions.

1. INTRODUCTION

Extraterrestrial containerized plant production holds significant promise for supporting astronauts' dietary and mental well-being during long-term space exploration (Haeuplik-Meusburger et al., 2014). NASA's initiation of the Ohalo III Crop Production System in 2019 aims to prototype crop production systems for extended space missions, specifically testing water delivery systems and volume optimization concepts under reduced gravity conditions (i.e., 0g) (Johnson et al., 2021). Simultaneously, containerized plant production on Earth (at 1g) within controlled environments, such as greenhouses and residential households, is gaining traction due to increasing concerns related to food and water security (Fields et al., 2021).

Advancements in containerized crop production systems, both on Earth and in orbit, involve automation in managing canopy environments (light, humidity, temperature) and root zone fluid delivery (water, oxygen, nutrients) with a focus on reducing labor time and resources. Recent advancements in plant growth modules aboard the International Space

Station (ISS), including the Advanced Plant Habitat (APH) system (Monje et al., 2020) and the VEGGIE system (Massa et al., 2017), range from active pumping systems and passive capillary-driven systems. The APH system employed a similar irrigation approach used in past plant cultivation experiments, including ADVASC (Link et al., 2003) and BPS (Morrow and Crabb, 2000), utilizing an active pumping system while monitoring the root zone water status for scheduled or manually operated irrigation. The VEGGIE system was the first to employ a non-powered, passive capillary-driven irrigation approach. It utilized a root pillow filled with a porous medium, which had one side interfacing with a water reservoir through a wicking material (Massa et al., 2017). However, the VEGGIE system faced challenges with excess water and poor root zone aeration (Massa et al., 2017; Monje et al., 2020).

The capillary-driven irrigation system is a simple and traditional approach to maintaining water status in the root zone under Earth's gravity conditions. For example, a prototype of the VEGGIE system under Earth gravity by Stutte et al. (2011) successfully demonstrated plant cultivation. However, understanding the hydrodynamics within porous media becomes imperative, especially when transitioning between Earth's gravity and reduced gravity conditions. Hydrodynamics in porous media is influenced by surface and capillary forces acting against Earth's gravitational force, while surface and capillary forces are dominant under reduced gravity. To illustrate this concept, consider how tissue paper absorbs water after being submerged in water. The wetting front travels upward through the paper fiber matrix in response to capillarity, which diminishes as the water climbs higher above the water surface. The balancing act between Earth's gravity force and the capillary and surface forces of the tissue paper matrix eventually limits the height to which

water climbs, resulting in a partially saturated tissue. However, under reduced gravity, water imbibition into tissue paper is not restrained by gravity, resulting in saturated tissue paper. This same phenomenon may explain variations in hydrodynamics leading to excess water levels using the capillary-driven irrigation system under reduced gravity conditions.

The hydraulic properties of porous media, especially the water retention characteristics, also play a crucial role in hydrodynamics. The water retention character is essential in various disciplines such as soil science, hydrology and engineering, because it defines the porous media's volumetric water content (θ) and hydraulic energy state, namely matric potential (h), under both saturated and unsaturated conditions. The water retention characteristic depends on the pore size distribution of the porous medium and the properties of air, water and solid interfaces (Hillel, 1998). The hysteretic water retention character, which manifests differently during drying and wetting processes (Pham et al., 2005), is particularly essential in plant production. This understanding becomes crucial as evapotranspiration and irrigation subject the porous media to alternating drying and wetting processes. Studies have shown that the hysteretic water retention character of porous media on Earth applies similarly under reduced gravity conditions (Heinse et al., 2005, 2007, 2015).

This research proposed and evaluated a simple passive water status management approach for reduced gravity to achieve target volumetric water content (θ_t) and/or target matric potential (h_t) values in plant growth media. Those target values were based on the hysteretic water retention character of the growth medium. The proposed innovation involves the installation of a spring-loaded check valve connected between the water reservoir and the porous medium, creating an automated 'plant-optimal' irrigation system.

The check valve installation under Earth's gravity was previously implemented by Jones and Or (1998a), maintaining negative h within a containerized sand while growing wheat. This system operates without sensing the water status (i.e., moisture sensor) or actively pumping water into the porous media. A check valve enables one-way fluid transport based on the pressure gradient between the inlet and outlet. This threshold pressure in the check valve compensates for the lack of gravitational potential under reduced gravity conditions, which should prevent over-irrigating the root zone. Additionally, by choosing check valves with different opening pressures, each container of growth medium can be operated at different matric potential control points, even if connected to the same reservoir. This variability can be tailored to match each porous medium's hydraulic properties and potentially the plant's water requirements. Our research objective was to demonstrate plant cultivation using the plant-optimal irrigation system under Earth's gravity conditions. Further discussions address the potential application of this system under reduced gravity conditions.

2. THEORETICAL

2.1 Hydraulic Potential Components

The foundational hydrodynamics of porous media involve key components: volumetric water content (θ in $\text{cm}^3 \text{ cm}^{-3}$), matric potential (h in cm), pressure potential (p in cm), gravitational potential (z in cm) and hydraulic potential (H in cm). Water in porous media experiences combined potential energies known as hydraulic potential, denoted as $H = h + p + z$ (cm). This encompasses matric, pressure and gravitational potentials. Note that the terms h and p are mutually exclusive, and a negative value of h represents the unsaturated condition in the porous media, while a positive value of p represents saturated

porous media. The z term varies based on the vertical position relative to the reference position ($z = 0$ cm), which is often set at the surface or bottom of the porous media container. In this study, we set the reference $z = 0$ cm at the bottom of the porous media container.

2.2 Water Retention Model

The water retention and unsaturated hydraulic conductivity models, initially derived on Earth, can also be applied to reduced gravity conditions (Heinse et al., 2005, 2007, 2015). These models can be mathematically computed using the widely adopted models developed by van Genuchten (1980):

$$S_e = \frac{\theta(h) - \theta_r}{\theta_s - \theta_r} = \left[\frac{1}{1 + (\alpha|h|)^n} \right]^m \quad (1)$$

$$K(h) = K_s S_e^l \left[1 - (1 - S_e^{1/m})^m \right]^2 \quad (2)$$

where S_e is the effective saturation (-), θ_s and θ_r are the volumetric water content values ($\text{cm}^3 \text{cm}^{-3}$) at saturation and residual condition, respectively. The parameter α influences both water retention and unsaturated hydraulic conductivity curve shape and is commonly considered equivalent to the reciprocal of the air-entry potential of the porous medium. Two other curve shape parameters, m and n , are related to the pore size distribution, with m often calculated as $m = 1 - 1/n$. The K_s parameter represents the saturated hydraulic conductivity (cm d^{-1}), and the term l is a pore connectivity parameter (-), typically estimated as $l = 0.5$ by Mualem, (1976). The initial setup of the plant cultivation experiments involved a drying process, and the calculation to obtain the target matric potential (h_t) and volumetric water content (θ_t) represented this drying process.

3. MATERIALS AND METHODS

3.1 Porous Media Selection and Preparation

In the context of reduced gravity, coarse-textured granular porous media, namely aggregated calcined clay have been employed as the traditional porous media (Heinse et al., 2015). Calcined clay can be autoclaved to minimize the risk of bacteria and fungus growth (Yendler, 1998). These materials generally have a coarse and narrow particle size range, thus facilitating a managed θ at a relatively small h range (Jones et al., 2012). Calcined clay from Profile Products LLC, Buffalo Grove, IL has been used as the plant growth porous medium for a number of space-based applications (Morrow and Crabb, 2000; Link et al., 2003; Heinse et al., 2005, 2007, 2015; Massa et al., 2017; Monje et al., 2020). Three different particle size ranges have been targeted: Profile (0.25–1 mm), Turface (1–2 mm), and a mixture of Profile and Turface, Mix (0.25–2 mm, Turface: Profile = 1v: 1v) as shown in Figure 1. The physical properties including particle density (ρ_s), bulk density (ρ_b) and porosity ($\varphi = 1 - \rho_b / \rho_s$) along with the hysteretic water retention parameters, have been comprehensively studied (Heinse et al., 2007; Dixon et al., 2023), and are listed in Table 1. Calcined clay exhibits two primary pore structures: inter-aggregate and intra-aggregate pores. Given the necessity for a larger control range of h to prevent plant root drought stress in controlled environments (Lieth and Oki, 2019), our study focused on the hydraulic properties within the inter-aggregate pore region, corresponding to the h range of $-25 < h < 0$ cm.

Error! Reference source not found.c illustrates the experimental setup of the plant-optimal irrigation system. Each porous medium (Profile, Turface, and Mix) was packed into a plastic column with a diameter of 10.8 cm and a height of 10 cm (volume of

916 cm³). The bottom of each column was glued to a corrugated plastic sheet. The reference elevation ($z = 0$ cm) was set at the bottom of the containerized growth media. The center of the cylindrical porous cup was placed in the middle of the porous media ($z = 5$ cm), and it was used to supply water (+nutrient solution) to each porous medium. A pressure transducer (PX-40-50GHG5V, +/- 67 cm, Omega Engineering) was installed between the check valve and the porous cup with a 3-way stopcock to monitor the h value in the middle of the porous media. The pressure transducers provided ± 0.1 cm of precision measurements in the porous media's h . **Error! Reference source not found.** exhibited the top-down view of the setup of containerized porous media, showing the pressure transducer installation.

Air-dried Surface, Profile, and Mix were packed into containers with each ρ_b value shown in Table 1, using the air-Multiple Sieve Pluviation (MSP) method discussed in Dixon et al. (2023). The MSP method facilitated random particle scattering to provide a consistent ρ_b value (Miura and Toki, 1982), providing high reproducibility of ρ_b of the coarse-textured granulated porous media. A major difference between the air-MSP method described in Dixon et al. (2023) and our study was the use of a larger diameter funnel of 10.2 cm to facilitate particle scattering in a larger packing column (i.e., 10.8 cm), which was twice as large as the diameter of the column (i.d. = 5.1 cm) used in Dixon et al. (2023). We packed the granular porous media to fill about 4 cm in height of the container and then installed the air stone to position the center of the air stone at 5 cm height in the center of the container. After installing the air stone, the same packing method was used to fill the gap between the container wall and the air stone.

3.2 Plant-Optimal Irrigation System

The essential components of the plant-optimal irrigation system in **Error! Reference source not found.c** included 1) an irrigation reservoir filled with the modified Hoagland nutrient solution (solution EC of 1 dS m^{-1}), which consisted of two tubing as an air-inlet and a siphon through an air-tight rubber stopper, acting as a Mariotte bottle (Mccarthy, 1934; Holden, 2004), 2) a spring-loaded in-line check valve (SCV08053, Nordson Medical) with air-entry hydraulic potential (H_{cv}) of $H_{cv} = 9.1 \pm 0.8 \text{ cm}$, and 3) a porous cup (Air Stone Cylinder, Pawfly) with a diameter of 1.5 cm and a height of 2.5 cm, as a subsurface irrigation emitter with the air-entry potential value of $60 \pm 6.5 \text{ cm}$ installed in the middle of porous media ($z = 5 \text{ cm}$) with an elbow fitting. These components were connected with black tubing filled with the nutrient solution. The black tubing prevented algae growth in the tubing by minimizing light exposure. The air-inlet tubing in the Mariotte bottle was at constant atmospheric pressure ($h = 0 \text{ cm}$), creating a constant hydraulic potential between the Mariotte bottle and the inlet of the check valve. The end of the siphon was hydraulically connected to the check valve and the pressure transducer and terminated with the air stone. One water reservoir was connected to six containers of Profile and Mix, and another water reservoir was connected to three containers consisting of Turface.

3.3 Check Valve Characterization

Error! Reference source not found.d illustrates an enlarged illustration of the check valve and its mechanism of opening/closing. The check valve consists of a disk and a spring, allowing water to flow one way (i.e., left to right, in **Error! Reference source not found.d**) through the valve. Blue- and red-solid lines represent the inlet- and outlet-pressure of the check valve, H_i and H_o , respectively. Blue dashed lines represent the

threshold hydraulic potential of opening the valve (H_{cv}), countered by the difference between H_i and H_o . The H_i value was set as a constant value adjusted by the position of the air inlet level in Mariotte's bottle; therefore, the H_i value can be negative or positive. The H_o value, however, was maintained at a negative value to create the unsaturated condition for the experiment.

To open the valve and allow water to flow through the check valve, the potential difference between the inlet- and outlet-valve, $H_i - H_o$, has to overcome the spring force of the check valve, H_{cv} , i.e., $H_i - H_o > H_{cv}$, as shown in the upper image in **Error! Reference source not found.**d. The $H_i - H_o$ value diminishes once the valve opens, and when the valve falls below H_{cv} (i.e., $H_i - H_o \leq H_{cv}$), the spring closes the valve. Before the plant cultivation experiments, we determined the H_{cv} value in all check valves by creating a positive pressure gradient between the inlet and outlet of the check valves with Mariotte's bottle.

3.4 Target Water Content and Matric Potential Values for Plant Cultivation Experiment

We aimed to maintain both adequate water transport and adequate gas exchange, settling on 60% of the effective saturation condition ($0.6S_e$) in the middle of the porous media during the plant cultivation experiment. The target volumetric water content (θ_t) was solved by taking the left side of van Genuchten's model (Equation $S_e = \frac{\theta(h) - \theta_r}{\theta_s - \theta_r} =$

$$\left[\frac{1}{1 + (\alpha|h|)^n} \right]^m \quad (1) \text{ as } 0.6S_e. \text{ The target matric}$$

potential (h_t) value was computed by rearranging Equation $S_e = \frac{\theta(h) - \theta_r}{\theta_s - \theta_r} = \left[\frac{1}{1 + (\alpha|h|)^n} \right]^m$

(1 for h and substituting the θ_t value. Computed θ_t

and h_t values in each porous medium are listed in Table 1. Since we prepared for the

saturated porous media and drained to achieve the θ_t and h_t values, we used the drying process water retention as the primary water retention character to compute S_e , θ_t , and h_t values. However, we also demonstrated the θ_t , and h_t values using the wetting process of water retention characteristics in Table 1.

3.5 Gravimetric Potential of the Mariotte Bottle Outlet for the Plant-Optimal Irrigation System

We combined hydraulic potential components (i.e., z , h , p) of the plant-optimal irrigation system including porous media, check valve and the water reservoir to determine the air-inlet elevation position of the Mariotte bottle, which corresponded to the z value in the water reservoir since the air-inlet is exposed to the atmospheric condition ($h = 0$ cm). Table 2 **Error! Reference source not found.** shows example values of potential components in the plant-optimal irrigation system under Earth gravity conditions. All gravitational potentials were referenced to the bottom of the containerized growth media ($z = 0$ cm). The porous cup positioned in the middle of the porous media (i.e., Profile) ($z = 5$ cm) was aimed to provide the h_t value (i.e., $h_t = -9.8$ cm, Table 1). The check valve was positioned at the top of the container ($z = 10$ cm) with hydraulic contact to the porous media, therefore the outlet of the check valve should maintain a matric potential (h_o) value of -14.8 cm. Since the system is a quasi-hydrostatic condition, both H values in the middle of the porous media and the outlet of the check valve should be the same value at $H_o = -4.8$ cm. However, the H_{cv} value of 9.1 cm regulates the hydraulic potential gradient between the inlet and outlet; therefore, the inlet of the check valve exhibited $H_i = H_o + H_{cv} = -4.8 + 9.1 = 4.3$ cm, which led to $h_i = -5.7$ cm. Again, the H_i values and the Mariotte bottle must be equal under hydrostatic conditions and the h value at the air-inlet tube is at the

atmospheric pressure ($h = 0$ cm). Finally, the vertical position of the air-inlet tube in the Mariotte bottle was equivalent to the Mariotte bottle gravitational potential (z_m) value of $z_m = 4.3$ cm. Here we simplified the calculation of z_m as follows:

$$z_m = h_t + z_t + H_{cv} \quad (3)$$

where z_t represents the gravitational potential of the porous cup in the porous media ($z_t = 5$ cm). We computed the z_m value of each porous medium based on h_t and H_{cv} values and listed those in Table 2 **Error! Reference source not found.**

3.6 Plant Cultivation Experiment

As shown in **Error! Reference source not found.a**, the surface of the container was covered by a disk with two holes (diameter of 3 cm) to prevent mineral precipitation buildup from nutrient solution due to evaporation. All porous media were initially saturated with Hoagland nutrient solution ($EC = 1 \text{ dS m}^{-1}$) and then drained using an external stainless-steel tube vertically inserted along the side of the container wall. A rapid drainage stopped when the measured h values in the middle of the container approached $h = -5$ cm. This corresponded to the hydrostatic equilibrium condition where the bottom of the container showed saturation ($h = 0$ cm) and the h value showed a linear decrease as the gravitational potential increased towards the surface of the container. This procedure was conducted before placing seeds in the porous media on Day 0 and Day 30, providing the same initial water distribution in the containers for two consecutive cultivation experiments.

Three red Romaine lettuce seeds (cv. ‘Outrageous’) were placed on the surface of the growth media where the holes in the surface disk were located (**Error! Reference source not found.**). Each container had two holes at the surface, therefore a total of six

lettuce seeds were sown in each porous media. After the emergence of the first leaves, a seedling in each hole (two seedlings per container) was selected for the growth experiment. If the seedlings were too small or did not emerge, new seedlings separately sown on a wet paper towel on the same sowing day were transplanted.

The light source provided $227 \pm 7.3 \mu\text{mol m}^{-2} \text{s}^{-1}$ of photosynthetic photon flux density (PPFD) at the surface of plant leaves was applied for 16 hours (5 pm to 9 am), and the height of the light source was adjusted as plants grew to maintain at least 10 cm distance from the light source to the surface of the top leaves. The water level of each Mariotte bottle was also monitored by the pressure transducer to remind us to refill the nutrient solution when the water level was low (less than 10 cm). All pressure transducers were connected to a datalogger CR1000X (Campbell Scientific, Logan UT) to monitor the sample h at 5 cm depth and the remaining water level in each Mariotte bottle every 10 seconds and collect the 1-minute moving average of measurements. All pressure transducers were calibrated before the plant cultivation experiment using hanging tubing filled with water to create positive and negative hydraulic potential ranging from -70 to 70 cm. A linear regression between the hydraulic potential value and the voltage output in each pressure transducer was individually optimized using the calibrated offset and slope values.

Disinfection between tubing and connections (i.e., manifolds and three-way cock) to prevent biofilm clogging was conducted in the second trial of the third and fourth weeks by injecting 4% hydrogen peroxide solution and flushing the solution with Hoagland nutrient solution. Biofilm buildup in irrigation lines is a common phenomenon in plant production and it has the potential to reduce the water flow through the tubing due to

biofilm blockage (Elasri and Miller, 1999; Lee and Lee, 2015; van Os et al., 2021). Since the O₂ gas is released when hydrogen peroxide reacts with biofilms, the trapped gas between the tubing was removed after the disinfection process by injecting the nutrient solution.

4. RESULTS

4.1 Target Matric Potential of Porous Media and the Gravitational Potential in Mariotte's Bottle

Error! Reference source not found.a-3c show the hysteretic water retention of Profile, Turface, and Mix using the hysteretic water retention model parameters (Equation 1) listed in Table 1. Solid and dash-dotted lines represent the drying and wetting water retention curves, respectively. Since particle size-range and -distribution substantially alter water retention characteristics, the coarse-textured and narrower particle size range of Turface (i.e., 1–2 mm) exhibits a water retention curve with smaller air-entry potential and steeper slopes compared to relatively finer-textured Profile and Mix. The θ_t and h_t were computed using the drying water retention curve, and each pair of θ_t and h_t values was listed in Table 1 and exhibited in Figure 3a, 3b and 3c in Profile, Turface and Mix, respectively. The θ_t values in all porous media exhibited θ_t between 0.56 and 0.57 cm³ cm⁻³, while the h_t values in Profile, Turface, and Mix exhibited -9.8, -5.1, and -9.1 cm, respectively. Coarser-textured Turface showed greater h_t values compared to the values in finer-textured Profile and Mix.

Table 3 shows the air-inlet position (z_m) value of the Mariotte bottle and the potential components used to compute z_m including h_t and the average value of threshold

hydraulic potential (H_{cv}) in individual check valves using Equation 3 for Profile, Turface, and Mix, respectively. Since Profile and Mix required similar z_m values of 3.8 and 3.5 cm, respectively, these porous media were connected to the same Mariotte bottle, therefore we set the z_m value of 3.7 cm. The greater h_t value ($h_t = -5.1$ cm) in Turface led to the greater value of z_m ($z_m = 7.3$ cm) compared to the z_m values ($z_m = 3.7$ cm) in Profile and Mix.

4.2 Diurnal Matric Potential Measurements in Porous Media

Error! Reference source not found.d–3f present the average h measurements in triplicated porous media, Profile, Turface and Mix, over the initial 30 days and the subsequent 30 days (a total of 60 days) of cultivation experiments. The horizontal axis denotes the time after the first sowing. Black solid lines depict average h values from triplicated measurements, while light blue circles indicate daily averages with gray vertical bars representing standard deviation values. Blue dotted lines represent determined h_t value based on drying water retention parameters (refer to **Error! Reference source not found.**a–3c and Table 1).

All porous media began from saturation, draining excess water to reach semi-container capacity ($h = -5$ cm in the middle of the container). Consequently, h values in all porous media exhibited a rapid decrease during the first week of both cultivation periods. The star (*) symbols in **Error! Reference source not found.**d–3f mark h spikes caused by manual maintenance, including the replacement of pressure transducers, repriming water lines and cleaning the biofilm buildup with H_2O_2 solution.

Diurnal fluctuations in h (black solid lines in **Error! Reference source not found.**d–3f) were observed, with decreasing h during the photoperiod (drying process) due to facilitated evapotranspiration and increasing h during the dark period (non-photoperiod)

(wetting process) caused by water redistribution and/or irrigation. Water level measurements in the Mariotte bottle indicated a substantial decrease about 10 days after both cultivations, suggesting water redistribution contributed initially, later dominated by plant-optimal irrigation due to increasing evapotranspiration from plant growth.

The plant-optimal irrigation system effectively maintained h near h_t , however, the daily average and the standard deviation values from triplicated h measurements (light blue circles and gray bars in **Error! Reference source not found.d–3f**) show temporary and individual fluctuations, ranging from 0.095 to 5.3 cm. Fluctuations in h measurements were likely a combination of precision in each pressure transducer and varied H_{cv} values in the individual check valve (Table 3).

Although the plant-optimal irrigation ensured automatic h control, manual maintenance was required weekly. Accumulation of trapped air in the tubing between the check valve and the porous cup potentially disconnects the hydraulic connection to the growth media, leading to decreased h values in some of the containers. Therefore, re-priming in Turface (on Day 15 and 21 in **Error! Reference source not found.e**) and Mix (on Day 21 in **Error! Reference source not found.Figure 3f**) was necessary. We suspect this accumulation of trapped air was a combination of the released dissolved air in irrigation water and trapped air in the porous cup.

Other spikes in h measurements occurred during the replacement of pressure transducers (on Day 37 in Profile and Mix, **Error! Reference source not found.d and 3f**) and cleaning (on Day 47 and 54 for all containers in **Error! Reference source not found.d–3f**). During the cleaning process with H_2O_2 solution, we observed the gas release from tubing connected to containers, caused by the oxidation process of organic matter

(i.e., biofilm), effectively eliminating biofilm buildup. Incorporating cleaning solutions into the maintenance procedure is crucial, especially for preventing bacterial biofilm buildup in irrigation practice.

4.3 Lettuce Yield in Porous Media

Table 4 shows the average and standard error values of leaf dry mass (g cm^{-2}) in Profile, Turface, and Mix after the 30 days of two cultivation trials. The surface area of the container was 86.6 cm^2 . The dry mass for the first trial ranged between 0.030 and 0.036 g cm^{-2} , while slightly increased dry mass for the second trial ranging between 0.047 and 0.053 g cm^{-2} was observed. However, both trials exhibited insignificant yield differences. All porous media showed similar dry mass across the trials.

5. DISCUSSION

In this study, we demonstrated the plant-optimal irrigation system, which combined check valve pressure regulation and a water reservoir (the Mariotte bottle) maintaining a near-constant hydraulic potential to manage the root zone h . Initially, we determined the h_i value to achieve 60% of S_e ($0.6S_e$) based on the drying process of water retention characteristics of three different pore sizes of aggregated calcined clay: Profile (0.25–1 mm), Turface (1–2 mm), and Mix (0.25–2 mm). We also proposed a simple equation (Equation 2) to calculate the air-entry tube position (z_m) in the Mariotte bottle relative to the reference level ($z = 0 \text{ cm}$) of the bottom of the growth media to maintain the h_i in porous media with the plant-optimal irrigation system, accounting for gravimetric, matric, pressure and water potentials in each component (i.e., porous media, check valve). An example of the plant-optimal irrigation system is illustrated in **Error! Reference source**

not found.c and the potential components are demonstrated in Table 2. The study demonstrated successful consecutive romaine lettuce cultivations while maintaining the porous media's h .

5.1 Check Valve Characteristics

Although we monitored the h value in the middle of the container, specifically between the porous cup and the check valve, additional pressure monitoring between the water reservoir and the check valve would allow us to provide further information about when the check valve opened and closed, as well as the pressure gradient between the inlet and outlet of the check valve during the cultivation periods. We assumed that each check valve exhibited a constant H_{cv} value throughout the consecutive plant cultivation experiment for 60 days, however, further study is needed to understand how the check valve's opening/closing mechanism corresponds to the diurnal change of evapotranspiration.

Characterizing the individual H_{cv} values of the check valve is crucial for precisely designing the plant-optimal irrigation and maintaining the h_t value. The significant variability observed in the H_{cv} value of check valves, indicated by the standard deviation value of 2.1 cm (Table 3), impacted the regulation of h values in different growth media such as Profile and Mix, despite these porous media being connected to the same Mariotte bottle (with the same H value).

The variability in the H_{cv} value of check valves should be considered when selecting growth media. Porous media with a wide range of particle size distribution (e.g., peat moss) exhibit a gradual slope in water retention (data now shown), suggesting that small changes in h values would have negligible effects on altering θ value. However, porous media with

a narrow range of particle size distribution such as aggregated calcined clay (e.g., Profile) exhibited a steep slope in water retention (see Figure 3a), indicating that minor variation in h values (e.g., ± 2 cm) can substantially change the θ values. For example, controlling the h value at -9 ± 2 cm in Profile resulted in θ values ranging from 0.49 and 0.70 $\text{cm}^3 \text{cm}^{-3}$ based on the water retention parameters during the drying process (see Figure 3a).

5.2 Potential Applications to Optimize the h_t value

While we did not focus on determining the optimal h_t value to maximize plant yield, we note that h_t values can be optimized based on the porous media's physical and hydraulic characteristics (i.e., hysteretic water retention) as well as the water requirement in different varieties of plants. Jones and Or (1998b) pointed out that the selection of porous media is typically based on the available materials rather than focused on the physical- and hydraulic-properties. Raviv et al. (2004) suggested choosing an optimal irrigation control once the adequate porous media choice has been made. As calcined clay exhibited substantial hysteresis in water retention models, selecting the proper water retention model, either the drying- or wetting-process, to calculate h_t critically affects plant growth, as Wallach (2008) mentioned. Among the three different particle size ranges and their distribution of particle size, Turface exhibited a steeper water retention slope, potentially leading to challenges in maintaining the target water status (i.e., θ_t and h_t) in the porous media's profile.

5.3 The Plant-optimal Irrigation System under Reduced Gravity Conditions

The plant-optimal irrigation system demonstrated in this Earth-based experiment was designed specifically for plant production under reduced gravity conditions. Table 5

shows the comparison of the porous media's h control under Earth gravity with the Mariotte bottle (i.e., capillary-driven irrigation) and the h control under reduced gravity using the check valve (i.e., plant-optimal irrigation). The Mariotte bottle's mechanism relies on the gravitational potential of the air-entry tube, which doesn't apply under reduced gravity conditions due to a lack of gravitational potential. However, the check valve's opening/closing mechanism, dependent on the threshold water pressure H_{cv} , can compensate for Earth's gravitational potential induced by the Mariotte bottle under reduced gravity.

6. CONCLUSIONS

In this study, we introduced a novel irrigation system, termed plant-optimal irrigation, showcasing its application for the passive irrigation system under reduced gravity with three distinct particle size ranges: Profile (0.25–1 mm), Turface (1–2 mm), and Mix (0.25–2 mm). The plant-optimal irrigation system conducted in Earth's gravity was designed with three components: a) an air stone serving as a subsurface irrigation emitter within the porous media, b) a Mariotte bottle ensuring constant pressure in the water reservoir and most notably, c) a check valve installed between the water reservoir and porous media providing additional regulation of the porous media's matric potential (H_{cv}). The integration of a check valve between the water line facilitated automated one-way irrigation by dynamically opening/closing the check valve based on the hydraulic potential (H) gradient between the inlet and outlet, exceeding the threshold potential (average $H_{cv} = 9.1 \pm 2.3$ cm). This system demonstrated an efficient irrigation approach operating without an active pumping system. The plant-optimal irrigation system features underscore the

cost-effectiveness under Earth and reduced gravity conditions, emphasizing its potential for sustainable plant production. Successful implementation of the plant-optimal irrigation system necessitates an understanding of fundamental porous media physical principles, encompassing water-, gravitational- and matric-potentials, along with the hysteresis exhibited in porous media water retention characteristics. To enhance the applicability of the system to Earth-based scenarios, we proposed a simple equation for calculating the air-entry tube position (z_m) in the Mariotte bottle. This equation considers the gravimetric and matric potentials of each component (i.e., check valve and porous media). Furthermore, the same equation can be applied to reduced gravity conditions by simply assigning a zero value to the gravitational potential. We determined the h_t by analyzing the drying process of water retention characteristics across three pore sizes of aggregated calcined clay: Profile (0.25–1 mm), Turface (1–2 mm), and Mix (0.25–2 mm). The check valve, linked to each containerized porous medium, provided flexible control over matric potential (h), even when connected to the same water reservoir with a consistent hydraulic potential value. This adaptability allows tailoring to the hydraulic properties of the porous media and potentially aligning with the specific water requirements of different plants. While our work has established the foundation for incorporating check valves into the water line for plant-optimal irrigation, further validation of check valve characteristics—especially concerning diurnal evapotranspiration requirements—will enhance the practicality of long-term plant production, both on Earth and in orbit.

REFERENCES

Dixon, C., Sheng, W., Zhou, R., Horton, R., and Jones, S. B. (2023). Thermal property standards using granular media with air-pluviation and heat pulse probe measurements. *Agric For Meteorol* 330, 109303. doi: 10.1016/J.AGRFORMET.2022.109303

Elasri, M. O., and Miller, R. V. (1999). Study of the Response of a Biofilm Bacterial Community to UV Radiation. *Appl Environ Microbiol* 65, 2025–2031. doi: 10.1128/AEM.65.5.2025-2031.1999

Fields, J. S., Owen, J., Lamm, A., Altland, J. E., Jackson, B. E., Zheng, Y., et al. (2021). Soilless substrate science: a North American needs assessment to steer soilless substrate research into the future. *Acta Horti*, 313–318. doi: 10.17660/ACTAHORTIC.2021.1317.36

Haeuplik-Meusburger, S., Paterson, C., Schubert, D., and Zabel, P. (2014). Greenhouses and their humanizing synergies. *Acta Astronaut* 96, 138–150. doi: 10.1016/j.actaastro.2013.11.031

Heinse, R., Humphries, S. D., MacE, R. W., Jones, S. B., Steinberg, S. L., Tuller, M., et al. (2005). Measurement of porous media hydraulic properties during parabolic flight induced microgravity. SAE International. doi: 10.4271/2005-01-2950

Heinse, R., Jones, S. B., Or, D., Podolskiy, I., Topham, T. S., Poritz, D., et al. (2015). Microgravity Oxygen Diffusion and Water Retention Measurements in Unsaturated Porous Media aboard the International Space Station. *Vadose Zone Journal* 14, vzj2014.10.0135. doi: 10.2136/vzj2014.10.0135

Heinse, R., Jones, S. B., Steinberg, S. L., Tuller, M., and Or, D. (2007).

Measurements and Modeling of Variable Gravity Effects on Water Distribution and Flow in Unsaturated Porous Media. *Vadose Zone Journal* 6, 713–724. doi: 10.2136/vzj2006.0105

Hillel, D. (1998). *Environmental soil physics: Fundamentals, applications, and environmental considerations*.

Holden, J. (2004). “Mariotte Bottle—Use in Hydrology,” in *Water Encyclopedia*, (Wiley), 503–504. doi: 10.1002/047147844X.pc380

Johnson, C. M., Boles, H. O., Spencer, L. S. E., Poulet, L., Romeyn, M., Buncek, J. M., et al. (2021). Supplemental Food Production With Plants: A Review of NASA Research. *Frontiers in Astronomy and Space Sciences* 8, 198. doi: 10.3389/FSPAS.2021.734343/BIBTEX

Jones, S. B., and Or, D. (1998a). A capillary-driven root module for plant growth in microgravity. *Advances in Space Research* 22, 1407–1412. doi: 10.1016/S0273-1177(98)00215-4

Jones, S. B., and Or, D. (1998b). Design of Porous Media for Optimal Gas and Liquid Fluxes to Plant Roots. *Soil Science Society of America Journal* 62, 563–573. doi: 10.2136/sssaj1998.03615995006200030002x

Jones, S. B., Or, D., Heinse, R., and Tuller, M. (2012). Beyond Earth: Designing Root Zone Environments for Reduced Gravity Conditions. *Vadose Zone Journal* 11. doi: 10.2136/vzj2011.0081

Lee, S., and Lee, J. (2015). Beneficial bacteria and fungi in hydroponic systems: Types and characteristics of hydroponic food production methods. *Sci Hortic* 195, 206–215. doi: 10.1016/j.scienta.2015.09.011

Lieth, J. H., and Oki, L. R. (2019). Irrigation in Soilless Production. *Soilless Culture: Theory and Practice Theory and Practice*, 381–423. doi: 10.1016/B978-0-444-63696-6.00009-8

Link, B. M., Durst, S. J., Zhou, W., and Stankovic, B. (2003). Seed-to-seed growth of *Arabidopsis Thaliana* on the international space station. *Advances in Space Research* 31, 2237–2243. doi: 10.1016/S0273-1177(03)00250-3

Massa, G. D., Dufour, N. F., Carver, J. A., Hummerick, M. E., Wheeler, R. M., Morrow, R. C., et al. (2017). VEG-01: Veggie hardware validation testing on the international space station. *Open Agric* 2, 33–41. Available at: <https://www.degruyter.com/document/doi/10.1515/opag-2017-0003/html> (Accessed May 16, 2021).

Mccarthy, E. L. (1934). Mariotte's Bottle. *Science (1979)* 80, 100.

Miura, S., and Toki, S. (1982). A Sample Preparation Method and its Effect on Static and Cyclic Deformation-Strength Properties of Sand. *Soils and Foundations* 22, 61–77. doi: 10.3208/SANDF1972.22.61

Monje, O., Richards, J. T., Carver, J. A., Dimapilis, D. I., Levine, H. G., Dufour, N. F., et al. (2020). Hardware Validation of the Advanced Plant Habitat on ISS: Canopy Photosynthesis in Reduced Gravity. *Front Plant Sci* 11, 673. doi: 10.3389/FPLS.2020.00673/BIBTEX

Morrow, R. C., and Crabb, T. M. (2000). Biomass Production System (BPS) plant growth unit. *Advances in Space Research* 26, 289–298. doi: 10.1016/S0273-1177(99)00573-6

Mualem, Y. (1976). A new model for predicting the hydraulic conductivity of

unsaturated porous media. *Water Resour Res* 12, 513–522. doi: 10.1029/WR012i003p00513

Pham, H. Q., Fredlund, D. G., and Barbour, S. L. (2005). A study of hysteresis models for soil-water characteristic curves. <https://doi.org/10.1139/t05-071> 42, 1548–1568. doi: 10.1139/T05-071

Raviv, M., Wallach, R., and Blom, T. J. (2004). THE EFFECT OF PHYSICAL PROPERTIES OF SOILLESS MEDIA ON PLANT PERFORMANCE - A REVIEW. *Acta Hortic*, 251–259. doi: 10.17660/ActaHortic.2004.644.34

Stutte, G. W., Newsham, G., Morrow, R. M., and Wheeler, R. M. (2011). Concept for sustained plant production on ISS using VEGGIE capillary mat rooting system., in *41st International Conference on Environmental Systems 2011, ICES 2011*. doi: 10.2514/6.2011-5263

van Genuchten, M. Th. (1980). A Closed-form Equation for Predicting the Hydraulic Conductivity of Unsaturated Soils 1. *Soil Science Society of America Journal* 44, 892–898. doi: 10.2136/sssaj1980.03615995004400050002x

van Os, E. A., Stijger, C. C. M. M., and Breeuwsma, S. J. (2021). Investigating the potential risk for accumulation of cleansing products in closed soilless culture systems. *Acta Hortic*, 55–62. doi: 10.17660/ActaHortic.2021.1321.8

Wallach, R. (2008). “Physical characteristics of soilless media,” in *Soilless Culture: Theory and Practice*, (Elsevier), 41–116. doi: 10.1016/B978-044452975-6.50005-8

Yendler, B. (1998). Preliminary evaluation of soil moisture probe for use with arcillite. *Advances in Space Research* 22, 1419–1423. doi: 10.1016/S0273-1177(98)00216-

Table 1. Physical properties including particle size distribution, particle density (ρ_s), bulk density (ρ_b) and the computed porosity ($\varphi = 1 - \rho_b / \rho_s$) and hysteretic water retention parameters for the van Genuchten (1980) model and the computed target volumetric water content (θ_t) and matric potential (h_t) in Profile, Turface and Mix.

			Profile	Turface	Mix
Physical Properties					
Particle size distribution		mm	0.25–1	1–2	0.25–2
Particle density [†]	ρ_s	g cm^{-3}	2.52	2.52	2.52
Bulk density	ρ_b	g cm^{-3}	0.63	0.64	0.69
Porosity ($\varphi = 1 - \rho_b / \rho_s$)	φ		0.75	0.75	0.73
Hydraulic properties					
Drying process					
VG model parameters [‡]	θ_r	$\text{cm}^3 \text{ cm}^{-3}$	0.34	0.34	0.32
	θ_s	$\text{cm}^3 \text{ cm}^{-3}$	0.72	0.73	0.72
	α	cm^{-1}	0.099	0.19	0.11
	n		7.7	5.6	3.9
Computed parameters	θ_t	$\text{cm}^3 \text{ cm}^{-3}$	0.57	0.57	0.56
	h_t	cm	–9.8	–5.1	–9.1
Wetting process					
VG model parameters [‡]	θ_r	$\text{cm}^3 \text{ cm}^{-3}$	0.34	0.34	0.32
	θ_s	$\text{cm}^3 \text{ cm}^{-3}$	0.69	0.68	0.64
	α	cm^{-1}	0.19	0.32	0.17
	n		4.4	4.1	2.9
Computed parameters	θ_t	$\text{cm}^3 \text{ cm}^{-3}$	0.55	0.54	0.51
	h_t	cm	–5.2	–3.1	–6.2

[†]Dixon et al. (2023), [‡]Heinse et al. (2007)

Table 2. Potential components of the plant-optimal irrigation system comprised of the porous cup in the media, the check valve ($H_{cv} = 9.1$ cm) and the water reservoir under Earth's gravity condition. Note that the reference gravitational potential ($z = 0$ cm) was set at the bottom of the containerized growth media.

	Gravitational potential z (cm)	Matric potential or pressure potential h or p (cm)	Hydraulic potential H (cm) = $z + h + p$
Porous cup	$z_t = 5$	$h_t = -9.8$	-4.8
Check valve outlet	10	$h_o = -14.8$	-4.8
Check valve inlet	10	$h_i = H_i - z_i = -5.7$	$H_i = H_o + H_{cv} = 4.3$
Mariotte bottle air-inlet	$z_m = 4.3$	Atmospheric = 0	4.3

Table 3. Target matric potential (h_t) computed from the drying water retention character, the threshold hydraulic potential to open the check valve (H_{cv}) with the standard error value and the air-inlet tube position (z_m) in the Mariotte's bottle computed with Equation 3 in Profile, Turface and Mix.

	Target matric potential h_t	Check valve opening H_{cv}	Air-inlet position z_m
	cm	cm	cm
Profile	-9.8	8.6±1.6	3.8
Turface	-5.1	7.4±1.7	7.3
Mix	-9.1	7.6±1.7	3.5

Table 4. The average- and standard error-values of dry leaf mass per unit area (g cm^{-2}) in Profile, Turface and Mix.

	1st trial	2nd trial
	g cm^{-2}	g cm^{-2}
Profile	0.034 ± 0.010	0.053 ± 0.018
Turface	0.030 ± 0.013	0.050 ± 0.016
Mix	0.036 ± 0.0046	0.047 ± 0.027

Table 5. Comparison of potential components of (a) the conventional Mariotte bottle irrigation system without the check valve under Earth's gravity condition and (b) the plant-optimal irrigation system with the check valve under reduced gravity (0g) condition as illustrated in **Error! Reference source not found.**

	Gravitational potential z (cm)	Matric potential or pressure potential h or p (cm)	Hydraulic potential H (cm) = $z + h + p$
(a) Earth gravity (1g) + Mariotte bottle (Conventional)			
Porous cup	5	-9.8	-4.8
Mariotte bottle air-inlet	-4.8	0	-4.8
(b) Reduced gravity (0g) + check valve ($H_{cv} = 9.1$ cm)			
Porous cup	0	-9.8	-9.8
Check valve outlet	0	-9.8	-9.8
Check valve inlet	0	-0.7	-0.7
Water reservoir	0	-0.7	-0.7



Figure 1. Calcined clay with three different particle size ranges: Profile (0.25-1 mm),

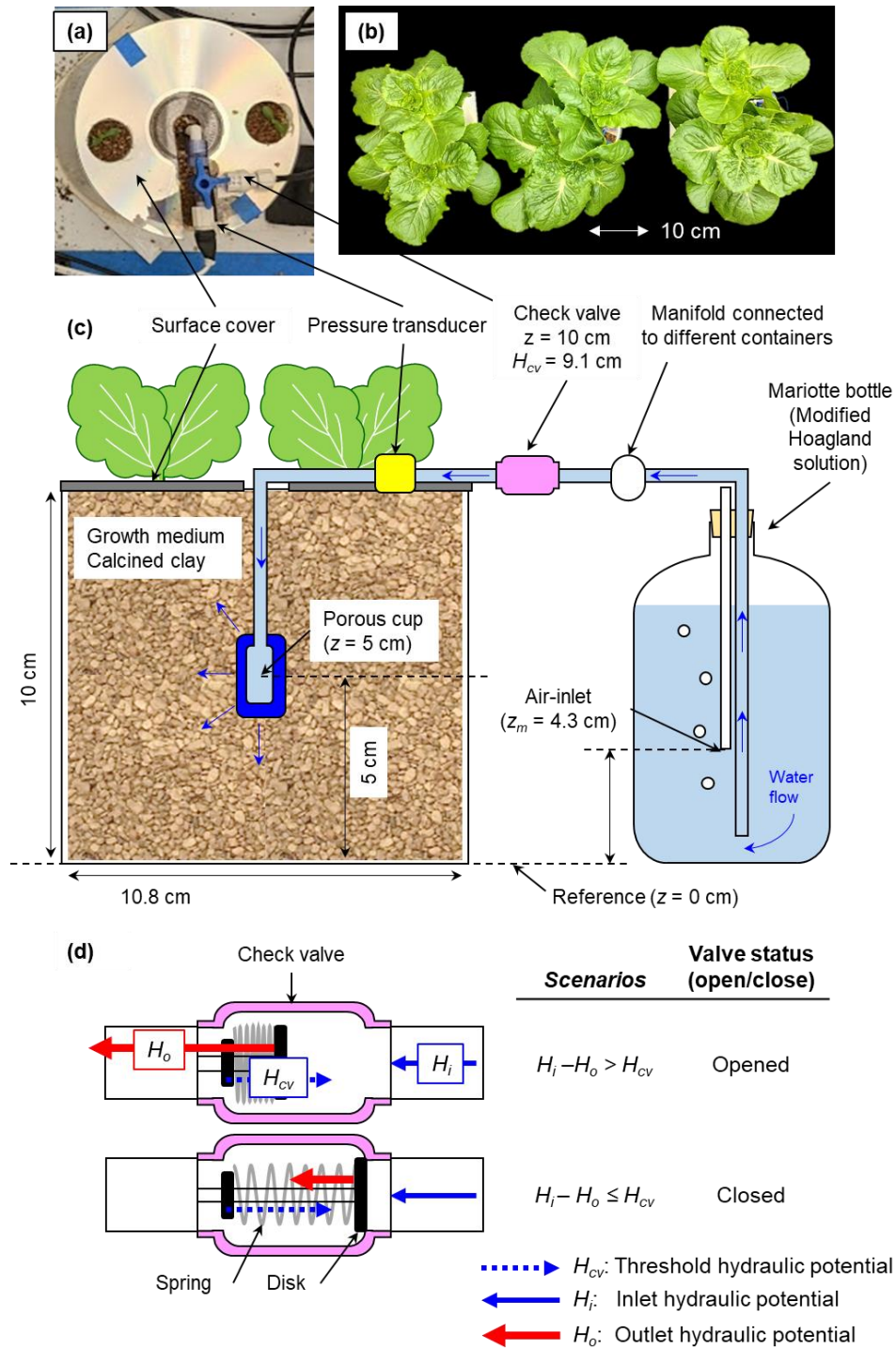


Figure 2. (a) A top-down picture and (c) an illustration demonstrating the plant-optimal irrigation system with (b) Romaine lettuce cultivation. The key components included: Plant growth medium, a check valve, and a Mariotte bottle water reservoir with (d) an enlarged illustration of the check valve demonstrating the opening/closing mechanism of the valve with the threshold potential (H_{cv}) to open the valve as well as the inlet (H_i) and the outlet (H_o) hydraulic potentials.

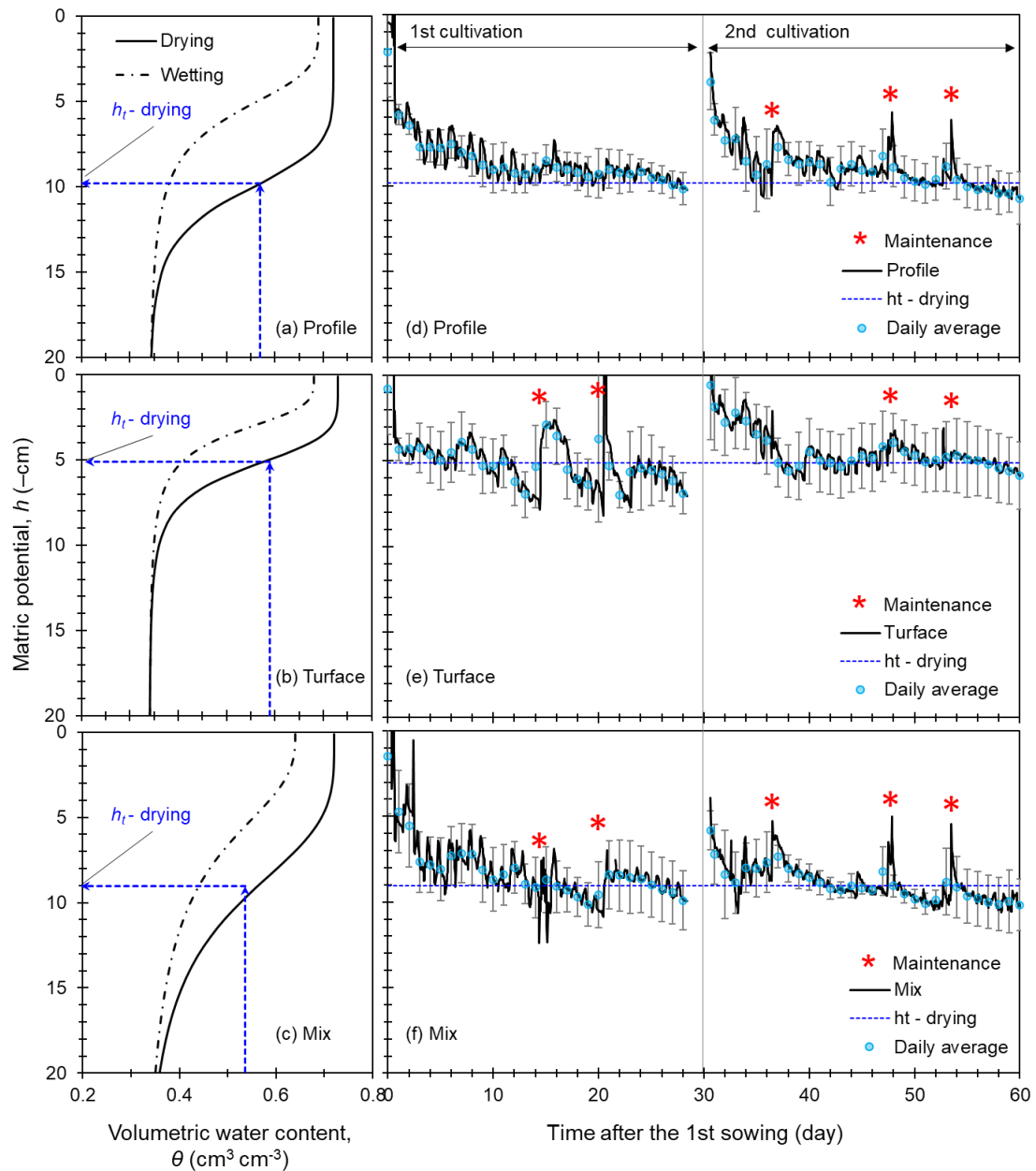
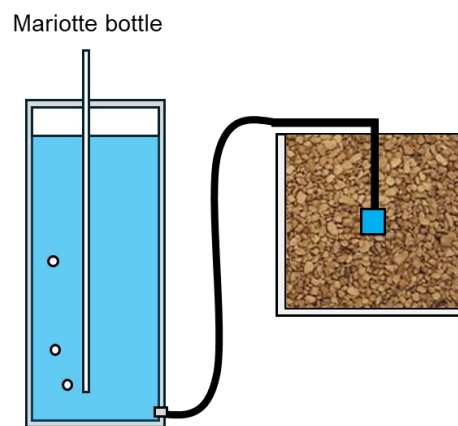


Figure 3. Water retention curve for the drying (solid lines) and wetting (dash-dotted lines) processes in (a) Profile, (b) Surface and (c) Mix using the VG model parameters listed in Table 1, and the total 60 days of diurnal changes in the averaged value of triplicated matric potential (h) measurements at $z = 5$ cm (black solid lines), and the target matric potential (h_t) values (blue dash lines) and daily average value of h measurements (light blue circles) with the gray bars showing the standard deviation in (d) Profile, (e) Surface and (f) Mix. Note that the star symbol (*) represents the manual maintenance including replacing pressure transducers, repriming the water lines and cleaning the biofilm buildup with H_2O_2 solution.

(a) Earth gravity (1G)



(b) Reduced gravity (0G)

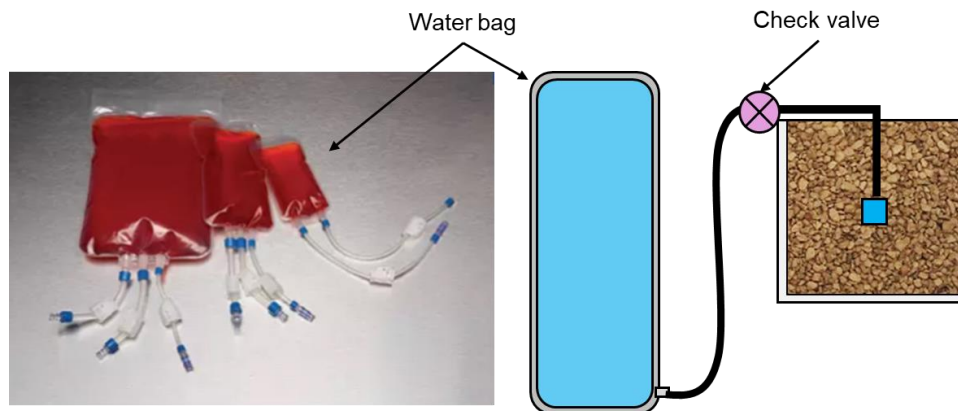


Figure 4. The illustration of the comparison between (a) the capillary-driven irrigation using the Mariotte bottle under Earth gravity and (b) the plant-optimal irrigation using the check valve and collapsible water reservoir.

CHAPTER VII

CONCLUSION

The successful implementation of plant production systems under microgravity is crucial for supporting long-term human space exploration. This necessitates a thorough assessment and validation of various components involved in the root zone sensing technique and our understanding of the hydrodynamics of the root zone, including growth media and interfaces.

In Chapter 2, our objective was to enhance thermal property estimation using a Heat Pulse Probe (HPP) calibration in air-free ice. The sharper peak temperature rise curve observed in air-free ice compared to traditional calibration media, agar-stabilized water, facilitated the optimization of temperature analysis models, such as the Infinite Cylindrical Perfect Conductor (ICPC) model. This calibration method holds promise in future plant growth experiments under reduced gravity as the heat pulse method was the only option decades ago and remains a viable option where electromagnetic interference remains a concern for space-based applications. Beyond space applications, thermal properties serve as surrogate determinations for monitoring a variety of soil properties and processes including heat flux, water flux, and water content.

Building upon the findings of Chapter 2, Chapter 3 showcased various granular media with highly reproducible bulk density, offering a wide range of water content-dependent thermal properties from oven-dry- to saturated-conditions. The reproducible bulk density preparation using the air-pluviation method can also ensure consistent bulk density when preparing containerized plant growth media.

In Chapter 4, we introduced an automated system for hanging water column measurements, employing a combination of diffuse laser distance sensing, linear actuators, and a high-resolution pressure transducer. This system, coupled with model fitting using existing water retention models, enables repeatable hysteretic water retention measurements for coarse-textured media within a typical controlled range of matric potential for plant growth.

Using the automated water retention measurements discussed in Chapter 4, we characterized the hysteretic water retention of synthetic and natural fibers as potential plant growth media in Chapter 5 and successfully demonstrated plant growth using containerized synthetic fibers. The findings revealed that lightweight fibrous media exhibited higher porosity and similar water retention characteristics to traditional horticultural media such as peat moss. This similarity in water retention characteristics between fabric and peat moss could be advantageous in distributing fluids (water, dissolved nutrients, and gas) when constructing the layered root zone using fabric and peat moss.

In Chapter 6, we demonstrated a passive irrigation system and emphasized optimization for containerized growth media's matric potential control based on hysteretic water retention curves. The development and validation of a passive irrigation system using a Mariotte bottle connected to a check valve were highlighted, showing its effectiveness in maintaining target matric potential values for plant growth. The study also highlighted the potential application of installing the check valves in the capillary-driven irrigation system under reduced gravity conditions. The spring-loaded check valve opening pressure, coupled with a matching porous membrane, maintains an operational matric potential within the root zone at virtually any gravity level without the need for powered pumps or

valves.

In this research, we focused on the accessibility of media (e.g., solid ice, granular media, and fabrics) and their preparation methodology to provide highly reproducible results. Although all media we provided were commercially available, the local availability of material highly influenced the selection of calibration media and plant growth media. For example, the process of creating air-free ice was found to be time-consuming and required a larger freezer, which could be a constraint in selecting the calibration media. Material selection for growth media in the International Space Station (ISS) includes additional requirements such as fire-resistance and food safety qualifications, which could limit the use of some of the fabrics.

Designing plant growth modules for long-term space missions poses a significant dilemma: while the ultimate tests occur in space, the initial evaluation must take place on Earth, where gravity influences root zone hydrodynamics. Looking ahead, the development of adaptable and inexpensive long-term plant growth experiments to simulate reduced gravity conditions on Earth is essential for advancing plant production systems in space exploration missions.

In conclusion, this research significantly contributes to the advancement of plant production systems under microgravity conditions. By enhancing our understanding of root zone dynamics and developing innovative techniques for thermal property estimation and water retention measurement, we pave the way for more sustainable and efficient plant cultivation in space. These findings not only hold promise for supporting long-term human space exploration but also have implications for terrestrial agriculture, driving innovation and progress in both fields.

APPENDICES

Appendix A CR-Basic Program for the Automated Hanging Water Column

Below is a CR-Basic program used in the automated hanging water column measurement.

'CR1000 Series Datalogger

```
'=====
=====
'
'                               MEASUREMENT PARAMETERS                               '
'=====
====='
```

```
*****
*****
```

'Sample Properties:

Public SAMPLE_HEIGHT = 8 'Height of sample from plate (mm)

Public SAMPLE_RADIUS = 37.5 'Radius of sample (mm)

Public QS = 0.95 'Qs (assume 1)

```
*****
*****
```

'Movement Parameters:

Const LA7_DISTANCE_DOWN = 50 'Distance to move LA7 down each step (mm)

Const LA7_DISTANCE_UP = 50 'Distance to move LA7 up each step (mm)

Public LA7_LOWER_LIMIT = 700 'Lower limit of LA7 movement (mm)

Const LA7_UPPER_LIMIT = 0 'Upper limit of LA7 movement (mm)

Const TURNAROUND_VALUES = 3 'Number of consecutive Theta values to look for TURNAROUND_CHANGE

Const TURNAROUND_CHANGE = 0.005 'Change in Theta to trigger turnaround (% in fraction)

Const CYCLES = 12 'Number of times to execute entire up&down measuring process

'Equilibrium Parameters:

Const VARIATION = 0.056 'Max variation for water equilibrium (cm)

Const EQ_TIME = 60 'Time for moving average to smooth measurements for equilibrium (sec)

```

Const EQ_TIME_MAX = 60*60  'Max time to wait for water equilibrium (sec)
Const EQ_WINDOW = 300    'Window to determine water equilibrium (sec)

'=====
=====
' * Ensure that LA1 and LA7 are both in their zero positions before beginning the
program * '
' * Send to logger to begin the program * Use Reset flag to stop the program early *
,

'=====
=====

```

'Declare Data Tables

```
DataTable(Table1,True,-1)    'Data table to store data for monitoring
```

```
Sample(1,SAMPLE_HEIGHT,FP2)
```

```
Sample(1,SAMPLE_RADIUS,FP2)
```

```
Sample(1,QS,FP2)
```

```
Sample(1,Counter,FP2)
```

```
Sample(1,LA7_Current_Pos,FP2)
```

```
Sample(1,LA7_cm,IEEEE4)
```

```
Sample(1,Sample_cm,IEEEE4)
```

```
Sample(1,Plate_cm,IEEEE4)
```

```
Sample(1,Reflector_cm,IEEEE4)
```

```
Sample(1,Pipette_cm,IEEEE4)
```

```
Sample(1,z_cm,IEEEE4)
```

```
Sample(1,Pressure_cm,IEEEE4)
```

```
Sample(1,OutflowL_cm,IEEEE4)
```

```
Sample(1,Volume_mL,IEEEE4)
```

```
Sample(1,Theta,IEEEE4)
```

```
EndTable
```

```
DataTable(Table2,True,-1)  'Data table for monitoring EQ
```

```
Sample(1,EQ_Pressure,IEEEE4)
```

```

Sample(1,EQ_Avg(1),IEEEE4)
Sample(1,EQ_Avg(EQ_WINDOW),IEEEE4)
Sample(1,FiveEQ,IEEEE4)
Sample(1,LA7_Direction,FP2)
EndTable

```

```
'Declare Constants
```

```

Const LA1_DIRECTION_PORT = 7 'Control port for LA1 direction control
Const LA1_PULSE_PORT = 8 'Control port for LA1 step control
Const LA1_MAX_POS = 11500 'Maximum distance of LA1 (pulses)
Const LA1_PULSE_PER_MM = 100
'[1rev/4mm]x[200steps/rev]x[2pulses/step]=400pulses/4mm = 100pulses/mm
Const ZERO = 0 'Zero distance value (used with LA1 & LA7 positions)
Const LA7_UP_PORT = 5 'Control port for LA7 up
Const LA7_DOWN_PORT = 4 'Control port for LA7 down
Const LA7_MAX_POS = 700 'Maximum distance of LA7 (mm)
Const SAFETY_PORT = 6 'Control port to disconnect manual switch
Const LASER_DIST_PORT = 15 'SE port for laser distance output
Const LASER_SWITCH_PORT = 3 'VX port for laser switching
Const UP = 0 'Flag used for upward measuring
Const DOWN = 1 'Flag used for downward measuring
Const PRESSURE_PORT = 9 'SE port for pressure transducer

```

```
'Declare Public Variables
```

```

Public SAMPLE_VOLUME 'Calculate volume of sample in mL
Public Water_Volume 'Calculate water volume of sample in mL
Public Counter 'Keeps track of main measurement executions
Public Last_Cycle As Boolean = FALSE 'Allows extra step down on last cycle
Public Reset As Boolean = 0 'Flag used to stop program and reset LA1
Public Index 'Reusable for For loops
'LA1

```

```

Public LA1_Target_Pos      'LA1 desired position (pulses)
Public LA1_Current_Pos    'LA1 current position (pulses)
Public LA1_Current_Pos_mm 'LA1 current position (mm)
Public Stop(4) = {88,113,52,ZERO} 'LA1 stops (mm) - Reflector=88, Pipette=113,
Plate=52, ZERO=0
'LA7
Public LA7_Target_Pos      'LA7 desired position (mm)
Public LA7_Current_Pos    'LA7 current position (mm)
Public LA7_Direction      'LA7 direction to move
Public LA7_Distance       'LA7 distance to move (mm)
Public LA7_Mov_Dir        'LA7 direction tracker for movement
Public LA7_Mov_mm         'LA7 movement control (mm)
'Turnaround
Public LA7_Mov_CP         'LA7 movement current position (mm)
Public Bottom_VWC(TURNAROUND_VALUES) 'Array to hold past pressure
readings to check for turnaround
Public Turnaround_Count = 0 'Counter for pressure readings within turnaround
change
Public Reverse As Boolean = FALSE 'Flag to reverse LA7 before reaching lower
limit
'Equilibrium
Public EQ_Pressure        'Distance measurements for determining EQ
Public EQ_Avg(EQ_WINDOW) 'Time window for determining EQ
Public FiveEQ            'EQ value determined
Public Pressure_cm       'Pressure measurement (cm)
Public Too_Long As Boolean = False 'Will be true if EQ reaches max time before
equilibrium
'Moving Average
Public Mov_Av_Array(EQ_TIME) 'Array to hold moving average values
Public Mov_Av            'Moving average
Public Mov_Av_Count      'Used to calculate moving average
Public Mov_Av_Reset As Boolean = FALSE 'Flag to reset moving average array
'Laser Measurements
Public LA7_cm            'True position of LA7 (cm)

```

```

Public Plate_mm      'Position of plate (mm)
Public Plate_cm      'Position of plate (cm)
Public Reflector_mm  'Position of reflector(mm)
Public Reflector_cm  'Position of reflector (cm)
Public Reflector_Start_mm  'Starting position of reflector, used to reference LA7
movement (mm)
Public Pipette_mm    'Position of water level in pipette (mm)
Public Pipette_cm    'Position of water level in pipette (cm)
Public Sample_mm     'Position of sample (mm)
Public Sample_cm     'Position of sample(cm)
'Theta Calculations
Public z_mm          'Distance between reflector and plate (mm)
Public z_cm          'Distance between reflector and plate (cm)
Public Volume_mL     'Change in water volume in pipette (mL)
Public OutflowL_cm   'Outflow length (cm)
Public Theta         'VWC of sample

'Define Functions
Function MoveLA1(pos) 'Function to move LA1
    LA1_Target_Pos = (pos * LA1_PULSE_PER_MM)          'Get the desired
position
    While (LA1_Target_Pos < LA1_Current_Pos AND LA1_Target_Pos >= ZERO)
'While desired position is < current position and >= 0
        PortSet(LA1_DIRECTION_PORT,1)                'Set direction +
        PortSet(LA1_PULSE_PORT,0)                    'Pulse motor
        Delay(0,10,uSec)                              'Each pulse takes 10uS
        PortSet(LA1_PULSE_PORT,1)                    'Stop pulsing motor
        LA1_Current_Pos = LA1_Current_Pos - 1        'Update current
position
        LA1_Current_Pos_mm = LA1_Current_Pos / 100   'Convert current
position to mm
    Wend
    While (LA1_Target_Pos > LA1_Current_Pos AND LA1_Target_Pos <=
LA1_MAX_POS) 'While desired position is > current position and <= max position

```

```

PortSet(LA1_DIRECTION_PORT,0)           'Set direction -
PortSet(LA1_PULSE_PORT,0)               'Pulse motor
Delay(0,10,uSec)                         'Each pulse takes 10uS
PortSet(LA1_PULSE_PORT,1)               'Stop pulsing motor
LA1_Current_Pos = LA1_Current_Pos + 1    'Update current
position
    LA1_Current_Pos_mm = LA1_Current_Pos / 100    'Convert
current position to mm
Wend
EndFunction

Function MoveLA7    'Function to move LA7
If (LA7_Direction = DOWN)                'If moving down
    LA7_Target_Pos = LA7_Mov_CP + LA7_Distance    'Increase target position
Else                                       'If moving up
    LA7_Target_Pos = LA7_Mov_CP - LA7_Distance    'Decrease target position
EndIf

If (Reset)                                'If reset button pushed
    LA7_Target_Pos = 0                    'Override target position to be 0
EndIf

If (LA7_Target_Pos > LA7_Mov_mm)          'If target position lower than current
position
    PortSet(SAFETY_PORT,1)                'Disconnect manual switch
    PortSet(LA7_DOWN_PORT,1)              'Turn on LA7 down port
    LA7_Mov_Dir = DOWN                    'Track direction as down
ElseIf (LA7_Target_Pos < LA7_Mov_mm)      'If target position higher than
current position
    PortSet(SAFETY_PORT,1)                'Disconnect manual switch
    PortSet(LA7_UP_PORT,1)                'Turn on LA7 up port
    LA7_Mov_Dir = UP                       'Track direction as up
EndIf
Do                                         'Loop

```

```

VoltSe(LA7_Mov_mm,1,mV5000,LASER_DIST_PORT,1,0,_60Hz,0.60436834,0)
'Measure Laser
    LA7_Mov_mm -= Plate_mm                'Use offset to find
position
    If (LA7_Mov_Dir = UP AND LA7_Mov_mm <= LA7_Target_Pos)      'If
moving up and at or past target position
        ExitDo                'Exit Loop
    ElseIf(LA7_Mov_Dir = DOWN AND LA7_Mov_mm >= LA7_Target_Pos)
'If moving down and at or past target position
        ExitDo                'Exit loop
    EndIf
Loop
PortSet(LA7_DOWN_PORT,0)        'Turn off LA7 down port
PortSet(LA7_UP_PORT,0)         'Turn off LA7 up port
LA7_Mov_CP = LA7_Target_Pos    'Set LA7 current position
PortSet(SAFETY_PORT,0)        'Reconnect manual switch
LA7_cm = -LA7_Mov_mm/10        'Change true position to negative and
to cm for display
    LA7_Current_Pos = -LA7_Mov_CP/10    'Change position to negative and
cm for display
EndFunction

Function MeasureLaser 'Function to take a laser distance measurement
    Dim dist, lav
    Scan (10,mSec,0,100)
    VoltSe(dist,1,mV5000,LASER_DIST_PORT,1,0,_60Hz,0.60436834,0) 'Measure
Laser
    AvgRun (lav,1,dist,100)        'Average measurements
    NextScan
    Return lav                    'Return averaged measurement
EndFunction

Function MovingAverage(tobeav) 'Function to calculate moving average

```

```

Dim mind
If (Mov_Av_Reset)           'If reset flag
  Mov_Av_Array() = 10000    'Reset moving average to 10000
EndIf
Mov_Av = 0                  'Reset moving average
Mov_Av_Count = 0           'Reset moving average count
Mov_Av_Array(1) = tobeav   'Assign current value to first slot of
moving average array
For mind = 1 To EQ_TIME Step 1 'For size of moving average
  If (Mov_Av_Array(mind) <> 10000) 'If element in array has been
initialized
    Mov_Av += Mov_Av_Array(mind)    'Accumulate
    Mov_Av_Count += 1              'Increase element counter
  EndIf
Next mind
Mov_Av /= Mov_Av_Count          'Divide sum by number of elements
For mind = EQ_TIME - 1 To 1 Step -1
  Mov_Av_Array(mind + 1) = Mov_Av_Array(mind) 'Shift array
Next mind
EndFunction

```

```

Function ResetProgram 'Function to reset actuators and exit program
  If (Reset)
    MoveLA1(Stop(1)) 'Move laser to reflector
    MoveLA7()        'Put LA7 back to zero
  EndIf
  MoveLA1(Stop(4))  'Move laser back to zero
  Exit              'End Program
EndFunction

```

```

Function MainMeasure 'Function to take ABCD measurements each movement
  Dim i, j, elapsed
  For i = 1 To 4 Step 1 'For each stop

```



```

If (Reset OR Reverse)          'If reset button pushed
  ExitFunction                  'Exit function
EndIf
MoveLA1(Stop(i))              'Move laser to stop
If (i = 1)                      'If stop #1
  MoveLA7()                    'Move LA7 one step
  EQ_Avg()=10000               'Initialize EQ window array
  Mov_Av_Reset = TRUE          'Reset moving average
  Timer(1,Sec,2)              'Start EQ timer
  "EQ"*****
  Scan(1,Sec,0,0)             'EQ Scan
  If (Reset)                   'If reset button pushed
    ExitFunction               'Exit Function
  EndIf
  elapsed = Timer(1,Sec,4)     'Check EQ running time
  VoltSe(EQ_Pressure,1,mv5000,PRESSURE_PORT,1,0,_60Hz,0.0142,1.1248)
'Measure pressure
  If (Mov_Av_Reset)           'If moving average reset flag true
    MovingAverage(EQ_Pressure) 'Find moving average
    If (elapsed > 5)          'After 5 values
      Mov_Av_Reset = FALSE    'Stop resetting
    EndIf
  Else
    MovingAverage(EQ_Pressure) 'Find moving average
    EQ_Avg(1) = Mov_Av        'Store current value in first slot of eq window
  EndIf
  CallTable Table2            'Call eq data table
  If (EQ_Avg(1) > (EQ_Avg(EQ_WINDOW)-VARIATION) AND EQ_Avg(1) <
(EQ_Avg(EQ_WINDOW)+VARIATION) AND EQ_Avg(1) <> 10000) 'If within
tolerance
    FiveEQ = EQ_Avg(1)        'Set FiveEQ
    ExitScan                  'Exit EQ scan
  ElseIf(elapsed >= EQ_TIME_MAX) 'If running too long

```

```

FiveEQ = EQ_Avg(1)      'Set FiveEq
Too_Long = True        'Set max time error
ExitScan               'Exit EQ scan
EndIf
For j=EQ_WINDOW-1 To 1 Step -1
    EQ_Avg(j+1) = EQ_Avg(j)    'Shift window array
Next j
NextScan               'Scan loops until EQ_TIME reached
Pressure_cm = EQ_Avg(1)    'Declare equilibrium
''''''''
Reflector_mm = MeasureLaser() 'Measure laser at reflector
Reflector_cm = Reflector_mm / 10 'Convert to cm
ElseIf (i = 2)
    Pipette_mm = MeasureLaser() 'Measure laser at pipette
    Pipette_cm = Pipette_mm / 10 'Convert to cm
ElseIf (i = 3)
    Plate_mm = MeasureLaser() 'Measure laser at plate
    Plate_cm = Plate_mm / 10 'Convert to cm
ElseIf (i = 4)
    Sample_mm = MeasureLaser() 'Measure laser at sample
    Sample_cm = Sample_mm / 10 'Convert to cm
EndIf
'VOLUME CALCULATIONS
Next i
z_cm = Plate_cm - Reflector_cm    'z is distance between plate and reflector
OutflowL_cm = Pressure_cm - z_cm    'Outflow length
Volume_mL = OutflowL_cm * 0.88    'Volume = outflow * 0.88
Theta = (WATER_VOLUME - Volume_mL) / SAMPLE_VOLUME 'VWC
calculation
EndFunction

Function FindBottom(rst As Boolean) 'Function to check for turnaround before lower
limit

```

```

If (rst)                'If reset flag is true
  Bottom_VWC() = 10000  'Reset bottom pressure array
  ExitFunction
EndIf

Turnaround_Count = 0    'Reset turnaround count

Bottom_VWC(1) = Theta  'Put current Theta in beginning of bottom pressure
array

  For Index = 2 To TURNAROUND_VALUES 'Check if consecutive Thetas are
  within turnaround change
    If (Bottom_VWC(Index) < Bottom_VWC(Index-1) + TURNAROUND_CHANGE
    AND Bottom_VWC(Index) > Bottom_VWC(Index-1) - TURNAROUND_CHANGE)
      Turnaround_Count += 1      'For each within change, increase counter
    EndIf
  Next Index

  If (Turnaround_Count = TURNAROUND_VALUES - 1) 'If all bottom pressure
  values are within change of each other
    Reverse = True              'Set flag to turn around
  Else                          'If all bottom pressure values are not within change
  of each other
    For Index=TURNAROUND_VALUES-1 To 1 Step -1  'Shift bottom pressure
    array
      Bottom_VWC(Index+1) = Bottom_VWC(Index)
    Next Index
  EndIf
EndFunction

'Main Program
BeginProg

  SAMPLE_VOLUME = (SAMPLE_HEIGHT * 3.141592 *
(SAMPLE_RADIUS^2))/1000

  Water_Volume = Sample_Volume * QS

  If (LA7_LOWER_LIMIT >= 680)      'LA7 lower limit capped at 680mm
    LA7_LOWER_LIMIT = 680
  EndIf

```

```

Counter = 0                'First round of measuring
LA1_Current_Pos = ZERO    'LA1 is at 0
LA1_Target_Pos = ZERO    'LA1 should be at 0
MoveLA1(Stop(3))        'Move LA1 to plate
Plate_mm = MeasureLaser() 'Find plate distance
Plate_cm = Plate_mm / 10  'Convert to cm
LA7_Current_Pos = ZERO    'LA7 is at 0
LA7_Mov_CP = ZERO        'LA7 is at 0
LA7_cm = ZERO            'LA7 is at 0
LA7_Target_Pos = ZERO    'LA7 should be at 0
LA7_Direction = DOWN     'LA7 should be moving down
LA7_Distance = 0         'Don't move LA7 for initial measurements
MainMeasure()           'Take initial measurements at zero
LA7_Distance = LA7_DISTANCE_DOWN 'Distance to move LA7 down
Scan(10,Sec,5,0)        'Main scan
    CallTable Table1     'save initial measurements
    If (LA7_Direction = DOWN) 'If LA7 is moving down
        FindBottom(FALSE) 'Check for early turnaround
    EndIf
    MainMeasure()        'Take 4 measurements
    If (Reset)           'If reset button pushed
        ResetProgram()   'Reset actuators and exit program
    EndIf
    If (((LA7_Mov_CP + LA7_DISTANCE_DOWN) > LA7_LOWER_LIMIT OR
Reverse) AND LA7_Direction = DOWN) 'If lower limit reached
        If (Last_Cycle)  'If this is the last cycle
            'Reset = TRUE    'Set to reset
            CallTable Table1
            ExitScan        'Exit main scan
        EndIf
        LA7_Distance = LA7_DISTANCE_UP 'Change LA7 distance
        LA7_Direction = UP    'Change LA7 direction

```

```

Reverse = FALSE           'Reset reverse flag
FindBottom(TRUE)        'Reset Bottom_VWC array
EndIf
If ((LA7_Mov_CP - LA7_DISTANCE_UP) < LA7_UPPER_LIMIT AND
LA7_Direction = UP) 'If upper limit reached
    CallTable Table1      'Record measurements
    Counter +=1          'Track 1 measurement cycle
    If (Counter = CYCLES) 'If max measurement cycles
        'ExitScan        'Exit main scan
        Last_Cycle = TRUE 'Do one more step down process
    EndIf
    LA7_Distance = 0     'Don't move LA7 for initial measurements
    MainMeasure()       'Take initial measurements at zero
    LA7_Distance = LA7_DISTANCE_DOWN 'Distance to move LA7 down
    LA7_Direction = DOWN 'LA7 should be moving down
    Reverse = FALSE     'Reset reverse flag
EndIf
NextScan
ResetProgram()          'Return LA1 to zero position
EndProg

```

APPENDIX B COAUTHOR APPROVAL LETTERS

Chihiro Dixon
Utah State University
Department of Plants, Soils and Climate
4820 Old Main Hill
Logan, UT 84322-4820
2024/4/1

Wenyi Sheng
Assistant Professor
Key Laboratory of Modern Precision Agriculture System Integration Research
Ministry of Education
China Agricultural University
Beijing 100083, China

Dear Dr. Wenyi Sheng,

I am in the process of preparing my dissertation in the plants, soils and climate department at Utah State University. I hope to complete my degree program in May 2024.

I am requesting your permission to include the papers we co-authored attached below. I will include acknowledgments and appropriate citations in these works and copyright and reprint rights information in a special appendix. The bibliographic citations will appear at the end of the manuscript as shown. Please advise me of any changes you require.

Please indicate your approval of this request by signing in the space provided, attaching any other form or instruction necessary to confirm permission. If you have any questions, please call me at the number below.

I hope you will be able to reply immediately.

Thank you for your cooperation,

You're sincerely,
Chihiro Dixon
801-441-8784

I hereby give permission to Chihiro Dixon to reprint the following materials in her dissertation.

Chihiro Naruke, Wenyi Sheng, Rong Zhou, Scott B. Jones, Standardizing Heat Pulse Probe measurements for thermal property determination using ice and water, *Agricultural and Forest Meteorology*, Volumes 308–309, 2021, 108610, ISSN 0168-1923, <https://doi.org/10.1016/j.agrformet.2021.108610>.

Chihiro Dixon, Wenyi Sheng, Rong Zhou, Robert Horton, Scott B. Jones, Thermal property standards using granular media with air-pluviation and heat pulse probe measurements, *Agricultural and Forest Meteorology*, 330, 2023, 109303, ISSN 0168-1923, <https://doi.org/10.1016/j.agrformet.2022.109303>.

Chihiro Dixon, Adam Blakeslee, Melanie Mills, Wenyi Sheng, Scott B. Jones, Automated hanging water column for characterizing water retention and hysteresis of coarse-textured porous media. *Soil Science Society of America Journal*, 87, 2023, 1474–1484, <https://doi.org/10.1002/saj2.20596>

A handwritten signature in black ink, appearing to read 'Wenyi Sheng', written in a cursive style.

Signed: _____

Chihiro Dixon
Utah State University
Department of Plants, Soils and Climate
4820 Old Main Hill
Logan, UT 84322-4820
2024/4/1

Robert Horton
Professor
Department of Agronomy
Iowa State University
Ames, IA 50011-1051

Dear Dr. Robert Horton,

I am in the process of preparing my dissertation in the plants, soils and climate department at Utah State University. I hope to complete my degree program in May 2024.

I am requesting your permission to include the paper we co-authored attached below. I will include acknowledgments and appropriate citations in this work and copyright and reprint rights information in a special appendix. The bibliographic citations will appear at the end of the manuscript as shown. Please advise me of any changes you require.

Please indicate your approval of this request by signing in the space provided, attaching any other form or instruction necessary to confirm permission. If you have any questions, please call me at the number below.

I hope you will be able to reply immediately.

Thank you for your cooperation,

You're sincerely,
Chihiro Dixon
801-441-8784

I hereby give permission to Chihiro Dixon to reprint the following material in her dissertation.

Chihiro Dixon, Wenyi Sheng, Rong Zhou, Robert Horton, Scott B. Jones, Thermal property standards using granular media with air-pluviation and heat pulse probe measurements, *Agricultural and Forest Meteorology*, 330, 2023, 109303, ISSN 0168-1923, <https://doi.org/10.1016/j.agrformet.2022.109303>.

Robert Horton

Signed: _____

CURRICULUM VITAE

Chihiro Dixon

(April 2024)

Dept. Plants, Soils and Climate
 College of Agricultural and Applied
 Sciences
 Utah State University
 Logan, UT 84322-4820

Home address:
 1651N 400E Apt. 611
 North Logan, UT 84341
 (801) 441-8784

EDUCATION

Ph.D. - Soil Science Utah State University Dissertation: "Designing, Sensing and Optimizing Porous Plant Growth Media for Reduced Gravity Applications"	2016-2024 Logan, UT
M.S. - Environmental science Mie University Dissertation: "Design, Sense and Optimize..."	2014-2016 Mie, JAPAN
B.S. - Environmental science Mie University	2010-2014 Mie, JAPAN

EXPERIENCE

Research Assistance Utah State University	2016-2024 Logan, UT
TA in Unsaturated Flow and Transport Utah State University	2021 Logan, UT
TA in Environmental Soil Physics Utah State University	2018, 2020 & 2022 Logan, UT
Student Tutor in Japanese Utah State University	2016-2020 Logan, UT
TA in Soil Physics Student Laboratory Experiments Mie University	2014-2016 Mie, JAPAN
TA in Basic Chemistry Mie University	2014 Mie, JAPAN
TA in Basic Statistics Mie University	2014 Mie, JAPAN

AWARDS

Grant A. Harris Fellowship METER group	2023 Pullman, WA
---	---------------------

1th place in the Soil Physics & Hydrology Division Student Competition	2022
ASA, CSSA & SSSA annual meeting	Baltimore, MD
USUSA Academic Opportunity Award	2022
Utah State University	Logan, UT
USU Graduate Student Travel Award	2022
Utah State University	Logan, UT
SSSA Robert Luxmoore Travel Award	2022
Utah State University	Logan, UT
AGRI Bertrand D. Tanner/Campbell Scientific Graduate Fellowship	2022
Utah State University	Logan, UT
Southard Soil Science Graduate Fellowship	2022
Utah State University	Logan, UT
1st place in Outstanding Student Presenters Mini-Award	2021
American Geophysical Union Fall Meeting	New Orleans, LA
4th place in the Soil Physics & Hydrology Division Student Competition	2021
ASA, CSSA & SSSA annual meeting	Salt Lake City, UT
College of Agriculture and Applied Sciences Graduate Student Travel Award	2021
Utah State University	Logan, UT
AGRI Bertrand D. Tanner/Campbell Scientific Graduate Fellowship	2021
Utah State University	Logan, UT
Best poster award at the PSC graduate student showcase	2021
Utah State University	Logan, UT
Best poster award	2015
Japanese Society of Soil Physics Annual Meeting	Okayama, JAPAN
Best poster award	2014
Japanese Society of Soil Physics Annual Meeting	Fukushima, JAPAN

PUBLICATIONS

- Dixon, C.**, Mills, M., Blakeslee, A., & Jones, S. B. 2024. A Plant-Optimal Irrigation System for Reduced Gravity Conditions. In process of submitting to *Frontiers in Astronomy and Space Sciences*
- Dixon, C.**, Blakeslee, A., Mills, M., Sheng W., & Jones, S. B. 2024. Characterizing Hysteretic Water Retention of Synthetic- and Natural-Fiber as Candidate Plant Growth Media. In process of submitting to *Soil Science Society of America*.
- Dixon, C.**, Blakeslee, A., Mills, M., Sheng W., & Jones, S. B. 2023. Automated hanging water column for characterizing water retention and hysteresis of coarse-textured porous media. *Soil Sci. Soc. Am. J.* doi: 10.1002/saj2.20596.
- Dixon, C.**, Sheng, W., Zhou, Horton, R., & Jones, S. B. 2023. Thermal property

standards using granular media with air-pluviation and heat pulse probe measurements, *Agricultural and Forest Meteorology*, 330, 2023, 109303, ISSN 0168-1923, <https://doi.org/10.1016/j.agrformet.2022.109303>.

Meng, F., Li, T., Sheng, W., Chung, C., **Dixon, C.**, Jones, S. B., Heat Pulse Probe Design Optimization Using Numerical Simulation. Accepted in *Geoderma*.

Naruke, C., Sheng, W., Zhou, R., & Jones, S. B. (2021). Standardizing Heat Pulse Probe measurements for thermal property determination using ice and water, *Agricultural and Forest Meteorology*, 308–309, 2021, 108610, ISSN 0168-1923, <https://doi.org/10.1016/j.agrformet.2021.108610>.

PRESENTATIONS

Dixon, C., Fatzinger, B., Bugbee, B., & Jones, S. B. (2023, November). Characterizing Hydraulic Properties of “Rooted” Plant Growth Substrates for Reduced Gravity Applications Using Hyprop and Ksat Systems. In ASA, CSSA, and SSSA International Annual Meetings. ASA-CSSA-SSSA.

Schreck, S., **Dixon, C.**, Fatzinger, B., Bingham, C., Bingham, G., Bugbee, B., & Jones, S. B. (2023, November). The Future of Plant Growth in Space: Sustaining Edible Crops on Manned-Missions to Mars. In ASA, CSSA, and SSSA International Annual Meetings. ASA-CSSA-SSSA.

Naruke, C., Fatzinger, B., Bugbee, B., & Jones, S. B. (2022, November). Numerical Simulation for Water and Plant Root Uptake under Various Gravity Conditions in Containerized Soilless Media. In ASA, CSSA, and SSSA International Annual Meetings. ASA-CSSA-SSSA.

Jones, S. B., **Naruke, C.**, Blakeslee, A., Fatzinger, B., & Bugbee, B. (2022, November). Plant Growth Porous Medium Design and Management Considerations for Reduced Gravity. In ASA, CSSA, and SSSA International Annual Meetings. ASA-CSSA-SSSA.

Naruke, C., Blakeslee, A., & Jones, S. B. (2021, December). Pore Space Dynamics and Oxygen Concentration in Containerized Porous Media. In AGU Fall Meeting 2021. AGU.

Naruke, C., Blakeslee, A., & Jones, S. B. (2021, December). Modeling Pore Space Dynamics from Root Growth in Porous Media. In AGU Fall Meeting 2021. AGU.

Jones, S. B., **Naruke, C.**, & Sheng, W. (2021, December). Standardizing Porous Media for Electromagnetic Water Content Sensor Evaluation, Calibration and Validation. In AGU Fall Meeting 2021. AGU.

Jones, S. B., A. Blakeslee, M. S. Mills & **C. Naruke.** (2021, December). Assessing the Significance of Hysteresis in Novel Porous Plant Growth Media. In AGU Fall Meeting 2021. AGU.

Naruke, C., Fatzinger, B., Bugbee, B., Blakeslee, A., & Jones, S. B. (2021, November). Impact of Root Growth on Water Retention and Hydraulic Properties in Containerized Soilless Media. In ASA, CSSA, and SSSA International Annual Meetings. ASA-CSSA-SSSA.

Naruke, C., Mills, M., Blakeslee, A., & Jones, S. B. (2021, November). Plant Growth in Candidate Media for Reduced Gravity Applications. In ASA, CSSA, and SSSA International Annual Meetings. ASA-CSSA-SSSA.

- Mills, M., **Naruke, C.**, & Jones, S. B. (2021, November). Characterizing Water Retention in Novel Soilless Media for Reduced Gravity Applications. In ASA, CSSA, and SSSA International Annual Meetings. ASA-CSSA-SSSA.
- Blakeslee, A., Mills, M., **Naruke, C.**, Sheng, W., & Jones, S. B. (2021, November). Automated Laser-Distance- and Pressure-Based Measurements for Characterizing Water Retention in Coarse Media. In ASA, CSSA, and SSSA International Annual Meetings. ASA-CSSA-SSSA.
- Jones, S. B., **Naruke, C.**, Chen, J., & Sheng, W. (2021, November). Standardizing Particulate Porous Media for Sensor Evaluation, Calibration and Validation. In ASA, CSSA, and SSSA International Annual Meetings. ASA-CSSA-SSSA.
- Fatzinger, B., **Naruke, C.**, Bugbee, B., & Jones, S. B. (2021, November). System for Precision Drought and Nutrient Stress. In ASA, CSSA, and SSSA International Annual Meetings. ASA-CSSA-SSSA.
- Naruke, C.**, Mills, M., Blakeslee, A., & Jones, S. B. (2021, October). Evaluation of Alternative Candidate Plant Growth Media for Reduced Gravity Applications. In Japanese Society of Soil Physics Annual Meeting. JSSP
- Naruke, C.**, Sheng, W., Zhou, R., Aoki, S., Kamai, T., & Jones, S. B. (2020, November). Standardizing Calibration and Testing Methodologies for Heat Pulse Probes in Agar-Stabilized Water and Air-Free Ice. In ASA, CSSA and SSSA International Annual Meetings (2020) VIRTUAL. ASA-CSSA-SSSA.
- Jones, S. B., Anderson, S. K., **Naruke, C.**, & Anderson, D. J. (2020, November). Thermo-Time Domain Reflectometry Commercialization: Progress, Problems and Future Plans. In ASA, CSSA and SSSA International Annual Meetings (2020) VIRTUAL. ASA-CSSA-SSSA.
- Naruke, C.**, & Jones, S. B. (2019, March). Numerical simulation of near-surface soil water and heat movement with different irrigation rate. In Spring Runoff Conference.
- Naruke, C.**, & Jones, S. B. (2019, March). What Do Numerical Simulations Tell Us about Accuracy of Traditional Soil Heat Flux Estimate?. In Department of Plant, Soils and Climate showcase.
- Naruke, C.**, Sheng, W., & Jones, S. B. (2019, November). Combining Near-Surface Estimates of Soil Heat and Evaporative Fluxes Using Heat Pulse and Dielectric Measurements. In ASA, CSSA, and SSSA International Annual Meetings. ASA-CSSA-SSSA.
- Naruke, C.**, Sheng, W., & Jones, S. B. (2019, November). Can Near-Surface Measurement and Modeling Predict Water and Heat fluxes? In ASA, CSSA, and SSSA International Annual Meetings. ASA-CSSA-SSSA.
- Jones, S. B., **Naruke, C.**, Sheng, W., Zhou, R., Sadeghi, M., Parajuli, K., ... & Tuller, M. (2019, January). Determination and Validation of Surface Soil Moisture Using Novel Gravimetric-, Dielectric-and Swir Reflectance-Based Approaches. In SSSA International Soils Meeting (2019). SSSA.
- Naruke, C.**, & Jones, S. B. (2018, October). Simulating the Impact of Evaporation on Soil Heat Flux. In Department of Plants, Soils and Climate Graduate student seminar.

- Naruke, C.** & Jones, S. B. (2017, October). Heat Flux Plate vs. Heat Pulse Probe – Sun position and shading effects on soil heat flux measurement in a grape vineyard? In Department of Plants, Soils and Climate Graduate student seminar.
- Naruke, C.**, Jones, S. B., Los, S., Hipps, L., McKee, L., Alfieri, J. G., ... & Kustas, W. (2017, October). Comparison of Grape Vineyard Linear-Soil Heat Flux and Soil Heat Pulse Probe Arrays. In SSSA International Soils Meeting (2019). SSSA.
- Naruke, C.**, & Jones, S. B. (2017, March). Estimation of surface soil heat flux using analytical solutions and numerical simulations. In Department of Plants, Soils and Climate Graduate student seminar.
- Naruke, C.**, & Jones, S. B. (2017, March). Exploring Soil Heat Flux Time Lag using Numerical Simulation. In Spring Runoff Conference.
- Naruke, C.**, Sakai, M., & Toride, N. (2015, October). Water Uptake and Stress of Soybean Root based on Soil Moisture Contents. In Japanese Society of Soil Physics Annual Meeting. JSSP.
- Naruke, C.**, Sakai, M., & Toride, N. (2015, August). Root growth and Water uptake distribution change of Soybean pot. In Annual meeting of the Japanese Society of Irrigation, Drainage, and Rural engineering.
- Naruke, C.**, Sakai, M., & Toride, N. (2014, October). Measurement of Transpiration and Soil Moisture Profile in Different Root Growing Stages. Japanese Society of Soil Physics Annual Meeting. JSSP.
- Sakai, M., **Naruke, C.**, & Toride, N. (2014, November). Root Water Uptake Distribution Based on Change of Soil Water Contents. In SSSA International Soils Meeting (2014). SSSA.

PROFESSIONAL ASSOCIATIONS

Soil Science Society of America
Japanese Society of Soil Physics

PROFESSIONAL SOCIETY SERVICE

Moderator in the session “Advances in Sensor Development and Application for Determination of Porous Media Properties and Processes Oral” at ASA, CSSA, SSSA annual meeting in Salt Lake City, UT, November 9, 2021